京都大学学術情報リポジトリ
KURENAI 紅
Kyoto University Research Information Repository

CHEMICAL REVIEWS

Review

Metal−Organic Network-Forming Glasses

Nattapol Ma and Satoshi Horike*

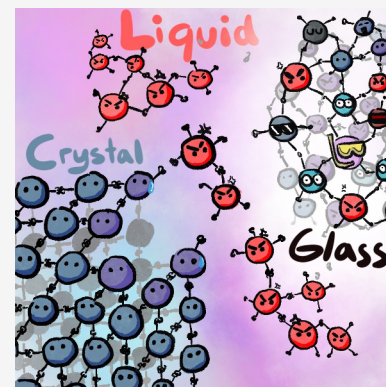Cite This: *Chem. Rev.* 2022, 122, 4163−4203

Read Online

ACCESS | Metrics & More | Article Recommendations

ABSTRACT: The crystal−liquid−glass phase transition of coordination polymers (CPs) and metal−organic frameworks (MOFs) offers attractive opportunities as a new class of amorphous materials. Unlike conventional glasses, coordination chemistry allows the utilization of rational design concepts to fine-tune the desired properties. Although the glassy state has been rare in CPs/MOFs, it exhibits diverse advantages complementary to their crystalline counterparts, including improved mass transport, optical properties, mechanical properties, and the ability to form grain-boundary-free monoliths. This Review discusses the current achievements in improving the understanding of anomalous phase transitions in CPs/MOFs. We elaborate on the criteria for classifying CP/MOF glasses and comprehensively discuss the three common strategies employed to obtain a glassy state. We include all CP/MOF glass research progress since its inception, discuss the current challenges, and express our perspective on future research directions.
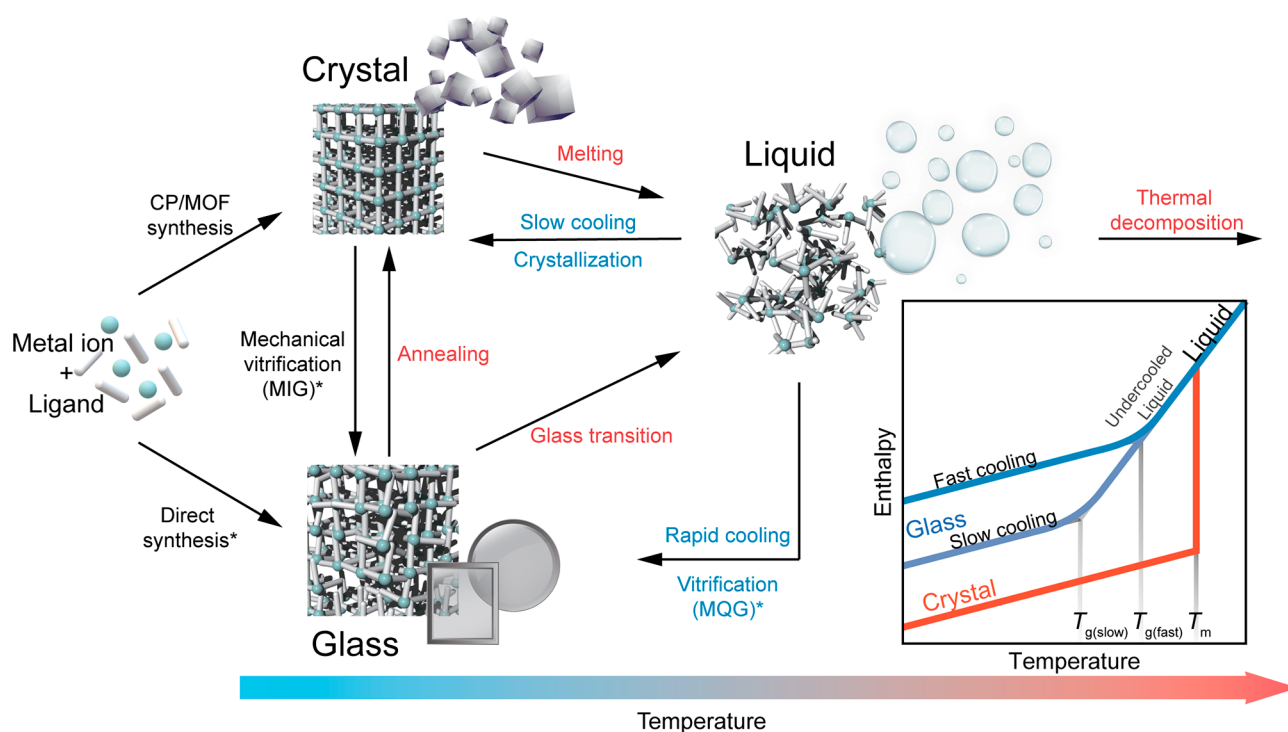
CONTENTS

Figure 1. Approaches for achieving CP or MOF glasses. Three common routes, including melt-quenching (MQG), mechanical vitrification (MIG), and direct synthesis, for achieving CP/MOF glasses are highlighted with an asterisk. The inset shows enthalpy as a function of temperature for a liquid at various cooling rates at constant pressure. Cooling a liquid at a higher rate provides a continuous glass transition. Enthalpy and T_g are dependent on the cooling rate. A discontinuous first-order crystallization process occurs at lower cooling rates. T_g and T_m represent glass transition and melting temperature, respectively. Adapted with permission from ref 21. Copyright 2018 Springer Nature. The inset adapted with permission from ref 24. Copyright 2001 Springer Nature.

1. INTRODUCTION

Coordination polymers (CPs) and metal−organic frameworks (MOFs) are solids in which the inorganic nodes, either metal ions or clusters (secondary building unit, SBU), are linked with an organic linker through coordination bonds in an infinite array.[1−5] The field of CPs/MOFs was further established when the permanent porosities and robust framework structures of $[Co_2(4,4'\text{-bipyridyl})_3(NO_3)_4]$[6] and $[Zn(1,4\text{-benzenedicarbox-ylate})]$[7] were discovered, respectively. The discovery of permanent porosity by gas adsorption experiments in design-able materials opened tremendous opportunities for designer functional materials. Since then, more than 90 000 crystalline CPs/MOFs have been reported with diverse structural motifs and applications.[2,8−20] Thus, far, the chemistry of CPs/MOFs has mostly revolved around the development of the crystalline state.[21,22] The resulting X-ray-amorphous products, either from synthesis or external stimuli, are often overlooked because they are challenging to characterize and have unrealized function-ality.

Order−disorder and solid−liquid−glass phase transitions are commonly observed in materials science. Since ancient times, these behaviors have facilitated material processing and provided access to their unique features.[23−25] Recently, an emerging class of well-characterized CPs/MOFs combines aspects of the liquid and solid states (Figure 1).[26,27] Coordination chemistry and reticular design principles offer unlimited possibilities for extending the structural diversity and properties of CPs/MOFs, which cannot be achieved in conventional inorganic, organic, and metallic glasses.[21] Despite the scarification of the porous structure of the crystal upon phase transition, opportunities have been identified for the

unique behavior of highly dense and processable glass phases. Their moldability and grain-boundary-free nature facilitate the fabrication of homogeneous membranes for gas separation,[28,29] flawless solid−electrolytes,[30−32] materials with unique optical behaviors,[33−35] and composite hybrids.[36−38] However, very few CPs/MOFs have exhibited a stable liquid state or glass transition upon amorphization. Moreover, the presence of metal−ligand coordination in the liquid state (melts) allows us to categorize the class as network-forming liquids. They are distinguished from conventional molecular fluids by their highly oriented intermolecular attraction, which corresponds to the coordination bonds between molecules.[39] The behavior is similar to the directional network of hydrogen bonds in water or the Si−O bonds and Zn−Cl between structural units of SiO_2 and $ZnCl_2$.[40] The chemical diversity of CPs and MOFs thus offers opportunities in which features can be modulated through the customization of network topologies and the variation of longer-range ordering in liquid states.[41]

At the time of writing this Review, a few reviews describing CP/MOF liquids and glasses have been published. Early reviews connected structural disorders and defects in molecular framework materials to a plausible glassy state in 2013[42] and 2016,[43] and a brief review introduced melt-quenched CP/MOF glasses in 2017.[44] A clearer distinction between the amorphous solid, glass, and liquid states in CPs/MOFs was later drawn in 2018.[21] Insights into MOF glass composites were reported in 2019,[45] and a brief history, design guidelines, and applications of CP/MOF liquids and glasses were outlined in 2020.[5] A perspective[46] and a review[47] of amorphous MOFs were published in 2021. A review on the applications of CP/

MOF glasses in mechanics, ionics, and optics was recently published in 2021.[48]

This Review provides a comprehensive discussion of the recent advancements in the fundamental aspects of CP/MOF glasses and their applications. Therefore, we have limited the scope to CPs/MOFs that exhibit a clear or at least a high possibility of glass transition behavior. We have structured this Review into eight main sections. First, we introduce CP/MOF glasses chronologically (section 1.1), define CP/MOF glasses and the related terminology (section 1.2), and categorize them (section 1.3). The second section introduces the basics of glass characterization (section 2), beginning with structural identification, thermal behavior, and chemical environment and ending with macroscopic morphology. In the next three sections, we discuss the design strategies and research progress of CP/MOF glasses obtained by melt-quenching (section 3), mechanically induced vitrification (section 4), and direct synthesis (section 5). We, then, discuss hybrid glasses and glass composites in section 6, deviating from single-component glasses. Applications employing ionic conductivity, optical properties, mechanical properties, and porosity are highlighted in section 7. We conclude the Review by providing insights into the challenges and opportunities associated with the development and application of CP/MOF glasses in section 8.

1.1. Background of CP/MOF Glasses

The observation of a stable liquid state upon heating has always been challenging because most CPs/MOFs undergo thermal decomposition upon heating, where the decomposition temperature (T_d) < melting temperature (T_m). This results in porous carbon decorated with metal or metal-oxide nanoparticles, which typically serve as a functional material.[49,50] These characteristics prohibit the preparation of glasses from CP/MOF crystals through the quenching of melts, as otherwise observed in oxide, metallic, and chalcogenide glass systems. Consequently, CP/MOF glasses were not observed until 2015, when they were prepared in three distinct studies.[26,27,33]

The demonstration of a reversible crystal−liquid−glass phase transition upon thermal treatment in one-dimensional (1D) CP $[Zn(HPO_4)(H_2PO_4)](H_2Im)_2$ was reported in 2012.[51] H_2Im denotes imidazolium. The differential scanning calorimetry (DSC) profile exhibited an endothermic peak at a T_m of 154 °C, while the quenched sample exhibited no diffraction peaks, resembling a glassy nature, which reverted to a crystalline state via physical stimuli. Later in early 2015, there were extensive studies on the thermal behavior, including T_m and the glass transition temperature, T_g, structure (magic-angle spinning nuclear magnetic resonance, MAS NMR; X-ray absorption spectroscopy, XAS; pair distribution function, PDF), mechanical properties (dynamic mechanical analysis, DMA), and ionic conductivity (electrochemical impedance spectroscopy) of $[Zn(HPO_4)(H_2PO_4)](H_2Im)_2$,[26,51] along with the introduction of three more CPs exhibiting melting and glass formation upon quenching, including metal−organic two-dimensional (2D) layered $Zn(H_2PO_4)_2(HTr)_2$[26,52] and the 1D CPs $[Zn_3(H_2PO_4)_6(H_2O)_3](HbIm)$[26,53] and $[Zn_3(H_2PO_4)_6(H_2O)_3]$-(HmbIm).[26] HTr, HbIm, and HmbIm denote 1,2,4-triazole, 1,3-benzimidazole, and 2-methylbenzimidazole, respectively. The glass structure of $Zn(H_2PO_4)_2(HTr)_2$ was later visualized by density functional theory and reverse Monte Carlo (RMC) simulations coupled with X-ray analysis (XAS and PDF).[54]

A crystal−liquid−glass transition was demonstrated for $Eu(hfa)_3(p\text{-}dpeb)$ with two coordination complex siblings, $[Eu(hfa)_3(o\text{-}dpeb)]_2$ and $[Eu(hfa)_3(m\text{-}dpeb)]_3$. The compounds are composed of Eu^{3+}, hexafluoroacetylacetonato anions (hfa^-), and a unique bent-angled phosphine oxide (p-dpeb). Variation in the regiochemistry of the dpeb ligands results in the manipulation of T_g and the luminescence properties.[33]

Despite prior reports on the mechanical and thermal amorphization of zeolitic imidazolate frameworks (ZIFs),[55−58] a clear classification of the glassy behavior of ZIFs was not proposed until 2015.[27] The phase transition of three-dimensional (3D) $Zn(imidazolate)_2$ (ZIF-4)[59] to a dense ZIF-zni phase,[60] followed by a T_m of 593 °C, was demonstrated, and a low-density glass phase was later formed via a quenching process, exhibiting a T_g of 316 °C. An extensive investigation of the structure of the liquid state of ZIF-4 was later reported in 2017.[61]

1.2. Terminology and Definitions

The distinction between the terminology of CP and MOF, or amorphous and glass, sometimes leads to confusion. This section intends to draw a more definitive border between each term based on IUPAC recommendations.[62,63] A CP is a "coordination compound with repeating coordination entities extending in one, two, or three dimensions". A coordination network is defined as "a coordination compound extending through repeating coordination entities in one dimension but with cross-links between two or more individual chains, loops, or spiro-links, or a coordination compound extending through repeating coordination entities in two or three dimensions." As a subset of CPs and coordination networks, a MOF is defined as "a coordination network with organic ligands containing potential voids". Accordingly, the IUPAC-recommended definitions involve both crystalline and amorphous phases.

To avoid further confusion between CP/MOF glasses and amorphous CPs/MOFs, the term "glass" is defined as an "undercooled frozen-in liquid." The term is valid thermodynamically even if glass has not been formed by cooling from a melt.[64,65] The absence of long-range atomic ordering and the occurrence of a second-order phase transition to a softer liquid-like state at T_g are required to classify an amorphous solid as a "glass" (inset Figure 1).[64−66] Accordingly, these definitions differentiate CP/MOF glasses from amorphous CPs/MOFs[67] as well as other related amorphous solids, such as solidified metal-containing ionic liquids,[68−71] metal−organic cages/gels/polymers,[72−77] and MOF-template derived carbon materials.[49,78,79]

1.3. CP/MOF Glass Fabrication Approaches

Because glass do not necessarily form via the cooling of a melt, a consistent amorphous structure has been demonstrated using various techniques. Identical local structures have been obtained via the melt-quenching process, mechanical induction, and direct amorphization.[80] Various methodologies that can achieve a glassy state in organic and organic glass are applicable to CPs/MOFs, yet only a few have been demonstrated. Here, we categorize CP/MOF glasses according to their glass formation approach (Figure 1).

1.3.1. Melt-Quenched Glass (MQG). This class of CP/MOF glasses is obtained when a stable liquid state is available $(T_m > T_d)$. Crystalline CPs/MOFs are heated above T_m to provide a melt state. Then, rapid cooling (vitrification) of the
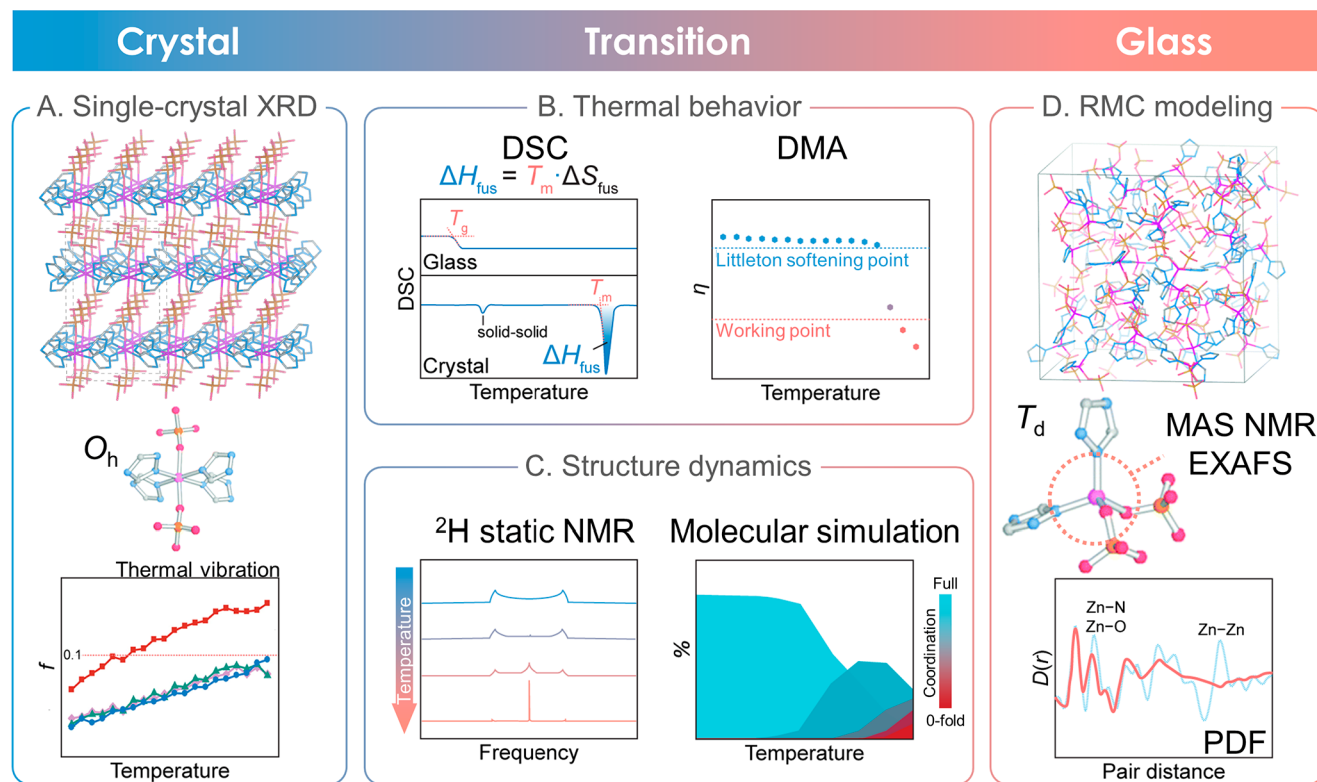
Figure 2. Selected characterizations of structures and phase transitions in CPs/MOFs. (A) Single-crystal X-ray diffraction (XRD) can determine the crystal structure, where mean atomic displacement retrieved from variable temperature measurements helps clarify the melting mechanism through Lindemann's rule. O_h represents octahedral geometry. (B) Differential scanning calorimetry (DSC) is used to determine thermal behavior, such as melting temperature (T_m) and glass transition temperature (T_g). ΔH_{fus} and ΔS_{fus} represent the difference in enthalpy and entropy of fusion between solid and liquid phases, respectively. Frequency-dependent dynamic mechanical analysis helps identify temperature-dependent viscosity (η). (C) Variable-temperature solid-state nuclear magnetic resonance (NMR) and molecular simulation are examples of characterization methods that provide insight into structural dynamics. (D) Reverse Monte Carlo (RMC) can provide atomistic modeling of the glass structure through the fitting of experimental data from pair distribution function (PDF), extended X-ray absorption fine structure (EXAFS), and magic-angle spinning (MAS) NMR. T_d represents tetrahedral geometry. Zn, C, N, O, and P atoms are represented by purple, gray, light blue, pink, and orange spheres, respectively. Representative crystal and glass structure, local geometry, and PDF data are adapted with permission from ref 54. Copyright 2015 The Royal Society of Chemistry. The DMA is adapted with permission from ref 32. Copyright 2021 The Royal Society of Chemistry. https://creativecommons.org/licenses/by/3.0/. ^{2}H static NMR is adapted with permission from ref 53. Copyright 2013 American Chemical Society. Molecular simulation is adapted with permission from ref 61. Copyright 2017 Springer Nature.

melts, faster than the crystallization rate, results in a supercooled/glassy state.

1.3.2. Mechanically Induced Glass (MIG). Melting is a rare phenomenon that is only observed in a few families of CPs/MOFs. As an alternative route for nonmelting CPs/MOFs, mechanical stimuli can induce a direct crystal-to-glass transformation via ball milling.[81]

1.3.3. Direct Synthesis of Glass. In addition to converting crystal to glass, CPs/MOFs can be synthesized directly as amorphous materials exhibiting glassy behavior.[31,34] The pathway is equivalent to the sol−gel method in conventional silica-based glasses.[82] However, extensive structural characterizations are required to obtain an exact composition/structure to validate the classification, especially the formation of coordination bond-based networks. For example, synthesis of $(dema)_{0.35}[Zn(H_2PO_4)_{2.35}(H_3PO_4)_{0.65}]$ (dema = diethylmethylammonium) results in a noncrystalline compound with glass transition behavior, where the structure was analyzed by a combination of multiple X-ray analyses, solid-state NMR, elemental analysis, and reverse Monte Carlo (RMC) simulation.[31]

2. CP/MOF GLASS CHARACTERIZATION

2.1. Structural Identification

The absence of long-range order in glassy states restricts the application of routine X-ray diffraction techniques to identify the precise position in network glasses. However, it is necessary to confirm the absence of long-range order through the observation of diffuse scattering patterns under angular diffraction (absence of Bragg peaks).[83] Diffraction patterns obtained by the scattering of X-rays, electrons, or neutrons are crucial for identifying the presence of atomic organization within the short or intermediate range. To emphasize, analysis of the scattering patterns provides a PDF, which offers direct access to the atomic structure information (Figure 2D), including the interatomic distance and coordination environment. The preservation of metal−ligand−metal connectivity in CP/MOF glasses or even the preservation of intermediate coordination networks in melts is often observed.[26,41,54,61] Moreover, access to comprehensive in situ scattering measurements allows the determination of structural evolution upon the application of external stimuli, such as temperature or pressure.[61,84] The mean thermal atomic displacement retrieved from variable-temperature single-crystal X-ray diffraction
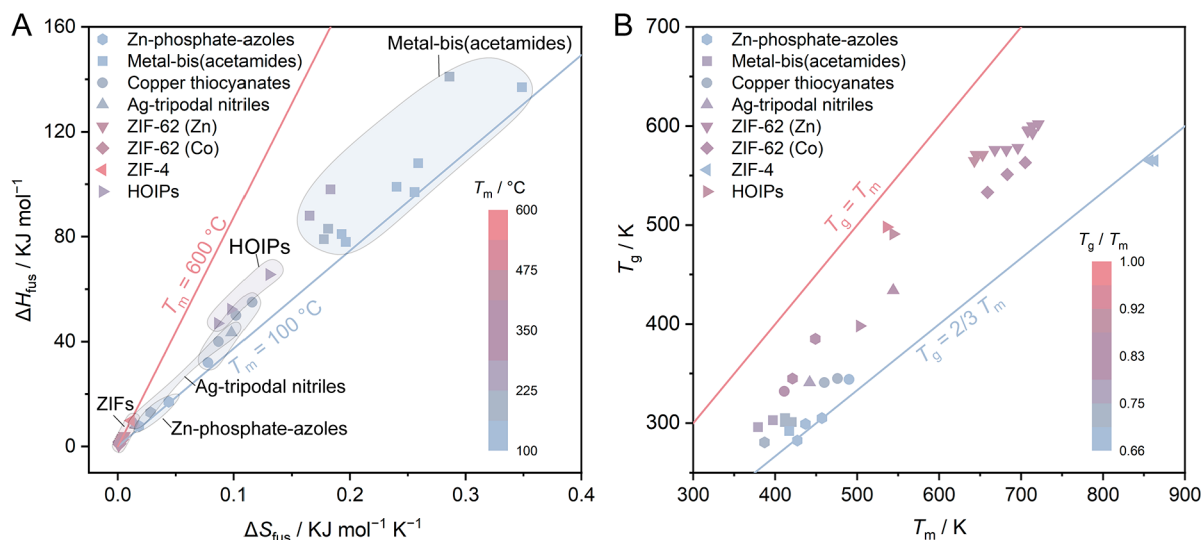
京都大学
KYOTO UNIVERSITY

KURENAI 紅
Kyoto University Research Information Repository

Chemical Reviews

pubs.acs.org/CR

Review

Figure 3. (A) Comparison of the difference in enthalpy of fusion (ΔH_{fus}), the difference in entropy of fusion (ΔS_{fus}) between solid and liquid phases, and the melting temperature (T_m) for select CP/MOF glasses. Each symbol shape denotes a series of compounds, while the symbol color represents T_m. (B) Comparison of T_g and T_m of MQGs. Empirical predictions of $T_g = 2/3\ T_m$ and the boundary of $T_g = T_m$ are plotted as lines, while the symbol color represents T_g/T_m. Data are taken from the following references: Zn−phosphate−azole,[26,32,51,54] metal−bis(acetamides),[41] copper thiocyanates,[115] Ag−tripodal nitriles,[92,93] ZIF-62,[94,114,116] ZIF-4,[27] and HOIPs.[97]

measurements, which is often overlooked, is beneficial for clarifying the melting mechanism through Lindemann's rule (Figure 2A).[26,85]

The local coordination environments of amorphous glasses around the metal of interest are detectable through X-ray absorption fine structure (XAFS) measurements (Figure 2D).[86] XAFS measurements consist of X-ray absorption near edge structure (XANES) and extended X-ray absorption fine structure (EXAFS) measurements. XAFS allows the determination of the valence states and coordination geometry of the metal nodes. While using EXAFS, the coordination numbers and bond distances of neighboring atoms are determined through radial distribution function (RDF) analysis. Probing structural evolution upon phase transition is essential to understanding the underlying mechanism. The examination involves coupling in situ X-ray or neutron analyses with variable temperature, diamond anvil cells, or mechanical milling cells.[38,84]

Visualization of amorphous glass structures has been made possible through RMC modeling (Figure 2D).[31,54,55,61] Techniques associated with fitting the experimental data, including the PDF and RDF, can be considered as Rietveld refinement analogues for the crystalline counterpart. The method involves reconfiguring atoms by successive steps until the properties simulated by the model resemble the experimental data. However, the RMC technique depends largely on the initial model and constraints applied that must be optimized to avoid unrealistic outcomes. Atomistic modeling of the melting and quenching processes has also been studied through first-principles methods, such as ab initio molecular dynamics (MD) simulations, to provide mechanistic insight into various phenomena, including melting, phase transitions, and nanoductility (Figure 2C).[61,87,88] Though they are computationally expensive, a classical description cannot describe the breaking and reconstruction of bonds since intra- and intermolecular interactions are described with parametrized force fields. Additionally, a combination of positron lifetime annihilation spectroscopy (PALS) and computational

modeling enables visualization of the internal surfaces of glasses.[89]

2.2. Thermal Behavior

Thermal analysis is generally divided into two main categories.[90] The first identifies the thermodynamic change in materials upon the application of a thermal stimulus, including the phase transition, T_g, and T_d. The temperature− residual weight relationships are obtained through thermogravimetric analysis (TGA). TGA reveals two distinct features: desolvation and T_d. Differential scanning calorimetry (DSC) is a powerful tool for investigating the detailed thermodynamic and kinetic parameters of glass-forming materials, as well as identifying phase transitions and relaxation of the system (Figure 2B).[66] The DSC profile of a MQG typically features an endothermic order−disorder phase transition at T_m and a baseline shift upon cooling at T_g, owing to the transition from a supercooled liquid to a solid glass. The subsequent cycle typically provides only the glass transition characteristics at T_g. The DSC of a MIG consists of a prerequisite glass transition at T_g. In some cases, further heating provides additional thermally induced crystallization peaks at T_c.[81,91−93] Determination of thermodynamic parameters, including the changes in the enthalpy of fusion (ΔH_{fus}) and entropy of fusion (ΔS_{fus}) upon melting, allows the chemical structure to be related to the parameters that govern the melting behavior, as well as the stability of the melts (Figure 3A).[41]

The ability of a glass-forming liquid (melt) to resist crystallization upon cooling to promote glass formation is termed glass-forming ability (GFA).[94] A glass with a low GFA value requires a higher cooling rate to prevent crystallization. The T_g/T_m relationship is beneficial for determining the GFA according to the Kauzmann "2/3" law.[94,95] The GFA is commonly inversely associated with liquid fragility (m), which corresponds to the activation energy of the viscosity at T_g and can be quantified by the T_g/T_m ratio, crystal−glass density difference ($\Delta\rho/\rho_g$), and viscosity (η) at T_m.[27,94] It was challenging to measure the data around T_g because of the lack of a viscometer that could avoid the oxygen influence. The m

value is then obtained by Mauro−Yue−Ellison−Gupta−Allan (MYEGA) viscosity model fitting.[96]

The second general type of thermal analysis correlates the mechanical response of a material to a change in temperature. Frequency-dependent DMA during the phase transition allows the estimation of mechanical softness and viscosity with respect to the temperature change (Figure 2B).[31,32] DMA can identify T_g at the maximum value of the loss modulus.[26,97] Similarly, thermal mechanical analysis (TMA) is an alternative technique to determine the glass transition and dilatomic softening temperatures.[34,97]

2.3. Chemical Environment

Vibrational spectroscopy, including infrared (IR) and Raman spectroscopy, provides information about the structure of the molecules, symmetry, host−guest interactions, and bond strength.[98] Changes or preservation in the local environment upon phase transition are distinguished through the comparison of vibrational spectra.[94,97] Terahertz (THz)/far-IR spectroscopy enables the examination of quasi-localized and collective framework dynamics beyond the range of IR and Raman spectroscopies.[99,100]

Solid-state nuclear magnetic resonance (NMR) spectroscopy is another powerful tool for probing the local environment of glass. Partial decoordination of ligands in melts or glasses is detectable through peaks that emerge in cross-polarization NMR spectra.[54,101] Proton and deuterium NMR reveal changes in the local dynamics of organic moieties upon thermal activation (Figure 2C).[32,53] 2D NMR enables direct observation of ligand−ligand or mutual host−guest interactions and spatial locations in glasses.[91,102] Observation of metal nuclei is a powerful approach. For instance, ^{67}Zn NMR can detect the short-range disorder of the coordination geometry in Zn-based MOF glasses.[103]

In addition to local geometry and bond distances, XAFS is also beneficial for elucidating the chemical environment around the atom of interest. Sufficient standard samples allow the determination of the local environment during the transition period through the combination fitting of XANES.[104] EXAFS is also sensitive to changes in the local environment, where fitting experimental data with structural modeling is potentially useful to illustrate the coordination bonding environment, as well as the Debye−Waller factor of CP/MOF glasses.[41,81]

2.4. Macroscopic Morphology

Macroscopic views of glasses are accessible through optical or electron microscopy. Under some specific constraints, the melting or recrystallization processes are identified through the observation of morphological transformations.[26,84] Cross-sectional scanning electron microscopy (SEM) enables the examination of heterogeneous interfaces, mechanical deformation, and the formation of grain-boundary-free monoliths.[32,92,93,105,106] Deformation of the glass surface or the formation of a shear band under mechanical stress is precisely quantified by atomic force microscopy (AFM).[94] In hybrid or glass composites, scanning transmission electron microscopy (STEM), energy dispersive X-ray spectroscopy (EDS), and electron energy loss spectroscopy (EELS) provide information regarding the degree of homogeneity at the interface.[36,38,107,108] Additionally, 3D EDS tomography, in which STEM-EDS data is reconstructed, improves the visualization of hybrid glass formation.[109]

2.5. Properties

Isotropic disorder domain, enhanced dynamics, and the ability to form a grain-boundary-free monolith of glasses are expected to deliver advantages in mass transport, optical properties, and mechanical properties.[48] Charge transport is probed via impedance spectroscopy with equivalent circuit fitting to identify the conductivity.[14,31,32] Generally, powders are pressed into pellets with specific dimensions. In situ melt-quenching into the measurement cell is preferred because it eliminates the contribution from interfacial resistance.[32] The contribution of the ions of interest to the total current is distinguished by the transport number (or transference number) measurement.[110] Electronic conductivity is determined by Ohm's law, where a known voltage is supplied and the current passing through is measured, or a linear relationship between current and voltage under constant rate potential sweeping. Conductivity is determined using the formula $\sigma = L/AR$, where L is the distance between contacts, A is the cross-section area, and R is the measured resistance. The thermal conductivity (κ) is calculated from $\kappa = \rho C_p \alpha$, where density (ρ), isobaric heat capacity (C_p), and thermal diffusivity (α) are determined independently.[111] Archimedes' principle, calorimetric characterization, and laser flash analysis (LFA) provides ρ, C_p, and α, respectively.

Transparency of glassy nature allows the application in optics. A spectrophotometer and a refractometer are used to measure the transmittance and refractive index of the as-prepared glass monolith.[112] Photoluminescence is characterized by a spectrofluorometer with an additional determination of luminescence lifetime and emission quantum yields.[33,34] The nonlinear optics properties of glass are examined using an open-aperture Z-scan measurement.[35]

Physical properties, including mechanical properties and porosity, are of interest. An indentation study reveals the Vickers microhardness and provides insight into the deformation behavior of glass monoliths under loads.[106] The creep resistance of glasses is evaluated by strain-rate jump (SRJ) tests and constant load and hold (CLH) indentation creep experiment.[105] A rheometer measurement provides information on the viscosity of glass.[94] Fracture toughness is measured using the single-edge precracked beam method.[113] Conventional gas/vapor adsorption techniques can evaluate the accessible pore.[92,102,114] Positron annihilation lifetime spectroscopy (PALS) has been used to identify the internal porosity, where the mapping of pore distribution is generated.[89,102] Permeation measurement requires the formation of a glass membrane, which is fixed in a module where mixed gas is fed at a constant rate with attached gas chromatography to detect permeate.[28]

3. MELT-QUENCHED GLASSES

In principle, all CPs/MOFs feature an equilibrium T_m. However, the T_d of most CPs/MOFs is located below T_m, resulting in the absence of a stable liquid state. Therefore, the melting of CPs/MOFs is achievable by either lowering T_m or raising T_d.

To control T_m, the terms that govern this first-order phase transition must first be understood. Melting is the transformation between two equilibrium phases at a well-defined temperature and pressure. It is defined by the equality of the chemical potentials of the solid and melt states, $\mu_{j,S}(T,p) = \mu_{j,L}(T,p)$. For a single-component system, the chemical
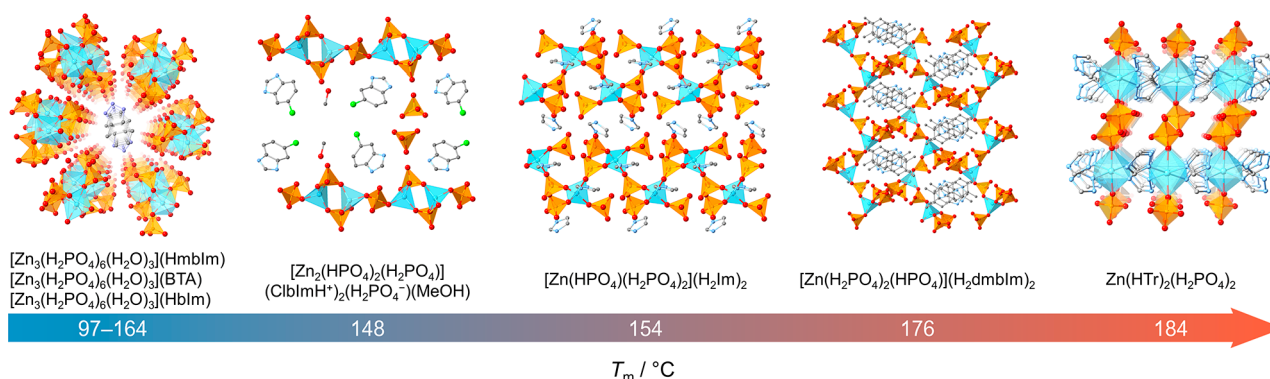
Figure 4. Crystal structures and melting temperature (T_m) values of phosphate−azole frameworks that form liquids and glasses. Zn, C, N, O, P, and Cl atoms are represented by blue, gray, light blue, red, orange, and green spheres, respectively.

potential is the same as the molar Gibbs free energy ($\mu = G$). Thus, at equilibrium, $dG = -(S_L - S_S)dT + (V_L - V_S)dp = 0$, yielding the Clapeyron equation: $dp/dT = \Delta S/\Delta V = \Delta Q/T\Delta V$. At T_m, ΔQ is the finite amount of heat required for the system to melt and is equivalent to the heat of melting/fusion (ΔH_{fus}). The transition temperature is then expressed as $T_m = \Delta H_{fus}/\Delta S_{fus}$ (Figure 3A). Therefore, T_m can be reduced through the combination of minimizing ΔH_{fus} and maximizing ΔS_{fus}.[41,65]

Minimizing ΔH_{fus} implies optimizing the cohesive interaction between the solid and melt states. In CPs/MOFs, this translates to the regulation of the strength of coordination bonds and other interactions, including hydrogen bonds, van der Waals interactions, Coulombic interactions, and steric repulsions. For a system to exhibit melting, the overall interactions must allow a certain degree of coordination bond dissociation, which further translates into inherent microscopic fluctuations and macroscopic fluidity in the liquid state. To date, CPs/MOFs with a stable liquid state are more likely to incorporate metal ions with a d^{10} configuration.[54,91] Compared with other 3d transition metals, those with a d^{10} configuration, which results in a lower crystal field stabilization energy, require comparatively less energy to dissociate the coordination bond. The choice of the ligand also plays an important role. Groups that form weak coordination bonds with metals, such as sulfonates, esters, amides, and nitriles, are more likely to provide a lower enthalpy change upon phase transition than those of ligands for highly robust frameworks, including carboxylates and azolates.[92,93,115,117] From the anticrystal engineering perspective of ionic liquid design, minimizing electrostatic attraction through charge delocalization and spatial separation of anions and cations further minimizes ΔH_{fus}.[41,115,118,119]

In solid CPs/MOFs, the entropy is composed of configurational, vibrational, and rotational entropies. Above T_m, the melt state incorporates an additional contribution from translational entropy. The utilization of low-symmetry, high-flexibility ligands should aid in maximizing ΔS_{fus} because they have access to more diverse conformations in the liquid state compared to those in their solid structure.[116,117,120] Designing CPs/MOFs with such flexible ligands and labile coordination nodes, where the extended structure limits the residual motion, should contribute to the formation of a stable liquid state because ligands possess higher degrees of freedom in the melt state.[41]

Recrystallization of glass and reversible melting of glass-forming melts remain rare in existing MQGs.[26,41] Depending on the GFA, cooling a liquid phase from above T_m result in a wide range of behaviors, including easily accessible glass transition, slow recrystallization, and rapid recrystallization.[41] Factors inhibiting recrystallization are large crystal−glass density differences ($\Delta\rho/\rho_g$), viscosity at T_m, and steric hindrance through linker complexities.[41,94] The significant change in density introduces incompatible surroundings for the nucleation process. Also, exceptionally high viscosity above T_m leads to slower relaxation dynamics and thus reduces the variety of configurations available in the melt for spontaneous nucleation. Moreover, T_m is another factor that governs the recrystallization of melts with a relatively lower GFA.[41] Faster recrystallization kinetics of melts with higher T_m is expected since higher internal thermal energy increases the probability of overcoming the energy barrier of nucleation.

Although melt-quenching is the most common method for achieving a glassy state in inorganic glasses, few CPs/MOFs exhibit a stable liquid state upon heating.[121] In this section, we distinguish MQGs into four subgroups based on the types of organic linkers.

3.1. Phosphate−Azole Frameworks

The reversible crystal−liquid−glass state transition was observed in the 1D CP $[Zn(HPO_4)(H_2PO_4)](H_2Im)_2$.[26,51] The coordination network consists of tetrahedrally coordinated Zn^{2+} and two types of orthophosphates, HPO_4^{2-} and $H_2PO_4^{-}$, which form an extended 1D chain network (Figure 4). Two crystallographically independent imidazoliums are located between the 1D chains to satisfy electroneutrality. Upon heating, DSC displays two endothermic peaks at 70 and 154 °C. The former peak (6.6 J mol^{-1} K^{-1}) results from a solid-to-solid plastic state transformation, while the latter is attributed to crystal melting (Figure 5). The liquid state is stable up to ∼200 °C, where decomposition begins. It is expected that the coexistence of the phosphates and azoles in the structure is a key factor that enables the stable melt state. These moieties form ion pairs by donating/accepting protons, where the high ionicity stabilizes the melt state and suppresses the partial vaporization of the components through Coulombic interactions. In contrast to inorganic metal phosphates (typically, $T_m > 900$ °C),[122] the inclusion of organic moieties and acidic hydrogen atoms on the phosphate linker in the melt causes a significant decrease in T_m. Upon cooling of the melt state, $[Zn(HPO_4)(H_2PO_4)](H_2Im)_2$ forms a glass with a T_g of 7.6 °C (DSC, 10 °C min^{-1}).

Figure 5. Photographs of $[Zn(HPO_4)(H_2PO_4)](H_2Im)_2$ in various states. Reprinted with permission from ref 26. Copyright 2015 American Chemical Society.

Lindemann's rule describes the melting of crystalline solids: $f = u/d$, where u is the mean thermal atomic displacement (the square root of the Debye−Waller factor) of an atom, and d is the bond distance to the nearest-neighbor atom.[85] The f value universally approaches 0.10−0.13 near T_m. In the melt state of $[Zn(HPO_4)(H_2PO_4)](H_2Im)_2$, partial dissociation of the coordination bonds and loosening of the close packing of the 1D zinc−phosphate chains are expected.[26] Among the four coordination oxygen atoms, thermal vibration analysis indicates a higher degree of thermal vibration from O9 of H_2PO_4 (P3) than those of the other oxygen atoms (Figure 6). The anomaly lies in the nearby imidazolium with a high Debye−Waller factor, which is rotatable at high temperatures. Rotatable imidazolium is hydrogen bonded with the P3 phosphate, inducing a higher thermal factor in O9. Just below T_m (at 140 °C), f(O9) is 0.12, while f(O1), f(O3), and f(O5) are less than 0.1, suggesting that Zn−O9 bond dissociation initiates melting by disrupting the stable tetrahedral arrangement. This highlights the importance of the incorporated imidazolium cations.

The preservation of coordination bonds in the melted and glassy states, in which the coordination bonds are persistent without rapid breaking and reforming events, was studied.[26] A single sharp peak in the ^{31}P NMR spectrum at 160 °C indicates that the coordination chain dissociates into ionic liquid-like discrete molecular fragments of zinc, phosphate, and imidazolium ions. The DMA of the melts supports the cleaved-bond model, which includes the absence of the entangled chain effect and a typical ionic liquid viscosity profile. In contrast, the phosphates in the quenched glass exhibit a broad chemical environment. Imidazole molecules remain protonated and do not coordinate with Zn^{2+}. XAS further indicates that the first coordination sphere of the crystal and glass are quantitatively identical. Metal−ligand−metal connectivity in the glassy state was further confirmed by PDF analysis, which demonstrated the retention of Zn−Zn correlation with a pair distance of 5.7 Å. Above 10 Å, the peaks broaden because of the absence of long-range order and are nearly featureless at $r > 20$ Å (Figure 7).

Slight alterations in chemical composition, host−guest interaction strength, or pK_a result in different thermal
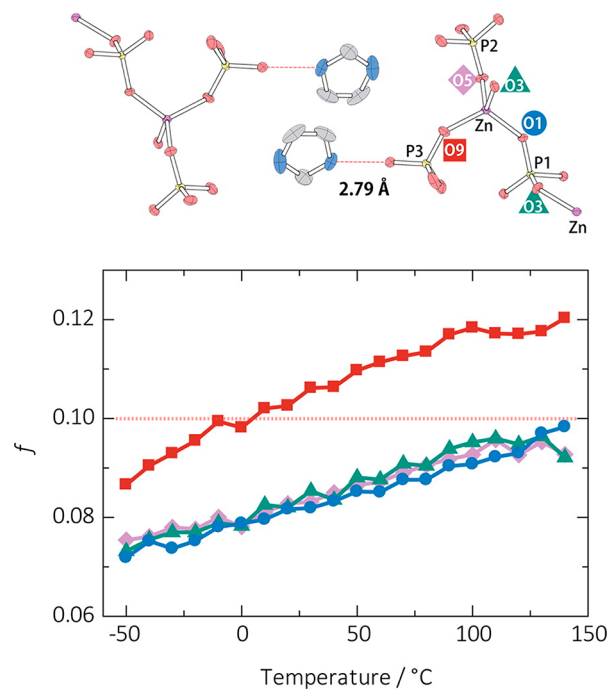

Figure 6. Degrees of thermal vibration of oxygen atoms around the Zn^{2+}. O1 (blue circles), O3 (green triangles), O5 (purple diamonds), and O9 (red squares). The ORTEP model of $[Zn(HPO_4)(H_2PO_4)]$-$(H_2Im)_2$ at −50 °C and the H-bond distances are shown on the top. The Zn, P, O, N, and C atoms are shown in purple, yellow, red, blue, and gray, respectively; H atoms have been omitted. Adapted with permission from ref 26. Copyright 2015 American Chemical Society.
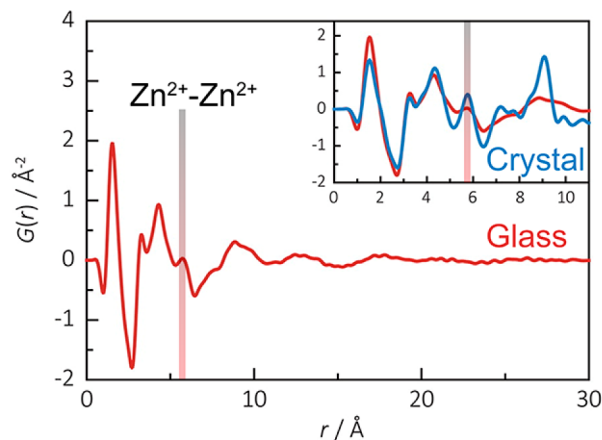

Figure 7. PDF analysis of the crystalline and glassy states of $[Zn(HPO_4)(H_2PO_4)_2](H_2Im)_2$. $G(r)$ is a reduced pair distribution function. Adapted with permission from ref 26. Copyright 2015 American Chemical Society.

behaviors. Note, pK_a expresses the acidity as $-\log K_a$, where K_a is the acid dissociation constant. There is a series of 1D H$^+$-conductive CPs composed of Zn^{2+}, phosphates, and non-coordinating azoles that includes $[Zn_3(H_2PO_4)_6(H_2O)_3]$-(HbIm) ($T_m$ = 164 °C), $[Zn_3(H_2PO_4)_6(H_2O)_3]H(2$-MebIm) ($T_m$ = 97 °C), and $[Zn_3(H_2PO_4)_6(H_2O)_3](BTA)$ (T_m = 114 °C),[26,32,53] where BTA represent 1,2,3-benzo-triazole. The compounds are composed of three crystallo-graphically independent octahedral Zn^{2+}, each with six bridging $H_2PO_4^-$ and one coordinated water molecule. HbIm, mebIm, or BTA is stacked in a 1D fashion along the a-axis and

surrounded by six chains of ZnO$_6$ octahedra, which are orderly arranged in the *bc* plane owing to hydrogen bonding (Figure 4). Despite their similarity, their T_m and T_d are sensitive to the specific azole moiety. The melting of these compounds is triggered by the rotatable azole upon thermal activation. The variable temperature ^2H solid-state static NMR spectra of $[Zn_3(H_2PO_4)_6(H_2O)_3](HbIm)$ (Figure 8) and the ^1H MAS
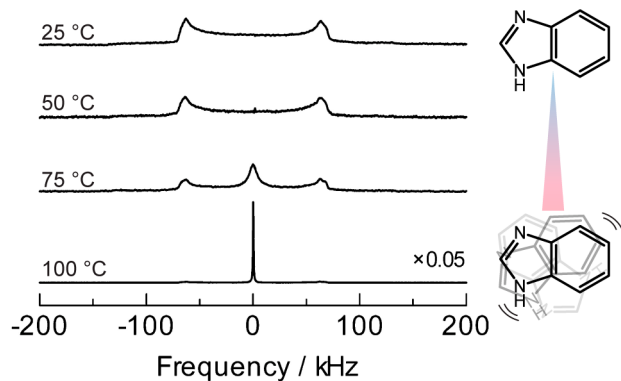
Figure 8. ^2H solid-state static NMR spectra of dehydrated $[Zn_3(H_2PO_4)_6(H_2O)_3](HbIm)$-HbIm-d$_4$ at 25, 50, 75, and 100 °C (T_m = 164 °C). Adapted with permission from ref 53. Copyright 2013 American Chemical Society.

NMR spectra of $[Zn_3(H_2PO_4)_6(H_2O)_3](BTA)$ both suggest that HbIm and BTA begin to rotate above 60 °C and thus induce melting. The melting of phosphate−azoles is not necessarily common. A stronger coordination bond and the lack of a fine balance between composition, ionicity, and bond strength prevent the congruent melting of $[Co_3(H_2PO_4)_6(H_2O)_3](HbIm)$ and $[Zn_3(H_2PO_4)_6(H_2O)_3]$-(2-chlorobenzimidazole), respectively.

The 1D chain $[Zn(H_2PO_4)_2(HPO_4)](H_2dmbIm)_2$ (H$_2$dmbIm: protonated 5,6-dimethylbenzimidazole), which has template-directed H$^+$ conduction pathways in the coordination framework, was later found to be a promising and versatile MQG platform for gas-sieving membranes.[29,123] The CP consists of a 1D chain of Zn^{2+} tetrahedrally coordinated by monodentate H$_2$PO$_4^-$ and HPO$_4^{2-}$ and bidentate HPO$_4^{2-}$. The overall charge is compensated by the inclusion of 1D $\pi-\pi$ stacking of protonated H$_2$dmbIm$^+$. The melting and glass-forming behavior of $[Zn(H_2PO_4)_2(HPO_4)]$-(H$_2$dmbIm)$_2$ were later found in three additional analogs with Cd^{2+}, Cu^{2+}, and Mn^{2+}. The analogs with Zn^{2+}, Cd^{2+}, Cu^{2+}, and Mn^{2+} exhibit T_m (T_g) values of 176 (112), 172 (105), 166 (140), and 152 (138) °C, respectively.

The 2D-to-0D structural transformation before and after glass formation was studied by intensive X-ray analysis.[54] Zn(HTr)$_2$(H$_2$PO$_4$)$_2$ is a glass-forming H$^+$-conductive CP comprising octahedral (O_h) Zn^{2+} with monocoordinated orthophosphate and bridging HTr, which form extended 2D sheets parallel to the *ab* plane (Figure 4).[52] The sheets stack in the *c* direction, and the axially coordinated phosphates form hydrogen bonds with one another in the layer. The CP melts at 184 °C. Air cooling to ambient temperatures from the molten state is sufficient to form the vitreous state with a glass transition at 32 °C, as determined by DSC.[54] The K-edge XAS spectra of the Zn^{2+} in the crystal and glass counterparts indicate that the arrangements around the Zn^{2+} are distinct, even at the nearest neighbor. The difference in the white-line

intensities suggests a change in the local symmetries around Zn^{2+}. The lower white-line intensities in the glassy state indicate that the glass transition induces a geometric change from an octahedral (O_h) to a tetrahedral (T_d) arrangement because the electronic transition associated with X-ray absorption at the K-edge of T_d Zn^{2+} has a stronger 1s to 3d transition than that of O_h.[124] RDF fitting of the MQG fits well with the model in which the Zn^{2+} is surrounded by four atoms with a shorter bond distance than those found in the crystal. The detailed structure was further analyzed using the PDF. The $D(r)$ of the MQG exhibits diminished atomic correlations above 5 Å, indicating the absence of an extended structure (Figure 9A). In addition, shorter bond distances are observed
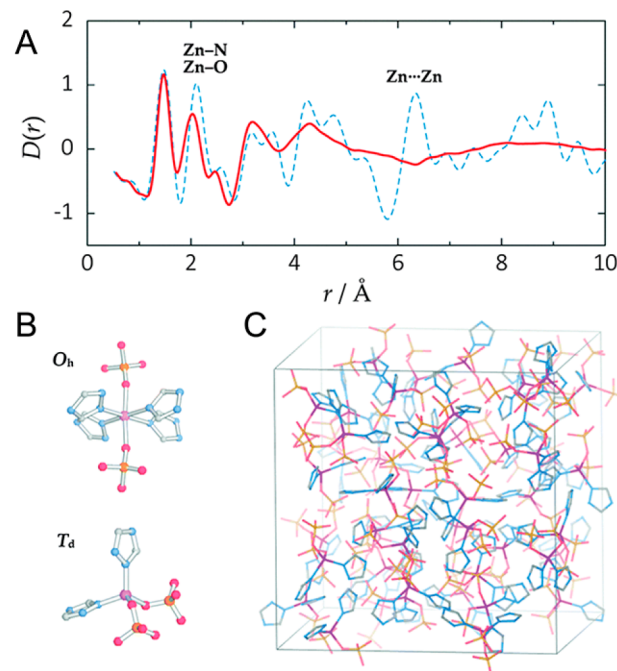

Figure 9. (A) Comparison of the $D(r)$ of crystalline Zn-(HTr)$_2$(H$_2$PO$_4$)$_2$ (blue) and MQG (red) in the range 1−10 Å (25 °C). Some of the assigned peaks of the $D(r)$ are indicated. (B) Arrangements around the Zn^{2+} for Zn(HTr)$_2$(H$_2$PO$_4$)$_2$ (top) and its MQG (bottom, postulated). (C) The RMC amorphous cell comprises 50 T_d models for the MQG. O_h and T_d represent octahedral and tetrahedral geometry. Reprinted with permission from ref 54. Copyright 2015 The Royal Society of Chemistry.

for the coordination shell of Zn^{2+}, consistent with the T_d arrangement proposed by the XAS results. This remarkably short correlation length found in the PDF profile suggests that the building unit of the MQG is likely a discrete molecule (0D, Figure 9B). A proposed structure of the MQG was simulated by replacing the bridging coordination of HTr with a monodentate ligand, which was randomly packed into 25 × 25 × 25 Å^3 cubic amorphous cells with $P1$ symmetry. The structure refined via the RMC model exhibited a refined fit of the amorphous cell in both real and reciprocal spaces (Figure 9C).

The heat capacity (C_p) is among the most important thermodynamic parameters of glasses. The C_p behavior of Zn(HTr)$_2$(H$_2$PO$_4$)$_2$ is ascribed to its discrete structure.[54] DSC of the MQG exhibits a gradually rising background, which describes the molecular rearrangements involved in the glass transition before the vibrational heat capacity is fully excited.
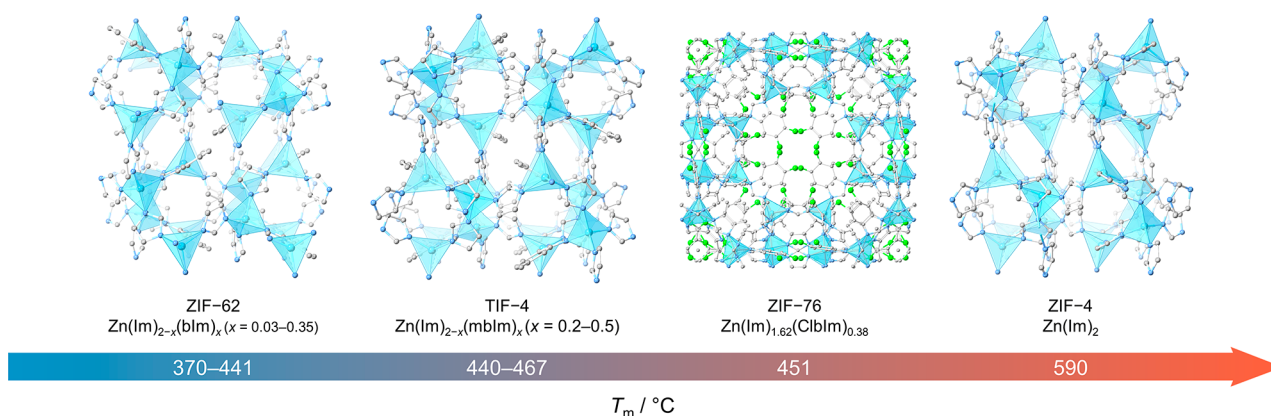
Figure 10. Crystal structures and melting temperature (T_m) of zeolitic imidazolate frameworks that form melts and glasses. Zn, C, N, and Cl atoms are represented by blue, gray, light blue, and green spheres, respectively.

In contrast to the molecular network glass, the increment of C_p at T_g ($\Delta C_p(T_g)$) of melt-quenched $Zn(HTr)_2(H_2PO_4)_2$ is more than four times larger (0.70 J K^{-1} g^{-1}) than that of high-density amorphous ZIF-4 (0.16 J K^{-1} g^{-1}).[27] This supports the importance of the discrete molecular structure in the MQG, where the configurational heat capacity is larger than that of a network glass. The change in entropy across the glass transition (7−52 °C) was ΔS = 81 J K^{-1} mol^{-1}.

The combination of ZnO, 5-chloro-1*H*-benzimidazole (ClbIm), and H_3PO_4 yields 2D frameworks of Zn^{2+} tetrahedrally coordinated with HPO_4^{2-} and $H_2PO_4^-$ as well as three types of uncoordinated guest molecules: ClbIm, methanol, and $H_2PO_4^-$.[125] Upon heating, a weight loss of 3.6%, corresponding to the release of methanol molecules, is followed by melting at 148 °C. XRD and DSC of the MQG exhibit a broad diffuse scattering pattern and a baseline shift from the glass transition with a T_g of 72 °C. The preservation of the coordination environment in the MQG is demonstrated by the RDFs. Apart from the lower peak intensity due to local disorder, the coordination environments are preserved because all peaks demonstrate an identical shape to that of the crystalline state.

3.2. Zeolitic Imidazolate Frameworks

Zeolitic imidazolate frameworks (ZIFs) or metal azolate frameworks (MAFs) primarily comprise metal ions with *N* donor azolate bridging ligands and adopt similar network topologies as those of inorganic zeolites (Figure 10).[59,126] Analogous to the thermally induced glass formation of inorganic zeolites,[127,128] heating the Zn^{2+} tetrahedrally coordinated imidazolate (Im) 3D framework $Zn(Im)_2$ (ZIF-4) initiates a transition toward a low-density amorphous (LDA) phase, followed by a subsequent phase transition from a low-density liquid (LDL) phase to a more fragile high-density liquid (HDL) phase (Figure 11A).[27] Further heating provides a dense ZIF-zni phase, followed by melting into a liquid phase. Both the quenched bulk glass and the HDA (quenched HDL) phase, after a complete liquid−liquid transition from LDL to HDA (ZIF-4 GIS), provide a virtually indistinguishable glassy state with a T_g of 292 °C despite the different thermal behaviors. Large differences in the viscosity of the supercooled LDL and HDL phases are quantified via Angell plots (log η versus T_g/T), demonstrating the fragilities of *m* = 14 and 41, respectively. Given that the melt fragility of melted silica is 20, the LDL phase (*m* = 14) is referred to as a superstrong liquid (Figure 11B).[129,130] PDF analysis of the
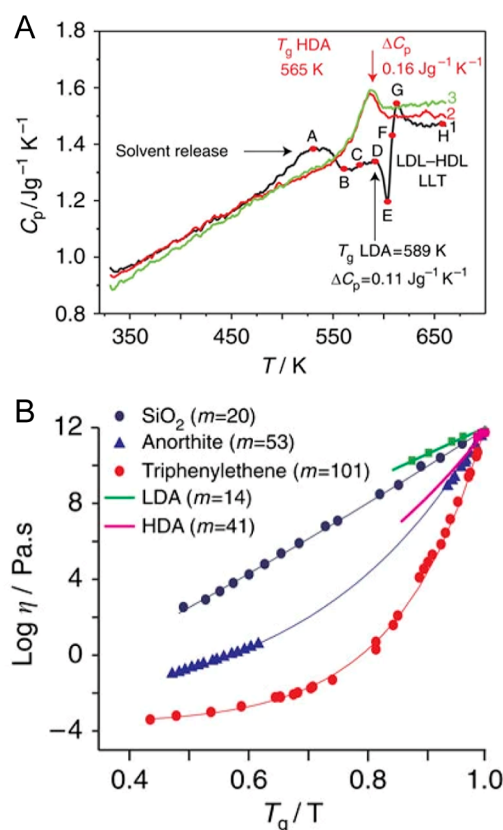
Figure 11. (A) Sequence of DSC up-scans on ZIF-4 at 10 K min^{-1} starting with ZIF-4 (black) showing solvent release (A) and collapse to the low-density liquid (LDL) phase (D−F), followed by the liquid−liquid phase transition (LLT) to the high-density liquid (HDL) phase (F−H). The jump in the isobaric heat capacity (C_p) through the LLT (E−G) is 0.33 J g^{-1} K^{-1}. ΔC_p is the difference in C_p from the glass to melt at T_g (0.11 and 0.16 J g^{-1} K^{-1} for the low-density amorphous (LDA) and high-density amorphous (HDA) phases, respectively). The endotherms in successive scans (2−red, 3−green) are for the HDA phase. (B) Angell plot showing the fragility of the LDL and HDL phases of ZIF-4 alongside other glass-forming liquids. Reprinted with permission from ref 27. Copyright 2015 Springer Nature Limited under Creative Commons license CC BY 4.0. https://creativecommons.org/licenses/by/4.0/.

ZIF-4, HDA, and MQG phases showed identical peaks below 6 Å, confirming the preservation of the tetrahedral coordination

environment in all states. Although the MQG displays a light brown color even when oxygen is excluded from the reaction, ^{1}H NMR of the digested samples confirms that the imidazolate ligands remain largely intact. In contrast, ZIF-8 ($Zn(MeIm)_2$, MeIm: 2-methylimidazole) undergoes thermal decomposition without observable melting behavior. Thermal treatment of the melt-quenched ZIF-4 glass at 520 °C ($1.38T_g$) for 420 min initiated a pronounced enthalpy release toward a lower energy state, which is attributed to pore collapse and structural densification.[131]

In addition to ZIF-4, the ZIF glass library was further extended to $Zn(Im)_2$ (GIS), TIF-4, and ZIF-62.[101] $Zn(Im)_2$ (GIS) adopts an identical chemical composition to that of ZIF-4 but is arranged in a gismondine network topology with a higher porosity of 56.9% as compared to 23.6% of ZIF-4.[132] TIF-4 and ZIF-62 are mixed-ligand variants of ZIF-4 that share a similar space group. The combination of Im and 5-methylbenzimidazolate (mbIm, $C_8H_7N_2^-$) yields TIF-4 [$Zn(Im)_{1.5}(mbIm)_{0.5}$], while the combination of Im with benzimidazolate (bIm, $C_7H_5N_2^-$) yields ZIF-62 [$Zn(Im)_{1.75}(bIm)_{0.25}$]. In DSC measurements, all four compounds exhibit melting upon heating followed by vitrification upon cooling with T_m (T_g) values of 590 (292), 584 (292), 467 (343), and 437 (318) °C for ZIF-4, $Zn(Im)_2$ (GIS), TIF-4, and ZIF-62, respectively. The T_g of the quenched glasses increases upon the inclusion of larger ligands, identical with organic polymers, where bulky side groups restrict the motion and flexibility of the backbone.

As discussed in the previous section, ZIF-4 forms an HDA phase because of thermal amorphization below T_m. Among the three additional compounds, identical behavior is only observed for $Zn(Im)_2$ (GIS).[101] TIF-4 and ZIF-62 only display thermal amorphization without the presence of T_g. The fragilities of the melts are influenced by the network architecture of the original solid phase. Although ZIF-4 and $Zn(Im)_2$ (GIS) possess an identical formula and T_m, their liquids exhibit distinct fragilities of 39 and 17, respectively. EXAFS measurements of the crystals and MQGs exhibit no differences, indicating the preservation of tetrahedral geometry around the Zn^{2+}. The PDFs of the glasses are essentially featureless above 8 Å. All the peaks below 6 Å are nearly identical, with a slight peak reduction, indicating the retention of short-range order up to the nearest Zn–Zn neighbor. ^{13}C MAS NMR reveals partial decoordination of Im ligands in ZIF-4 and $Zn(Im)_2$ (GIS).

Two more ZIF glasses involving sterically congested benzimidazolate linkers were developed with the aim of exploring permanent porosity in MOF glasses.[102] ZIF-76, $Zn(Im)_{1.62}(ClbIm)_{0.38}$ (ClbIm: 5-chlorobenzimidazolate), and ZIF-76-mbIm, $Zn(Im)_{1.33}(mbIm)_{0.67}$ (mbIm: 5-methylbenzimidazolate), exhibit endothermic melting transitions at 451 and 471 °C, followed by T_g of 310 and 317 °C, respectively, in the subsequent cycle. The higher T_m observed for the mbIm linker is due to the electron-donating methyl group, which leads to a higher energy barrier for the bond dissociation process. The larger van der Waals radius of the methyl group provides stronger noncovalent interactions between the framework constituents, resulting in a higher T_g value. In contrast to the aforementioned ZIF glasses, in which only short-range order remains in the glassy states, the PDFs of MQGs from ZIF-76 and ZIF-76-mbIm exhibit the preservation of medium-range order (i.e., Zn–Im–Zn–ClbIm connectivity,

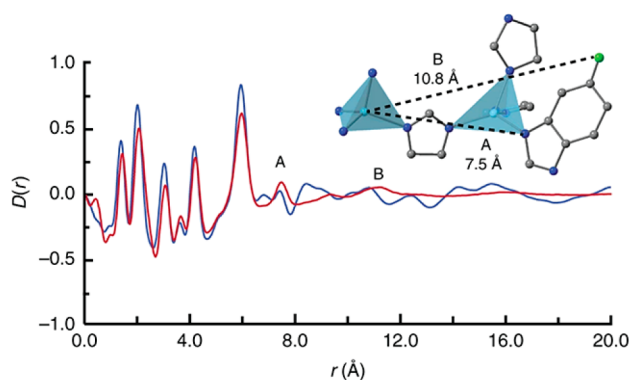Figure 12). This is ascribed to the sluggish diffusion kinetics and high viscosity of the melt states.

Figure 12. ZIF-76 pair distribution function (PDF). Inset shows medium-range order. Zn, Cl, C, and N atoms are represented by light blue, green, gray, and dark blue spheres, respectively; H atoms have been omitted for clarity. Reprinted with permission from ref 102. Copyright 2018 Springer Nature Limited under Creative Commons license CC BY 4.0. https://creativecommons.org/licenses/by/4.0/.

The chemical configuration, coordination bonding, and porosity of liquid ZIF-4 melts were studied using in situ variable X-ray diffraction, ex situ neutron PDF measurements, and first-principles MD (FPMD) simulations.[61] Upon heating from 31 to 505 °C, where the long-range order remains intact, the intensity and position of the first sharp diffraction peak (FSDP) remained constant. Further heating above T_m to 583 °C led to a reduction in the peak intensity and shift in the peak position from 1.1 to 1.3 Å^{-1}, as well as peak disappearance above the Q values and a decreased Zn–Zn correlation at 6 Å in $F(Q)$. The microscopic structural evolution was further probed by FPMD with a constant-temperature MD simulation from 27 to 1977 °C. The simulated partial radial distribution function $g_{ij}(r)$ revealed liquid-like disorder above 727 °C corresponding to the generalized Lindemann ratio of the system, satisfying the Lindemann melting criteria (0.10–0.15) at a T_m between 727 and 1227 °C. The melting mechanism of ZIF-4 was studied, and the potential of mean force (PMF) comparison revealed that the breaking of the Zn–N bond is a suitable path for reaction coordination. The distribution of Zn^{2+} coordination numbers is depicted as a function of temperature (Figure 13A) to visualize the melting process. At low temperatures (<927 °C), the undercoordination of Zn^{2+} with less than 4-fold coordination is regarded as a defect in the solid. The undercoordination of Zn^{2+} increases significantly at higher temperatures (>927 °C). At 1227 °C, where melting occurs, bond breaking and reorientation of the imidazolate linker toward nearby sites occur within a few picoseconds (Figure 13B). These results reinforce the idea that melting is driven by bond breaking and reorientation events, thus disturbing the network.

The characteristics of liquid ZIF-4 were analyzed by FPMD and RMC modeling.[61] The translational diffusion behaviors of Zn^{2+} and imidazolate at 1227 °C are comparable, with values of 7.7 × 10^{-10} and 6.5 × 10^{-10} m^2 s^{-1}, respectively. The similarity between anion and cation diffusion is considered a common feature of ionic liquids. Using helium as a probe molecule, RMC modeling based on X-ray data at 583 °C (Figure 13C) revealed that 16.2% of the porous volume was
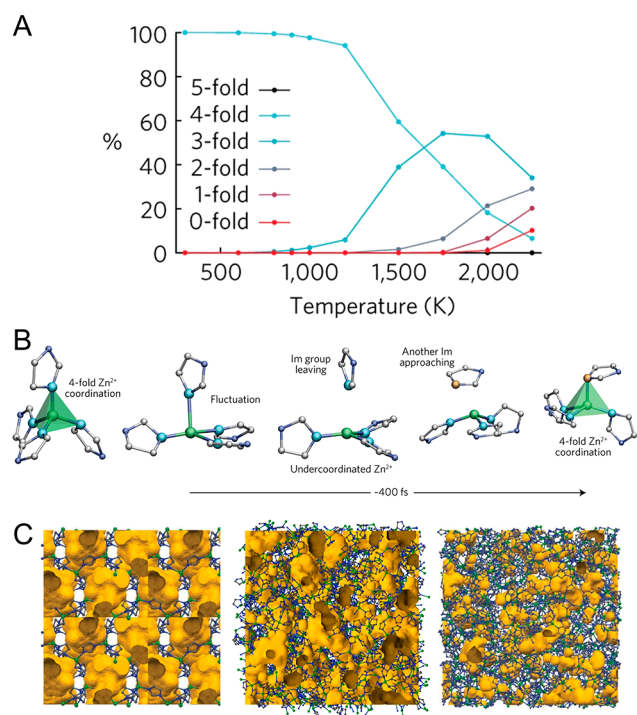
Figure 13. (A) Calculated distribution of coordination numbers around Zn^{2+} in ZIF-4 as a function of temperature. (B) Visualization of an imidazolate exchange event in ZIF-4 upon melting. (C) Atomic configurations of the ZIF-4 crystal (left), melt (middle), and glass (right) from RMC modeling of the total scattering data collected at 583 °C. Free volume is represented by orange, and Zn, N, and C atoms are represented by green, blue, and gray, respectively. Reprinted with permission from ref 61. Copyright 2017 Springer Nature.

present in the liquid state, while only 4.8% was found in the glass at ambient temperatures.

The effect of topology and chemical structure on the structure of the quenched state was further investigated by ab initio modeling with three representative ZIFs: ZIF-4, ZIF-8, and SALEM-2 $(Zn(Im)_2$, Im: imidazolate).[133,134] While ZIF-4 has the **cag** topology, ZIF-8 and SALEM-2 share the **sod** topology. Because ZIF-8 melts above its T_d in contrast to denser ZIFs, this study reveals a higher free energy barrier for the detachment of imidazolate linkers from the metal cation caused by the isolated intermediate state in the high porosity of ZIF-8. In denser ZIFs, the leaving ligand compensates instantly for the other ligands and is stabilized by dispersive interactions. The melting increases the distance to the fourth closest neighboring zinc atom by more than 15% in both ZIF-8 and SALEM-2, while only 1.5% increases were observed in ZIF-4. Structural observations demonstrate that topology has a dominant influence on melting behavior, where SALEM-2 and ZIF-8 with the same **sod** topology behave more similarly than ZIF-4. Quenching decreases the distance back to lower values than those present in crystalline states for ZIF-4 and SALEMS-2, while the distance increases to above the values of melts for ZIF-8. Therefore, the reconstruction of the frameworks (quenching) is mainly influenced by the metal–ligand chemical interactions.

The glass-forming mechanisms of ZIF-4, ZIF-zni, and ZIF-62 were traced by ^{67}Zn solid-state NMR.[103] The NMR spectra of the crystalline state indicate the presence of two individual Zn^{2+} sites (1:1 ratio), which are differentiated by two

quadrupolar coupling constants (C_Q). One of these is a more distorted $Zn[\text{ligand}]_4$ tetrahedron. Increases in C_Q and the broader distribution of the MQGs indicate the structural disorder of the $Zn[\text{ligand}]_4$ tetrahedral environment. Despite the differences in their Im/bIm ratio, all glasses display a similar ^{67}Zn NMR parameter, indicating a similar degree of short-range disorder. The line shape alteration upon glass formation reveals the disappearance of the two distinct Zn sites characteristic of ZIF crystals, indicating that the scission and renewal of the Zn–N bond upon melting initiates structural reorientation.

A series of ZIF-62 $Zn(Im_{2-x}bIm_x)$ glasses were found to exhibit an ultrahigh GFA with a high viscosity η (10^5 Pa s) at T_m, a large crystal–glass network density deficit, no crystallization in the supercooled region on laboratory time scales, a low fragility ($m = 23$), a high Poisson's ratio ($\nu = 0.45$), and the highest T_g/T_m ratio of 0.84 (Figure 14).[94] The
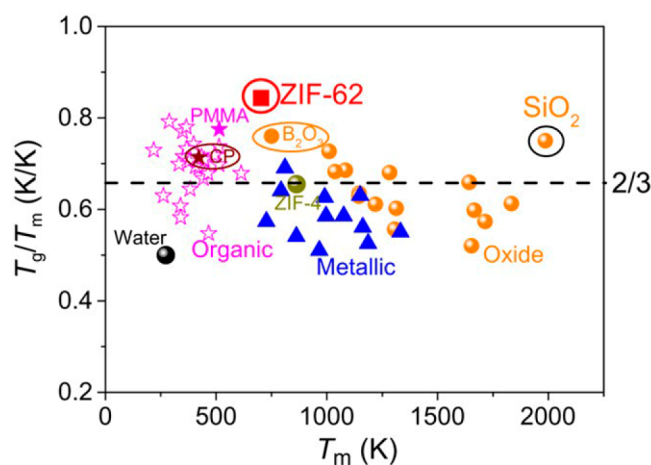
Figure 14. Comparison of the T_g/T_m ratio between ZIF-62 and other types of glass-forming systems. Reprinted with permission from ref 94. Copyright 2018 American Association for the Advancement of Science Limited under Creative Commons license CC BY 4.0. https://creativecommons.org/licenses/by/4.0/.

obtained T_g/T_m value is considerably larger than that of the Kauzmann "2/3" law.[95,135] While T_g and T_m increase with the increasing amount of bIm, the system tends to retain the T_g/T_m ratio. A thermodynamic study revealed that the marginal difference in the Gibbs free energy between the crystal and supercooled liquid of ZIF-62 is insufficient to drive nucleation at temperatures between T_g and T_m.[136]

The phase transition behavior of ZIF-62 under simultaneous high-pressure and high-temperature conditions has been studied using in situ PXRD with a resistively heated membrane-driven diamond anvil cell (DAC).[84] The study allows the construction of a P–T phase diagram from the resulting stability fields of various phases (Figure 15). Under single stimuli, ZIF-62 undergoes T-induced amorphization at ∼320 °C at ambient P and P-induced amorphization at ∼5 GPa at ambient T. The P- and T-induced amorphizations are distinct. The former reverts to the initial phase upon decompression and is thus ascribed to a displacive transition. In contrast, thermal amorphization is irreversible and is identified as a reconstructive phase transition. Simultaneous application of high P and high T reveals a change in the gradient of the crystalline to solid–amorphous transition and can be derived from the $\Delta S/\Delta T$ term of the Clausius–

Figure 15. Pressure−temperature phase diagram of ZIF-62. The stability field of crystalline ZIF-62 is shown in blue, tracing the res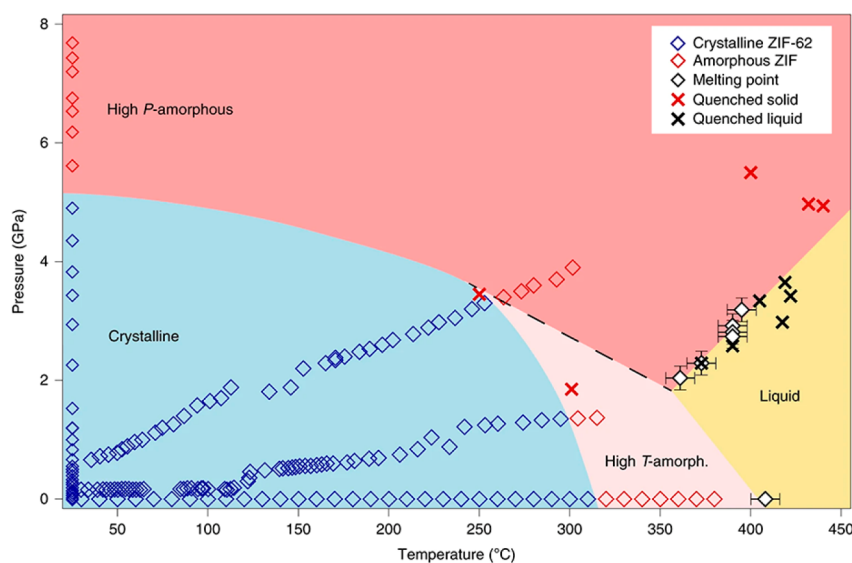ults of the PXRD phase transition analysis (blue and red diamonds). Two distinct amorphous phases with high and low densities relative to each other are shaded dark red (high P) and light red (high T), respectively. This distinction is based on changes in the slopes of both the crystalline−amorphous and solid−liquid phase boundaries. The phase boundary between the two amorphous phases is tentatively indicated with a dashed black line. The stability field for liquid ZIF-62 is shown in yellow, which is defined by melting points observed optically at high P and using DSC at ambient P. Crosses indicate the high-P/high-T conditions from which the samples were quenched for morphological analysis. Reprinted with permission from ref 84. Copyright 2019 Springer Nature.

Clapeyron relation. There are six different T_m at high P, ranging from 2 to 3.5 GPa, and the melting curve exhibits two distinct regions: a negative slope from ambient P to <2 GPa and a positive gradient at >2 GPa. A negative gradient indicates the solid phase has a lower density than that of the melts and vice versa for a positive gradient. To gain further insight, FPMD simulations reveal that the melting mechanism is not directly affected by pressure. A distinct decrease in the free energy barrier when the pressure increases from 0.1 to 5 GPa indicates the softening of the Im−Zn−Im angle upon pressurization, compensating for the thermodynamic barrier of melting. An identical study on the rich polymorphism of ZIF-4 was performed with more complex solid−solid phase transitions.[137]

The variation of the ZIF composition has been studied through topological constraint theory (TCT) to further gain control and understanding of the T_g of ZIF glasses.[138] The model incorporates a hierarchy of bond constraints and can predict T_g from a topological perspective as a function of bIm concentration $Zn(Im_{2-x}bIm_x)$ with an error of 3.5 °C. The model was further developed to account for the effect of additional mbIm ligands through TIF-4 experimental data. The incorporation of mbIm allowed the prediction of T_g for an unsynthesized, hypothetical MQG system Zn-$(Im)_{2-x-y}(bIm)_x(mbIm)_y$ (Figure 16). The TCT model later proved to provide accurate predictions, with a difference between the experimental and predicted T_g values below ∼6 °C.[139] Additional experimental data are required for systems with high mbIm and bIm concentrations because the experimental range only covers $Zn(Im)_{2-x-y}(bIm)_x(mbIm)_y$ variants with $x = 0.17-0.27$ and $y = 0.09-0.21$ where T_g appears between 305 and 316 °C.

Alteration of the ligand composition and metal substitution from conventional Zn^{2+} to Co^{2+} have been used to engineer the thermal behavior. Crystalline ZIF-62 constructed from Co^{2+} $Co(Im)_{1.7}(bIm)_{0.3}$ melts at 432 °C, which is slightly
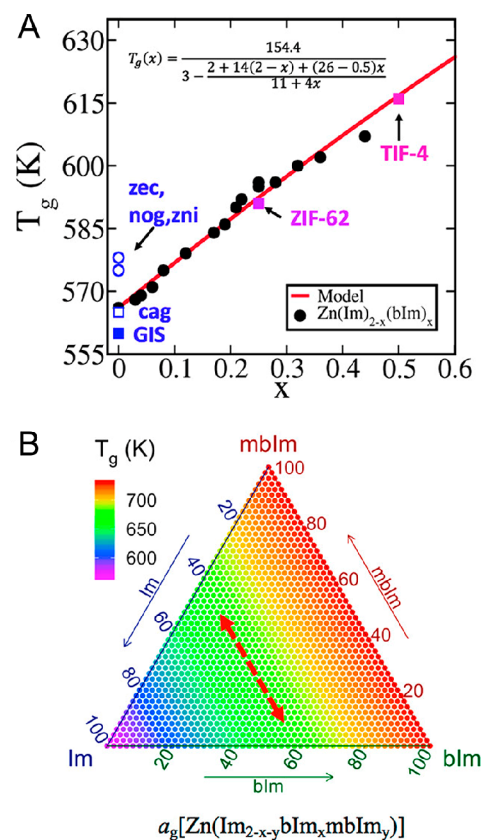

Figure 16. (A) Comparison of T_g values obtained from experiments and topological constraint theory. (B) Compositional dependence of T_g for the predicted $Zn(Im)_{2-x-y}(bIm)_x(mbIm)_y$ glass system. Reprinted with permission from ref 138. Copyright 2018 American Chemical Society.

lower than its Zn^{2+} counterpart with a smaller stability window, $T_d \approx 550$ °C.[114] The quenched glass exhibits a T_g of 290 °C, which is considerably lower than that of ZIF-62(Zn) (320 °C). In addition to monometallic ZIFs, bimetallic ZIF-62 with both Co^{2+} and Zn^{2+} in a single-phase $Zn_{1-x}Co_x(Im)_{1.7}(bIm)_{0.3}$ has been reported.[140] According to earlier results, the substitution of Co^{2+} up to 50% does not affect T_d (580 °C). T_m and T_g increased from 447 to 452 °C and from 328 to 334 °C as the Co^{2+} concentration increased. In contrast, subsequent work with ZIF-62 synthesized by mechanical milling demonstrated otherwise.[141] The addition of Co^{2+} into ZIF-62, $Zn_{1-x}Co_x(Im)_{1.75}(bIm)_{0.25}$, caused a decrease in T_m from 401 °C at 0% Co^{2+} to 389 °C at 20% Co^{2+}. In contrast, T_g remained mostly unchanged throughout the concentration range. Systematic control of both T_m and T_g of prototypical ZIF-62 has been demonstrated by adjusting the molar ratio of the two imidazolate linkers in the range $x = 0.02-0.35$, $M(Im)_{2-x}(bIm)_x$; $M^{2+} = Zn^{2+}$, Co^{2+}.[116] Cation substitution vastly impacts T_d, ~510−500 °C for Co^{2+} and ~550−600 °C for Zn^{2+}, but minimally affects T_m. Interestingly, the T_m of ZIFs is linearly dependent on the molar ratio of Im^- and bIm^-, ranging from 370 ($x = 0.03$) to 440 °C ($x = 0.35$, Figure 17).
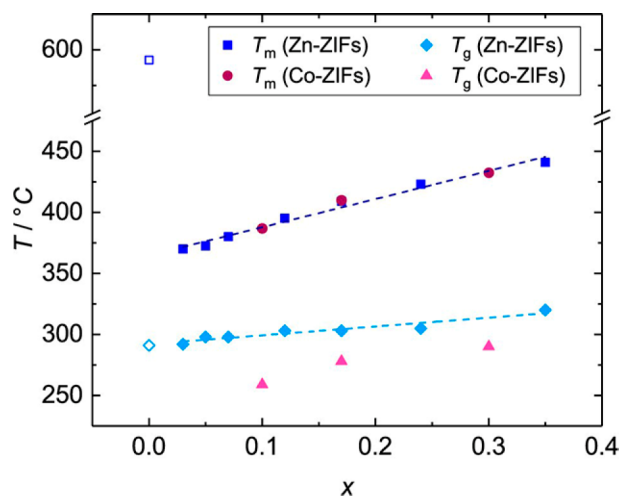

Figure 17. Evolution of T_m and T_g of ZIF-62 ($M(Im)_{2-x}(bIm)_x$; M^{2+} = Zn^{2+}, Co^{2+}). The values for ZIF-4 are shown with open symbols for comparison. Reprinted with permission from ref 116. Copyright 2019 American Chemical Society.

Moreover, the liquid state of ZIFs with $x < 0.05$ is metastable and tends to undergo partial crystallization toward the ZIF-zni phase at approximately 500 °C, while a stable liquid state is expected for ZIFs with $x \geq 0.05$. An uneven distribution of linkers might cause unexpected polymorph formation, resulting in a distinct deviation of the thermal behaviors.[142] An identical correlation was observed in $Zn(Im)_{2-x}(ClbIm)_x$, where increasing x from 0.05 to 0.25 caused T_m and T_g to increase from 367 to 423 °C and from 296 to 317 °C, respectively.[141]

The thermal behavior of ZIF-62 also depends on steric effects.[100] By incorporating halogenated benzimidazolate-derived linkers, four additional ZIF-62 analogs were synthesized with 5-chlorobenzimidazolate (5-ClbIm), 5-chloro-2-methylbenzimidazolate (5-Cl-2-mbIm), 5-fluorobenzimidazolate (5-FbIm), and 6-chloro-5-fluorobenzimidazolate (6-Cl-5-FbIm) linkers. The synthesized compounds have a variety of halogenated benzimidazolate concentrations, making it difficult to draw a clear conclusion on the effect of the side group on the thermal behavior. When $Zn(Im)_{1.75}(bIm)_{0.25}$ is compared to $Zn(Im)_{1.74}(5-Cl-2-mbIm)_{0.26}$, T_m of the latter decreases slightly from 400 to 390 °C because it contains the most sterically large ligand. It results in a denser structure, promoting the dispersive interaction between the framework and the partially dissociated ligand. A subsequent study clarified that the presence of electron-withdrawing ligands lowers both the T_m and T_g of ZIFs.[143] Replacing the mbIm ligand in TIF-4 $Zn(Im)_{1.8}(mbIm)_{0.2}$ with ClbIm, $Zn(Im)_{1.8}(ClbIm)_{0.2}$, caused a significant reduction in T_m and T_g. T_m and T_g decreased from 440 to 428 °C and from 350 C to 336 °C, respectively. The number of components in ZIF-62 also affects thermal behavior.[144] The overall trend of T_m is $Zn(Im)_{1.95}(bIm)_{0.05}$ ($T_m = 370$ °C, $T_g = 308$ °C, $T_g/T_m = 0.90$) > $Zn(Im)_{1.95}ClbIm_{0.05}$ ($T_m = 366$ °C, $T_g = 296$ °C, $T_g/T_m = 0.89$) > $Zn(Im)_{1.95}(bIm)_{0.025}(ClbIm)_{0.025}$ ($T_m = 356$ °C, $T_g = 296$ °C, $T_g/T_m = 0.90$) > $Co_{0.2}Zn_{0.8}(Im)_{1.95}(bIm)_{0.025}(ClbIm)_{0.025}$ ($T_m = 310$ °C, $T_g = 288$ °C, $T_g/T_m = 0.96$). The inclusion of the 1-methylimidazole (1-mIm) modulator in ZIF-4 and the synthesis conditions affect the particle size, size distribution, morphology, and surface defects of the resultant product.[145,146] These variations affect the polymorphic phase transition, recrystallization, melting, and glass formation of ZIF-4.
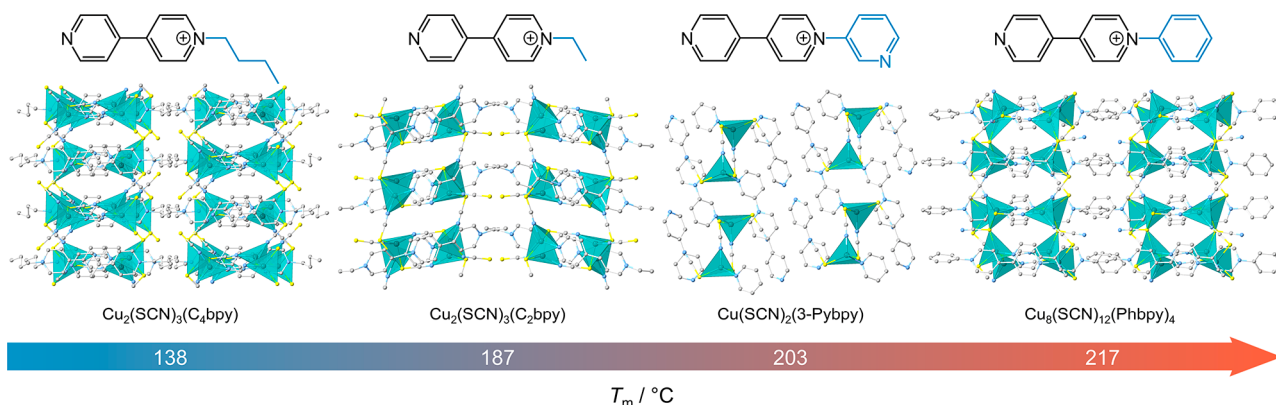

Figure 18. Crystal structures and melting temperature (T_m) values of thiocyanate-4,4′-bipyridin-1-ium derivative frameworks that form liquids and glasses. Cu, C, N, and S atoms are represented by teal, gray, light blue, and yellow spheres, respectively.

3.3. Thiocyanate and Nitrile-Based Frameworks

With the aim of extending the library of meltable CPs/MOFs to include a larger number of metals and ligands, anticrystal engineering strategies have been utilized to control the T_m of CP crystals.[115] Ions with reduced symmetry and delocalized charge were selected to achieve minimum molecular interactions with sufficient Coulombic interactions between anionic and cationic moieties. Four meltable CPs were synthesized with d^{10} Cu$^+$, ionic-liquid-forming charge-delocalized thiocyanate (SCN$^-$), and a series of low-symmetry 4,4′-bipyridin-1-ium derivatives (Figure 18). The series consists of Cu$_2$(SCN)$_3$(C$_2$bpy), Cu$_2$(SCN)$_3$(C$_4$bpy), and Cu$_8$(SCN)$_{12}$(Phbpy)$_4$ with two tetrahedral Cu$^+$ bridged by SCN$^-$ via S,N bridging to form a distorted dimeric Cu$_2$(SCN)$_2$ cluster. Two clusters are connected by the bridging tetrahedral Cu$^+$ through S,S bridging, forming 2D anionic Cu$_2$(SCN)$_3$. The negatively charged anionic structure is then balanced by the coordination of the 4,4′-bipyridin-1-ium-based cationic ligand from the opposite side of the 2D sheet. C$_2$bpy, C$_4$bpy, and Phbpy represent the 1-ethyl-[4,4′-bipyridin]-1-ium, 1-butyl-[4,4′-bipyridin]-1-ium, and 1-phenyl-[4,4′-bipyridin]-1-ium ligands. In contrast, Cu(SCN)$_2$(3-Pybpy) has a 1D helical chain structure with tetrahedral Cu$^+$ connected by SCN$^-$ through S,N bridging, and the coordination environment is completed with 3-Pybpy. The overall trend for T_m is Cu$_8$(SCN)$_{12}$(Phbpy)$_4$ (T_m = 217 °C) > Cu(SCN)$_2$(3-Pybpy) (T_m = 203 °C) > Cu$_2$(SCN)$_3$(C$_2$bpy) (T_m = 187 °C) > Cu$_2$(SCN)$_3$(C$_4$bpy) (T_m = 138 °C), indicating that the substituent group of the pyridinium ligand directly impacts crystal melting. In general, increasing the alkyl chain length, Cu$_2$(SCN)$_3$(C$_4$bpy) and Cu$_2$(SCN)$_3$(C$_2$bpy), reduces the overall symmetry of the system and decreases the lattice energy, thus providing a lower energy barrier for melting. This explanation is supported by the lower melting enthalpy (ΔH_m) and entropy (ΔS_m) observed in DSC measurements. In contrast, the pendant phenyl rings in Cu$_8$(SCN)$_{12}$(Phbpy)$_4$ stabilize the framework through $\pi-\pi$ interactions with adjacent phenyl rings. These interactions provide additional stability and, thus, the highest T_m. In principle, the 1D chain structure of Cu(SCN)$_2$(3-Pybpy) requires the least amount of energy to initiate melting. The $\pi-\pi$ interactions between the pyridinium and adjacent pyridine ring (N at the para position) with rings from neighboring chains stabilizes the structure. These interactions are considerably stronger than the van der Waals interactions in Cu$_2$(SCN)$_3$(C$_4$bpy) and Cu$_2$(SCN)$_3$(C$_2$bpy), resulting in a higher T_m. The T_g/T_m of the MQGs depends on the substitution group. A higher degree of rotational freedom and the plasticizing effect provide a better GFA with T_g/T_m values of 0.74 for Cu$_2$(SCN)$_3$(C$_2$bpy) and 0.77 for Cu$_2$(SCN)$_3$(C$_4$bpy). In contrast, the dangling phenyl and pyridine rings favor the formation of an ordered structure owing to the $\pi-\pi$ interactions, resulting in lower T_g/T_m values of 0.69 and 0.73 for Cu$_8$(SCN)$_{12}$(Phbpy)$_4$ and Cu(SCN)$_2$(3-Pybpy), respectively. The preservation of the coordination environment with partial uncoordination and lower symmetry in some Cu$^+$ units was verified via Cu K-edge XAS, which enables recrystallization through mechanical hand grinding.

1D cobalt and cadmium pyrazinamide dithiocyanate CP analogs, [Co(μ-NCS)$_2$(C$_5$H$_5$N$_3$O)$_2$]·C$_5$H$_5$N$_3$O and Cd(μ-NCS)$_2$(C$_5$H$_5$N$_3$O)$_2$, use asymmetrical organic ligands to achieve crystal melting and MQGs.[144,147] Co^{2+} is octahedrally coordinated with two monodentate pyrazinamide in a trans geometry and with four bridging thiocyanate ligands, two

through N and two through S. DSC and TGA revealed a T_m of ~198 °C with a small weight loss of ~7% (from 190 °C), indicating a narrow temperature range for a stable liquid. Quenching provided a MQG with a T_g of ~79 °C. The Cd^{2+} analog exhibited a slightly higher T_d of ~220 °C and T_m of 205 °C. In contrast to Co^{2+}, crystallization occurred upon cooling, with an exothermic peak at 146 °C.

2D and 3D Ag-based frameworks with tripodal nitrile ligands have exhibited melting and the ability to form MQGs (Figure 19).[92,93] The labile and dynamic nature of the coordination
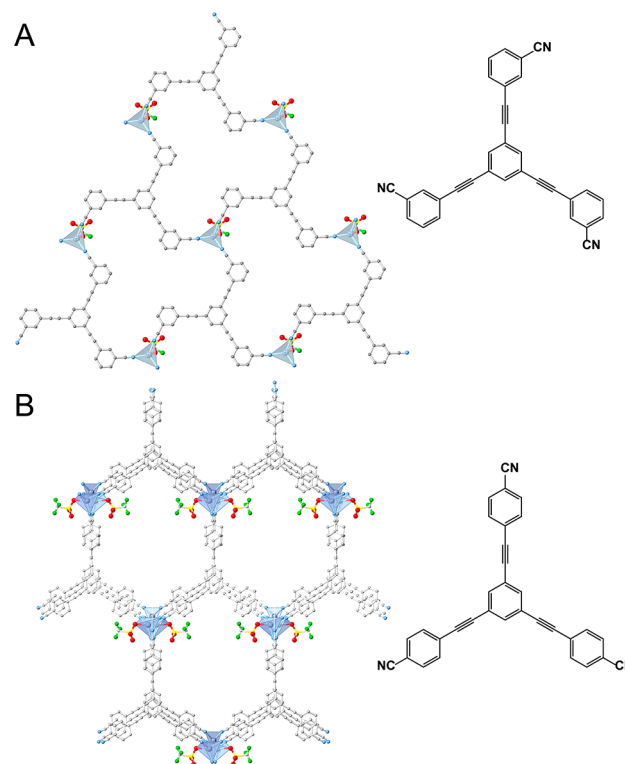
Figure 19. Crystal structures and ligands of (A) [Ag(mL1)-(CF$_3$SO$_3$)]·2C$_6$H$_6$ and (B) [Ag(pL2)(CF$_3$SO$_3$)]·2C$_6$H$_6$. Ag, C, N, O, F, and S atoms are represented by blue, gray, light blue, red, green, and yellow spheres, respectively.

bond between the nitrile group and metal ions is expected to aid crystal melting. 2D [Ag(mL1)(CF$_3$SO$_3$)]·2C$_6$H$_6$ consists of Ag$^+$, 1,3,5-tris(3-cyanophenylethynyl)benzene (mL1), CF$_3$SO$_3^-$, and guest benzene.[92] The four Ag$^+$ coordination sites are occupied by three nitrile-bound mL1 and one CF$_3$SO$_3^-$. The extended 2D layered structure is stacked in an ABCD fashion with a channel filled with benzene guest molecules. The DSC of the degassed phase revealed an endothermic T_m at 169 °C with a wide temperature range, over 110 °C, of liquid stability. The quenched glass exhibited a T_g at 68 °C without any crystallization peaks over the experimental range of 200 °C. Another meltable Ag-based framework with a tripodal nitrile ligand is 3D [Ag(pL2)(CF$_3$SO$_3$)]·2C$_6$H$_6$.[93] It consists of Ag$^+$, 1,3,5-tris(4-cyanophenylethynyl)benzene (pL2), and CF$_3$SO$_3^-$. One CF$_3$SO$_3^-$ is coordinated with one of the four Ag$^+$ coordination sites. The other retains a counteranion with the disorder. Three of the sites are connected to three different pL2 ligands, forming a 3D interpenetrated network honeycomb architecture. DSC and Variable-temperature PXRD measurements revealed two

distinct endothermic peaks at 237 and 271 °C corresponding to solid−solid and solid−melt transitions, respectively. The quenched glass exhibited a T_g of 161 °C without any crystallization. It is worth mentioning that both CPs also undergo mechanical vitrification, leading to the formation of MIG, which is discussed in section 4.2.

Succinonitrile (SN)-based ligands show a propensity to form quenched glasses through rapid quenching.[30] A 3D Li-conductive CP, Li[N(SO$_2$F)$_2$](NCCH$_2$CH$_2$CN)$_2$, was designed to minimize metal−ligand interactions by utilizing a hard acid, Li$^+$, and a soft base, SN according to the hard−soft acid−base theory. SN was selected instead of nitrile to avoid decomposition through volatilization. The CP has a diamond-like 3D network consisting of Li$^+$ linked with four NCCH$_2$CH$_2$CN (Figure 20A). Charge compensation is

Figure 20. (A) Crystal structure of Li[N(SO$_2$F)$_2$](NCCH$_2$CH$_2$CN)$_2$. Li, C, N, O, F, and S atoms are represented by indigo, gray, light blue, red, green, a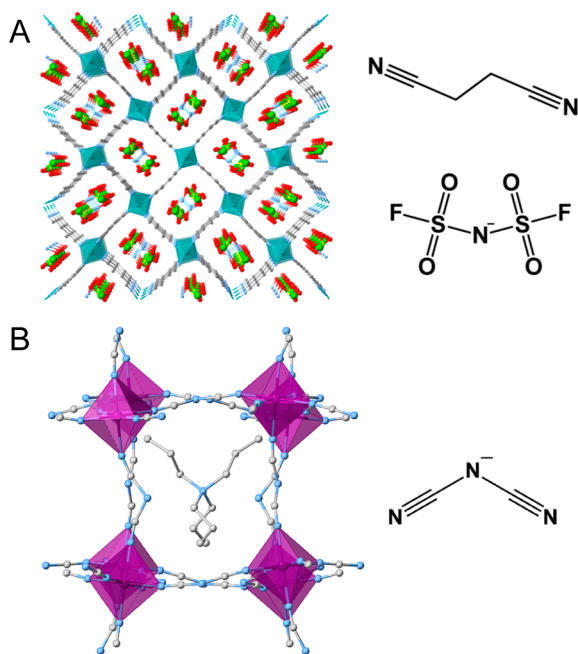nd yellow spheres, respectively. (B) Crystal structure of (TPrA)[M(dca)$_3$], M = Mn^{2+}, Fe^{2+}, Co^{2+}. M, C, and N atoms are represented by purple, gray, and light blue spheres, respectively.

achieved through the incorporation of N(SO$_2$F)$_2$$^-$ in the interstitial sites. Upon heating, the crystal melts at a low T_m of 59.5 °C. Although the compound does not form a glass upon cooling owing to the crystallization process, both X-ray diffraction and diffuse scattering results indicate a tendency to form a MQG with sufficiently rapid quenching.

Melting and glass formation of hybrid organic−inorganic perovskites (HOIPs) has been observed in dicyanamide-based (dca, N(CN)$_2$$^-$) frameworks.[97] Three representative (TPrA)-[M(dca)$_3$] (TPrA = tetrapropylammonium (CH$_3$CH$_2$CH$_2$)$_4$N$^+$, M = Mn^{2+}, Fe^{2+}, Co^{2+}) compounds with the empirical structure ABX$_3$ were selected (Figure 20B). The dca bridges the octahedrally coordinated metal nodes through the N atom in a $\mu_{1,5}$ end-to-end connectivity. The TPrA resides in the cavity to maintain the electroneutrality of the framework. Melting was observed via DSC with T_m values of 271, 263, and 230 °C for the Mn^{2+}, Fe^{2+}, and Co^{2+} analogs, respectively. The increase in T_m follows the trend in the ionic

radii $r_{Co} < r_{Fe} < r_{Mn}$, which is consistent with the hard−soft acid−base theory in which softer metal nodes interact preferably with the soft dca ligand. Cooling of these melts yields a quenched glass with diffuse X-ray scattering and T_g at 218, 225, and 125 °C for Mn, Fe, and Co, respectively. The glass transition behavior was also supported by TMA and DMA with TMA temperatures of 209, 220, and 102 °C and T_g of 185, 219, and 145 °C from the peak loss moduli for Mn, Fe, and Co glasses, respectively. The chemical structures of the (TPrA)[M(dca)$_3$] glasses were investigated via spectroscopy and X-ray analyses. ^{13}C MAS NMR revealed that TPrA remains intact after the melt-quenching process. Changes in the NMR, IR, and UV−vis spectra indicated a degree of decoordination and decomposition of the dca ligand during crystal melting. Temperature-dependent DC magnetic suscepti-bility measurements indicated a reduction in the oxidation state of the metal nodes, with reduced percentages of 18.7%, 22.0%, and 15.3% for the Mn, Fe, and Co glasses, respectively. The PDFs exhibited peak broadening and the absence of long-range order with a degree of M−dca−M connectivity retention. To further clarify the microscopic evolution of the framework upon melting, FPMD simulations of crystalline (TPrA)[Mn(dca)$_3$] were performed at 27, 477, 927, and 1427 °C. The generalized Lindemann ratio, calculated from the Mn−N correlation, exceeded the melting criteria between 477 and 927 °C. Thermal fluctuations of N−Mn−N away from a perfect octahedral structure were observed to intensify upon thermal activation. Moreover, the potentials of mean force calculation indicated that the melting mechanism of these (TPrA)[M(dca)$_3$] is similar to the proposed mechanism of ZIF-4, with a smaller contribution from the activation entropy.

3.4. Metal−Bis(acetamide) Frameworks

A systematic study of metal−bis(acetamide)-based coordina-tion compounds allows a generalization of the thermodynamic strategies for controlling the melting behavior of CP/MOF glasses through enthalpic and entropic driving forces.[41] The combination of weak coordination bonds, conformationally flexible bridging ligands, and weak electrostatic interactions between spatially separated cations and anions reduces the enthalpy of fusion (ΔH_{fus}) while increasing the entropy of fusion (ΔS_{fus}), resulting in a low melting point framework because $T_m = \Delta H_{fus}/\Delta S_{fus}$. These qualities were observed in Co(hmba)$_3$[Co(NCS)$_4$] [hmba = N,N'-1,6-hexamethylenebis-(acetamide)]. The compound melts at 144 °C (ΔH_{fus} = 108 kJ mol^{-1}) and undergoes recrystallization upon isothermal heating at 120 °C for less than 1 h. The low T_m is attributed to the large ΔS_{fus} of 260 J mol^{-1} K^{-1}, high conformational flexibility of the ligand, and increased dynamics of uncoordi-nated anions in the melt state.

A series of 3D M(bba)$_3$[M'Cl$_4$] networks (M/M' = Mn, Fe, Co; M = Mn, M' = Zn; and M = Mg, M' = Co, Zn) were synthesized to improve the understanding of the structural and chemical factors affecting melting dynamics.[41] Octahedral divalent metal centers are each connected to six other nodes by bridging N,N'-1,4-butylenebis(acetamide) (bba) ligands, form-ing a 3D cubic network that surrounds tetrahedral uncoordi-nated anions (Figure 21A and 21B). All six compounds exhibit a reversible melting transition with T_m ranging from 124 °C for Co(bba)$_3$[CoCl$_4$] to 262 °C for Mg(bba)$_3$[ZnCl$_4$] (Figure 21C and Table 1). T_m is influenced mainly by the lack of enthalpy−entropy compensation. The driving force for the higher T_m of Mn(bba)$_3$[MnCl$_4$] compared to that of the Co^{2+}

京都大学
KYOTO UNIVERSITY

Chemical Reviews

pubs.acs.org/CR

Review

KURENAI 紅
Kyoto University Research Information Repository
京都大学学術情報リポジトリ

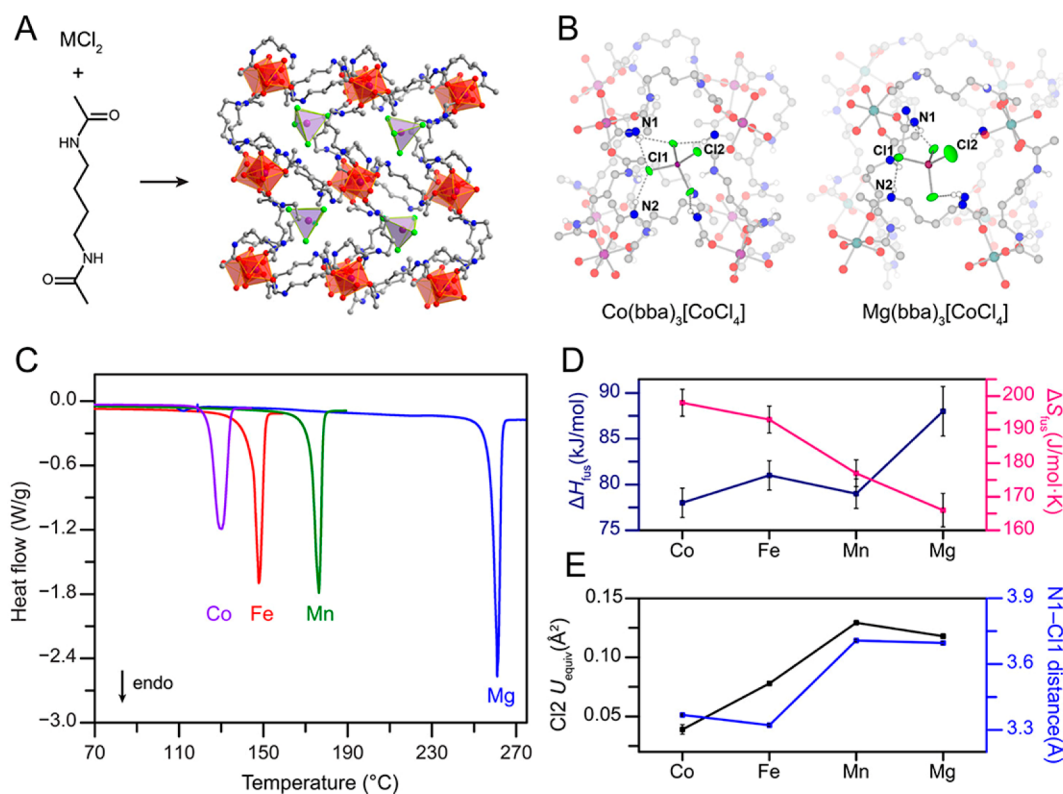**Figure 21.** (A) Crystal structure of the 3D Co(bba)$_3$[CoCl$_4$]. Note that the bba ligand is disordered over two positions, and only the higher occupancy atomic positions are shown. Purple, red, gray, blue, and green spheres represent Co, O, C, N, and Cl atoms, respectively; H atoms have been omitted for clarity. (B) Comparison between the geometry of hydrogens bonds with [CoCl$_4$]$^{2-}$ for Co(bba)$_3$[CoCl$_4$] and Mg(bba)$_3$[CoCl$_4$] at −173 °C to highlight the additional set of moderate hydrogen-bonding interactions present in the former compound. Teal spheres represent Mg atoms, and only N−H protons are shown. (C) DSC traces for M(bba)$_3$[M'Cl$_4$] compounds (M/M' = Co, Fe, Mn; and M = Mg, M' = Co) with a heating rate of 5 °C min^{-1} for all compounds. (D) Trends of difference in enthalpy (ΔH_{fus}) and entropy (ΔS_{fus}) of fusion between solid and liquid phases for Co(bba)$_3$[CoCl$_4$], Fe(bba)$_3$[FeCl$_4$], Mn(bba)$_3$[MnCl$_4$], and Mg(bba)$_3$[CoCl$_4$]. (E) Equivalent isotropic displacement parameters, U_{equiv}, of Cl2 atoms and N1−Cl1 hydrogen bond donor−acceptor distances at −173 °C, generally correlated with each other and inversely correlated with ΔS_{fus}. Reprinted with permission from ref 41. Copyright 2021 American Chemical Society.

and Fe^{2+} analogs is primarily entropy. In contrast, the higher T_m of Mg is driven by both enthalpy and entropy (Figure 21D). The enthalpic trends follow the M−O coordination bond strength, where Mn−O < Fe−O < Co−O < Mg−O. Stronger M−O bonds lead to a larger ΔH_{fus} because more energy is required to partially dissociate the bonds between M and bba, as well as the hydrogen bonds between amides and uncoordinated [MCl$_4$]$^{2-}$, when the amide carbonyl is more polarized owing to a stronger interaction. In contrast, entropic trends are more complicated. Although all the compounds present identical dimensionality and connectivity around the metal centers, the difference in the N1−C3−C4−C5 dihedral angle of bba ligands leads to a different arrangement and number of hydrogen bonds between the N−H protons of bba and the Cl of [MCl$_4$]$^{2-}$. An additional set of hydrogen bonds with Cl1 atoms in the Co and Fe analogs limits the residual motion of the counteranions and ligands, which reduces vibrational and rotational entropy, and restricts disorder or reduces configurational entropy (Figure 21B). The lower isotropic atomic displacement parameters (U_{equiv}) of Cl2 atoms support the explanation regarding the lower entropy in the solid phase for both analogs, which results in a higher ΔS_{fus} upon melting (Figure 21E).

Replacing uncoordinated [MCl$_4$]$^{2-}$ with Cl$^-$ (M(bba)$_3$X$_2$) yields a 2D hexagonal network, Mg(bba)$_3$Cl$_2$, with a coordination environment identical with that of Mg-

(bba)$_3$[CoCl$_4$] (Figure 22).[41] The 2D network has a 70% higher ΔH_{fus} than its 3D counterpart, owing to the stronger hydrogen bonds between the bba ligands and the more charge-dense Cl$^-$ acceptors. However, the compound melts 40 °C below the T_m of its 3D counterpart because the increase in ΔH_{fus} is fully compensated by an increase in ΔS_{fus}. This occurs through restricted residual motion owing to the strong hydrogen-bonding network in the solid state and the increased translation entropy of halide anions in the melts. Consequently, the presence of porosity in many CPs/MOFs could, in part, hinder the observable melting point because porosity can incorporate organic ligands with a high degree of residual motion in the solid state, which reduces the ΔS_{fus} for melting.

Metal−bis(acetamide)-based coordination compounds exhibit the network-forming nature of the melt state and the composition dependence of the GFA.[41] The local structure of Co(bba)$_3$[CoCl$_4$] just below and above T_m was probed through X-ray total scattering and EXAFS. The melt-state PDF revealed the preservation of the average local coordination environment around the Co centers, with a coordination number reduction of 20%. Apart from the short-range periodicity, the melt exhibited network-forming liquid characteristics with the FSDP at 0.98 Å^{-1}. Quasiperiodic oscillations at up to 80 Å verified the persistence of some degree of intermediate- and extended-range order in the liquid

Table 1. Selected Properties of MQGs

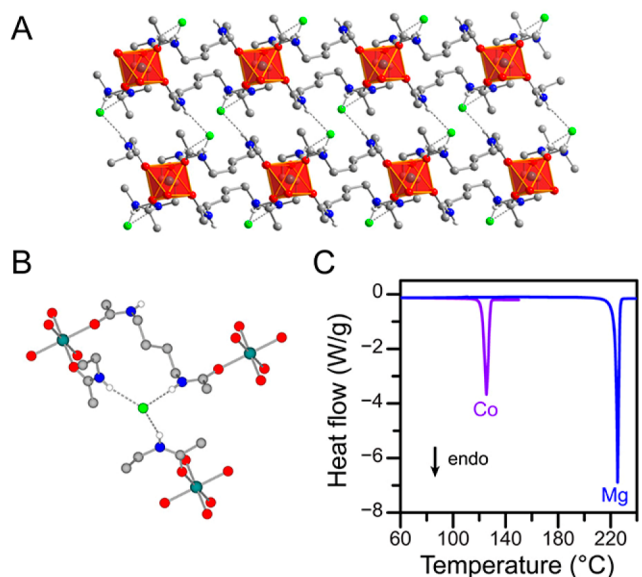| materials[a]	dimensionality	T_m (°C)	T_g (°C)	ΔH_{fus} (kJ mol^{-1})	ΔS_{fus} (J mol^{-1} K^{-1})	ref
phosphate–azole frameworks						
$[Zn(HPO_4)(H_2PO_4)_2](ImH_2)_2$	1D	154	9.4	7.8	18.2	26, 51
$[Zn_3(H_2PO_4)_6(H_2O)_3](HbIm)$	1D	164				26, 53
$[Zn_3(H_2PO_4)_6(H_2O)_3](HmbIm)$	1D	97				26
$[Zn_3(H_2PO_4)_6(H_2O)_3](BTA)$	1D	114	7.6	17	44	32
$[Zn(H_2PO_4)_2(HPO_4)](H_2dmbIm)_2$	1D	176	112			29, 123
$Zn(HTr)_2(H_2PO_4)_2$	2D	184	32	13.0	28.4	26, 52, 54
$[Zn_2(HPO_4)_2(H_2PO_4)](ClbImH^+)_2 \cdot (H_2PO_4^-) \cdot (MeOH)$	2D	148	72			125
zeolitic imidazolate frameworks						
$Zn(Im)_2$/ZIF-4	3D	590	292	9.9	11.4	27, 101
$Zn(Im)_2$ (GIS)	3D	584	292			101
$Zn(Im)_{2-x}(bIm)_x$ ($x = 0.03-0.35$)/ZIF-62 (Zn)	3D	370–448	292–329	0.4–4.1	0.7–5.6	94, 114, 116
$Co(Im)_{2-x}(bIm)_x$ ($x = 0.10-0.30$)/ZIF-62 (Co)	3D	386–432	260–290	0.8–2.7	1.2–3.8	114, 116
$Zn(Im)_{1.62}(ClbIm)_{0.38}$/ZIF-76	3D	451	310			102, 105
$Zn(Im)_{1.33}(mbIm)_{0.67}$/ZIF-76-mblm	3D	471	317			102, 105
$Zn(Im)_{1.5}(mbIm)_{0.5}$/TIF-4	3D	467	343			101
$Zn(Im)_{1.8}(mbIm)_{0.2}$/TIF-4	3D	440	350			143
$Zn(Im)_{1-x}(ClbIm)_x$ ($x = 0.05-0.28$)	3D	366–432	296–336			100, 143
$Zn(Im)_{1.87}(6\text{-}Cl\text{-}5\text{-}FbIm)_{0.13}$	3D	406	250			100
$Zn(Im)_{1.81}(5\text{-}Cl\text{-}2\text{-}mbIm)_{0.19}$	3D	390	336			100
$Zn(Im)_{1.66}(FbIm)_{0.34}$	3D	421	290			100
$Zn_{1-x}Co_x(Im)_{1.70}(bIm)_{0.30}$ ($x = 0.007-0.5$, $y = 0.25-0.3$)	3D	399–452	331–334			140, 141
$Zn(Im)_{1.95}(bIm)_{0.025}(ClbIm)_{0.025}$	3D	356	296			143
$Co_{0.2}Zn_{0.8}(Im)_{1.95}(bIm)_{0.025}(ClbIm)_{0.025}$	3D	310	288			144
$Zn(Im)_{2-x-y}(bIm)_x(mbIm)_y$ ($x = 0.17-0.27$, $y = 0.09-0.21$)	3D	418–433	305–316			139
thiocyanate and nitrile-based frameworks						
$Cu(SCN)_2(3\text{-}Pybpy)$	1D	203	72	55	115.5	115
$Cu_2(SCN)_3(C_2bpy)$	2D	187	68	40	86.9	115
$Cu_2(SCN)_3(C_4bpy)$	2D	138	59	32	77.8	115
$Cu_8(SCN)_{12}(Phbpy)_4$	2D	217	71	50	102	115
$(C_4C_1py)[Cu(SCN)_2]$	1D	87.9				148
$\alpha\text{-}[Cu(ipim)]$	1D	185				149
$\beta\text{-}[Cu(ipim)]$	1D	146				149
$[Co(\mu\text{-}NCS)_2(C_5H_5N_3O)_2]\cdot C_5H_5N_3O$	1D	180/198	79			144, 147
$Cd(\mu\text{-}NCS)_2(C_5H_5N_3O)_2$	1D	185/205				144, 147
$[Ag(mL1)(CF_3SO_3)]\cdot 2C_6H_6$	2D	169	68	43.4	98.2	92
$[Ag(pL2)(CF_3SO_3)]\cdot 2C_6H_6$	3D	271	161	8.2	15.1	93
$Li[N(SO_2F)_2](NCCH_2CH_2CN)_2$	3D	59.5				30
$(TPrA)[Mn(dca)_3]$	3D	271	218	46.9	86.2	97
$(TPrA)[Fe(dca)_3]$	3D	263	225	52.3	97.6	97
$(TPrA)[Co(dca)_3]$	3D	230	125	65.5	130.3	97
metal–bis(acetamide) frameworks						
$Co(hmba)_3[CoBr_4]$	2D	106	23	97	255	41
$Mn(hmba)_3[MnCl_4]$	2D	139	32	99	239	41
$Mn(hmba)_3[MnBr_4]$	2D	139	28	99	240	41
$Co(bba)_3Br_2$	2D	120		137	348	41
$Mg(bba)_3Cl_2$	2D	220		141	287	41
$Co(hmba)_3[Co(NCS)_4]$	3D	144	19	108	260	41
$Co(bba)_3[CoCl_4]$	3D	124	30	78	198	41
$Fe(bba)_3[FeCl_4]$	3D	147	28	81	193	41
$Mn(bba)_3[MnCl_4]$	3D	172		79	177	41
$Mn(bba)_3[ZnCl_4]$	3D	185		83	182	41
$Mg(bba)_3[CoCl_4]$	3D	260		88	166	41
$Mg(bba)_3[ZnCl_4]$	3D	262		98	183	41
phosphine-oxide/ethynyl frameworks						
$Eu(hfa)_3(p\text{-}dpeb)$	1D		46, 96			33

[a]See Abbreviations.

Figure 22. Crystal structure of $Mg(bba)_3Cl_2$ highlighting the (A) 2D coordination network and (B) hydrogen bonds with Cl^- (dashed lines). Teal, red, gray, blue, green, and white spheres represent Mg, O, C, N, Cl, and H atoms, respectively; only N–H protons are shown for clarity. (C) DSC traces for $Mg(bba)_3Cl_2$ (blue) and $Co(bba)_3Br_2$ (purple) with a heating rate of 5 °C min^{-1}. Reprinted with permission from ref 41. Copyright 2021 American Chemical Society.

state arising from the topological and chemical ordering of the network-forming liquid. Conventionally, the cooling of CP/MOF melts results in MQGs. In contrast, the melting transitions of metal−bis(acetamide)-based coordination compounds are mostly reversible, with a wide variation in liquid recrystallization kinetics upon cooling. For instance, the cooling of $Mn(bba)_3[MnCl_4]$, $Co(hmba)_3$-$[Co(NCS)_4]$, and $Co(hmba)_3[CoBr_4]$ at 10 °C min^{-1} results in rapid recrystallization, slow recrystallization, and a glass transition, respectively. The difference in cooling kinetics is composition dependent and is explained by the viscosity just above T_m. Viscosity evaluation just above T_m reveals that a higher viscosity leads to slower relaxation dynamics and thus a higher GFA.

4. MECHANICALLY INDUCED GLASSES

Not all CPs/MOFs exhibit a stable liquid state. As an alternative route, mechanically induced amorphization directly converts crystals into a glassy state through compressive, shear, and tensile stresses.[81,91,150] This method has long been applied to induce crystal-to-glass phase transitions in inorganic compounds, such as Se,[151−154] metals/metal oxides,[155] metal alloys,[156] and organic compounds.[150,157−163] This nonthermal direct phase transition is initiated by the mechanical instability of the framework upon pressurization. To understand the root of mechanically induced amorphization, the changes in the elastic tensors, which represent the stress/strain responses in specific directions, upon pressurization must be considered. For the unpressurized stable crystal, all the eigenvalues of the stiffness matrix are positive, and they diminish in certain components under mechanical stress. A further increase in mechanical load initiates a phase transition when the elastic tensor drops below the requirement for Born stability.[164−166] This plastic deformation thus induces a direct transformation from crystal to glass, also known as solid vitrification.

In contrast to MQGs, MIGs are more likely to undergo recrystallization under thermal treatment above the crystallization temperature (T_c).[81,91] Crystallization of the amorphous state below this temperature is limited to the growth of residual nuclei without nucleation. Thus, this feature is not present in undercooled MQGs or in prolonged mechanical treatment, where none of the starting nuclei survive.[150] This demonstrates the difference in the equilibrium landscape between MQGs and MIGs under the laboratory time scale. The multiple local potential energy minima (basins) in the multidimensional potential energy surface can be visualized as a function of particle coordinates (Figure 23).[24,167] Although
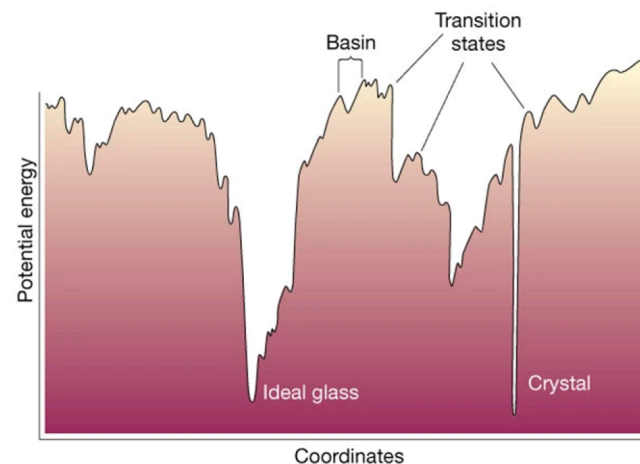
Figure 23. Schematic of an energy landscape. The *x*-axis represents all configurational coordinates. Reprinted with permission from ref 24. Copyright 2001 Springer Nature.

the average potential energy per atom of a MQG depends on the quenching rate, liquid-state intermediates ensure that all crystalline domains are distorted thoroughly. In contrast, the degree of disorder in a MIG depends on the combination of the applied mechanical load and the mechanical properties of the framework. The former includes the milling duration, collision frequency, and stress-energy in mechanical milling or the applied pressure in hydrostatic pressurization.[168−170] The latter depends mostly on the intrinsic bulk, Young's, and shear moduli of the frameworks.[165,166] Although mechanical treatment has a broad array of applications, the formation mechanism of MIGs remains largely unknown.

4.1. $M^{2+}(1,2,4\text{-triazole})_2(H_2PO_4)_2$

A direct crystal-to-glass phase transition through mechanical milling was first demonstrated in $Cd(HTr)_2(H_2PO_4)_2$.[81] In contrast to its Zn-based analog with a stable liquid state, heating does not result in melting but rather thermal decomposition ($T_m > T_d$). The Cd^{2+} are octahedrally coordinated by axial monocoordinated $H_2PO_4^-$ with bridging 1,2,4-triazole and monocoordinated phosphate, forming a 2D structure (Figure 24A). $Cd(HTr)_2(H_2PO_4)_2$ underwent solid vitrification upon milling treatment via ZrO_2 planetary milling at 400 rpm for 40, 240, and 500 min, whereas Zn-$(HTr)_2(H_2PO_4)_2$ did not. Diffuse PXRD scattering patterns confirmed a complete crystal-to-amorphous transition in the presence of T_g and exothermic T_c, as verified by DSC. When the milling duration was increased from 40 to 240 and 500 min, the enthalpy of crystallization increased from -37 ± 1 to -46 ± 1 and -48 ± 1 J g^{-1}, respectively. This implies that the

京都大学
KYOTO UNIVERSITY
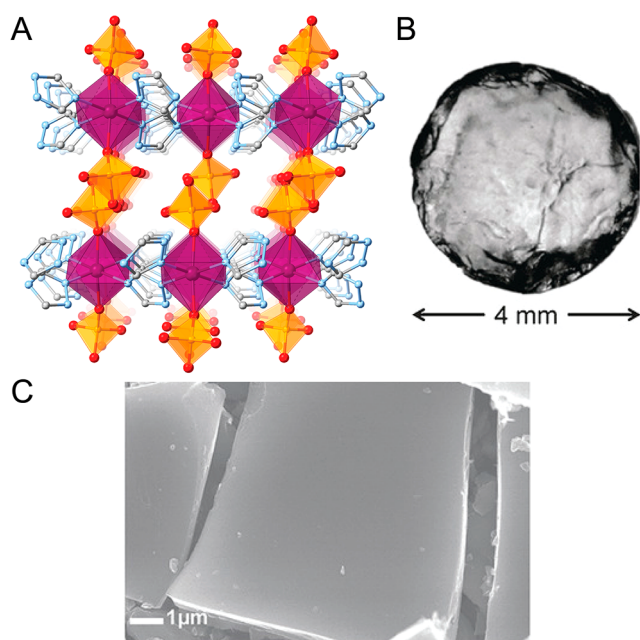
KURENAI 紅
Kyoto University Research Information Repository

Chemical Reviews

pubs.acs.org/CR

Review

Figure 24. (A) Crystal structure of $M(HTr)_2(H_2PO_4)_2$, M = Cd^{2+}, Cr^{2+}, Mn^{2+}, Fe^{2+}, Co^{2+}. M, C, N, O, and P atoms are represented by burgundy, gray, light blue, red, and orange spheres, respectively. (B) Photograph and (C) SEM image of a $Cd(HTr)_2(H_2PO_4)_2$ glass, 240 min of mechanical treatment, pellet prepared at 4 GPa. Reprinted with permission from ref 81. Copyright 2016 John Wiley and Sons.

MIG has multiple stress-dependent equilibrium states. The amorphous nature allows the formation of a transparent monolith from the glass powder. A monolith with a diameter of 4.2 mm and a thickness of 1.0 mm was prepared by hot pressing at 4 GPa and 70 °C for 2 h (Figure 24B). The SEM image of the monolith exhibits a smooth, crack- and grain-boundary-free surface (Figure 24C).

The local arrangement around Cd^{2+} in $Cd(HTr)_2(H_2PO_4)_2$ was studied by XANES.[81] The results confirmed the retention of octahedral geometry around Cd^{2+}, and the local disorder in the glassy state was verified with a slightly diminished intensity of the Cd−O, Cd−C, Cd−N, and Cd−P peaks due to ligand disorder. The PDF of the MIG exhibited a broad Cd^{2+}−Cd^{2+} correlation feature, confirming the structural distortion upon mechanical milling. The retention of the octahedral coordination geometry was supported through consistent chemical shifts in ^{113}Cd and ^{31}P solid-state NMR spectra, while the lower signal-to-noise-ratio of ^{113}Cd indicated local distortion.

In addition to $Zn(HTr)_2(H_2PO_4)_2$ and $Cd(HTr)_2(H_2PO_4)_2$, four Cr, Mn, Fe, and Co-based $M^{2+}(HTr)_2(H_2PO_4)_2$ analogs were synthesized.[91] The crystal structures were determined by single-crystal X-ray diffraction, all of which demonstrated identical octahedral coordination geometries (Figure 24A). $Cr(HTr)_2(H_2PO_4)_2$ was classified as monoclinic, whereas Mn, Fe, and $Co(HTr)_2(H_2PO_4)_2$ were orthorhombic. After 120 and 240 min of mechanical milling (ZrO_2, 400 rpm) for $Cr(HTr)_2(H_2PO_4)_2$ and for Mn, Fe, and $Co(HTr)_2(H_2PO_4)_2$, respectively, only $Cr(HTr)_2(H_2PO_4)_2$ and $Mn(HTr)_2(H_2PO_4)_2$ exhibited a glassy state. In contrast, $Fe(HTr)_2(H_2PO_4)_2$ and $Co(HTr)_2(H_2PO_4)_2$ exhibited partial retention diffraction patterns. The T_g and T_c values were 62 and 90 °C, respectively, for the $Cr(HTr)_2(H_2PO_4)_2$ glass and 81 and 128 °C, respectively, for the $Mn(HTr)_2(H_2PO_4)_2$ glass. The metal-ion-dependent glass formation behavior was further discussed based on the coordination strength. The M^{2+}−N bond lengths observed in MIG-forming Cd−N, (2.288−2.321 Å), Cr−N (2.138−2.343 Å), and $Mn(HTr)_2(H_2PO_4)_2$ (2.224−2.283 Å) are larger than those of Fe−N (2.181−2.190 Å), Co−N (2.129−2.167 Å), and $Zn(HTr)_2(H_2PO_4)_2$ (2.134−2.182 Å). The lower coordination bond energy of $Cd(HTr)_2(H_2PO_4)_2$, $Cr(HTr)_2(H_2PO_4)_2$, and $Mn(HTr)_2(H_2PO_4)_2$ permits plastic deformation upon the application of mechanical stress via ball milling, while the higher bond energy of Fe, Co, and $Zn(HTr)_2(H_2PO_4)_2$ prevents deformation. After mechanical vitrification, Mn K-edge XAS and PDF validated the preservation of the local geometry and oxidation state of $Mn(HTr)_2(H_2PO_4)_2$. Although the nearest neighboring atoms of Mn^{2+} determined via EXAFS were identical with those of the pristine state, the second and higher neighboring atoms were distorted, as in $Cd(HTr)_2(H_2PO_4)_2$.[81]

Molecular doping is applicable to MIGs.[91] Ball-milling-induced vitrification of $Cd(HTr)_2(H_2PO_4)_2$ with a copresence of 0.05 and 0.10 mol ratio of diazabicyclo[2,2,2]octane (DABCO) provided homogeneous amorphous doped glasses (single T_g). 2D solid-state NMR indicated that the doped DABCO was located within 4 Å of 1,2,4-triazole. DABCO is known for its sublimation properties, high Lewis basicity, and small size. After 240 min of ball milling under an Ar atmosphere, both doped glasses exhibited no weight loss upon heating to 100 °C, where pure DABCO began to sublime even at 25 °C. This demonstrates the ability of small guests to be encapsulated in dense glasses. The transformation of DABCO into a MIG increased the T_c of the compound, extending the temperature range in which the compound exhibited the enhanced conductivity of the glass.

4.2. Ag−Tripodal Nitrile Frameworks

Two additional Ag-based tripodal nitrile ligand CPs, [Ag(mL1)(CF₃SO₃)]·2C₆H₆ and [Ag(pL2)(CF₃SO₃)]·2C₆H₆, introduced in section 3.3 (Figure 19), are considered as examples that can undergo glass transition by both melt-quenching and mechanically induced amorphization.[92,93] Hand grinding of both compounds in an agate mortar under an Ar atmosphere for 30 min is sufficient to obtain the MIGs. DSC of the MIG [Ag(mL1)(CF₃SO₃)]·2C₆H₆ indicates an identical T_g of 68 °C to that of its MQG counterpart.[92] In contrast to the MQG, the MIG exhibits a detectable exothermic recrystallization at a T_c of 130 °C. Note that hand grinding of the MQG exhibits a T_c in DSC owing to mechanically induced nucleation. The preservation of the —C≡N bonds, Ag^+ oxidation state, and coordination geometry were confirmed by FTIR, Ag K-edge XANES, and EXAFS. A hierarchical crystal/glass interface was prepared through the partial recrystallization of the monolith. Prolonged benzene vapor/liquid exposure of the hot-pressed homogeneous monolith glass induces recrystallization, where the thickness of the crystallized layer is controlled through the exposure duration (Figure 25). The heterogeneous programmable formation of crystallization domains on glass monoliths is important for the preparation of glass−ceramic materials or membrane technology, which had not been attempted for any CP/MOF glasses prior to this work.

Hand grinding for 30 min under an Ar atmosphere produced a fully amorphous [Ag(pL2)(CF₃SO₃)]·2C₆H₆ MIG.[93] Unlike $M^{2+}(HTr)_2(H_2PO_4)_2$, where ball milling results in a stable MIG, [Ag(pL2)(CF₃SO₃)]·2C₆H₆ undergoes an irreversible
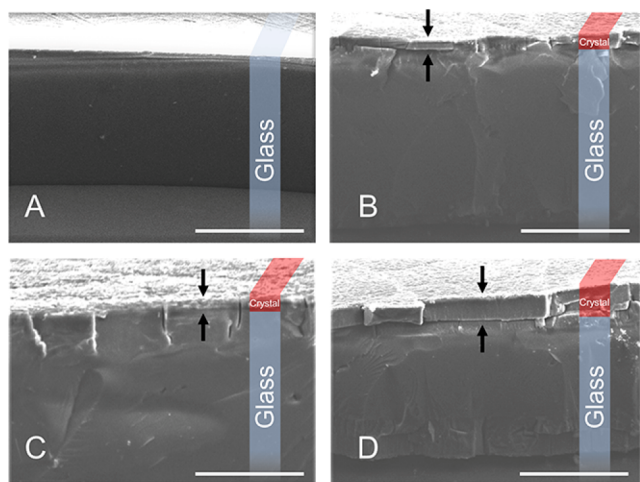
Figure 25. Cross-sectional SEM images of a $[Ag(mL1)(CF_3SO_3)] \cdot 2C_6H_6$ MIG monolith over time. (A) Pristine and after soaking in anhydrous benzene for (B) 4 h, (C) 16 h, and (D) 24 h at 25 °C. Scale bars are 100 μm. The blue and red (with arrows) sections highlight the width of the glass and the crystallized surface, respectively. Adapted with permission from ref 92. Copyright 2020 The Royal Society of Chemistry.

collapse of the network with the presence of Ag(0) in PXRD because of its lower elastic modulus. Though the mechanism has not been investigated, the reduction of Ag is potentially induced by the decomposition of ligands under a high-energy milling process. DSC revealed the presence of T_g and T_c at 107 and 117 °C, respectively. Further heating to 271 °C resulted in crystal melting. XAS was used to study the glass structure. The retention of the +1 oxidation state after solid vitrification was confirmed by Ag K-edge XANES, and the retention of nearby neighboring atoms was confirmed by Ag K-edge EXAFS. Because pL2 is a π-conjugated rigid ligand, a slight distortion of the coordination geometry for each Ag$^+$ should be sufficient to propagate the overall periodicity. PDF analysis of the $[Ag(pL2)(CF_3SO_3)] \cdot 2C_6H_6$ MIG revealed the retention of correlated pairs, even over 7 Å, owing to the rigidity and size of the ligand.

4.3. Zeolitic Imidazolate Frameworks

Extended milling of ZIF-62 isomorphs (Figure 10) Zn-$(Im)_{2-x}(bIm)_x$ (x = 0.3, 0.5, 1.0) during mechano-synthesis results in MIGs, with T_g ranging between 318 and 411 °C.[171] The observed values are lower than those of their MQG counterparts. The difference in thermal behavior is hypothesized to be the result of the differences in particle size. Further

heat treatment of the MIG at 450 °C ($>T_m$) induces particle agglomeration (sintering), thus increasing T_g to values observed in MQG of ZIF-62.

5. DIRECT SYNTHESIS OF GLASSES

The direct synthesis of CP glasses has been demonstrated as an alternative to multistep glass preparation. Unlike MQGs and MIGs, the CP glasses in this class are significantly harder to characterize owing to the lack of an exact composition and single-crystal structure. The chemical and structural determinations mostly rely on the information accumulated from elemental analysis; XAFS, PDF, and MAS NMR measurements; and reverse Monte Carlo simulations. Thus, far, H$^+$-conductive $(dema)_{0.35}[Zn(H_2PO_4)_{2.35}(H_3PO_4)_{0.65}]$ (dema = diethylmethylammonium cation) glass synthesized from protic ionic liquid $[dema][H_2PO_4]$ is one of only a few examples in this family so far.[31] Protic ionic liquid $[dema][H_2PO_4]$ was utilized both as a H$^+$ carrier and a bridging ligand for redox-inactive Zn^{2+} (Figure 26A). The CP glass was directly synthesized by the neutralization of zinc oxide (ZnO), dema, and H$_2$PO$_4^-$. The chemical composition was characterized using ^{1}H MAS NMR and elemental analysis. In addition to diffuse PXRD scattering, the presence of T_g at −22 °C confirmed its glassy nature (Figure 26B). A fitted XAFS analysis with an average coordination number of 4.6 suggested that some H$_2$PO$_4^-$/H$_3$PO$_4$ act as bridging ligands and confirmed the formation of the Zn^{2+}−H$_2$PO$_4^-$/H$_3$PO$_4$ coordination network. PDFs confirmed the assignments of two distinct Zn−Zn correlations: a single μ-oxygen atom of the PO$_4^{3-}$ (3.38 Å) and two oxygen atoms of PO$_4^{3-}$ (4.22 Å). The coordination network structure was finally demonstrated via a reverse Monte Carlo simulation (Figure 26C).

Another family of direct synthesis amorphous glasses is the gold thiolate CPs.[34] Unlike the previous case, in which the crystal structure is unknown, gold thiolate can be synthesized in crystalline and glassy states.[34,172] This family is composed of gold-based glasses comprising 1D double-helix interpenetrated spiral chains of −Au−S−Au−S−, where the linkers are thiophenolate Au(SPh), phenylmethanethiolate Au(SMePh), or phenylethanethiolate Au(SEtPh) (Figure 27). Mechanical pressurization at 0.67 GPa under ambient atmospheric conditions provided a transparent glass pellet. TMA verified the presence of glass with T_g at 72, 57, and 51 °C for Au(SPh), Au(SMePh), and Au(SEtPh), respectively, where T_g decreased with increasing alkyl chain length. PDF measurements confirmed the retention of molecular networks, where the Au−S (2.3 Å) and Au−Au (3.5 Å) connectivity was preserved in the amorphous phase. Some positional correlations of the

Table 2. Selected Properties of MIGs

materials[a]	dimensionality	T_g (°C)	T_c (°C)	functionality	ref
phosphate−azole frameworks (M^{2+}(1,2,4-triazole)$_2$(H$_2$PO$_4$)$_2$)					
Cd(HTr)$_2$(H$_2$PO$_4$)$_2$	2D	79−90	104−142	anhydrous H$^+$ conductivity	81
Cr(HTr)$_2$(H$_2$PO$_4$)$_2$	2D	62	90	anhydrous H$^+$ conductivity	91
Mn(HTr)$_2$(H$_2$PO$_4$)$_2$	2D	81	128	anhydrous H$^+$ conductivity	91
Ag-tripodal nitrile frameworks					
$[Ag(mL1)(CF_3SO_3)] \cdot 2C_6H_6$	2D	68	102	porosity	92
$[Ag(pL2)(CF_3SO_3)] \cdot 2C_6H_6$	3D	107	117	porosity	93
zeolitic imidazolate frameworks					
Zn(Im)$_{2-x}$(bIm)$_x$ (x = 0.35, 0.5, 1.0)/ZIF-62	3D	318−411		porosity	171

^{a}See Abbreviations.
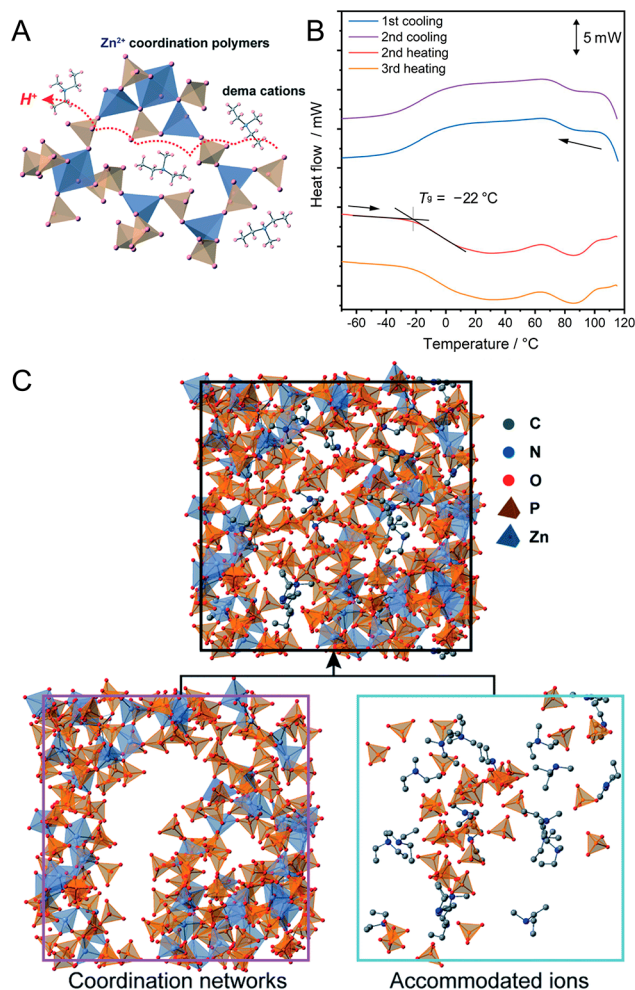
Figure 26. Direct synthesis of CP glass (dema)$_{0.35}$[Zn(H$_2$PO$_4$)$_{2.35}$ (H$_3$PO$_4$)$_{0.65}$] (dema = diethylmethylammonium). (A) Schematic of the structure; blue and orange polyhedral represent Zn^{2+} and H$_n$PO$_4$, respectively. (B) DSC profiles under Ar atmosphere at 10 °C min^{-1}. (C) Unit cell of the amorphous structure modeled by an RMC simulation. The coordination network and captured free dema and H$_2$PO$_4^-$/H$_3$PO$_4$ are presented separately. Reprinted with permission from ref 31. Copyright 2020 The Royal Society of Chemistry. https://creativecommons.org/licenses/by/3.0/.

double helix chains were confirmed in the PDF at ∼11.5 Å. A better description of the distorted double-helix interpenetrated orientation was confirmed via PDF and Au-L$_3$ XANES fitting, thus excluding the possibility of the tetramer ring conformation.

A liquid-forming glass does not have to undergo vitrification by fast cooling. A class of metal-containing ionic liquids exhibit a liquid-to-glass phase transition upon light irradiation and reversibly return to the ionic liquid by melting.[117,173−175] The ionic liquids are composed mainly of cationic organometallic sandwich complexes with nitrile-based anions. Depending on the synthesis conditions, a combination of [Ru(C$_5$H$_5$)-(MeCN)$_3$]X (X = FSA$^-$ or PF$_6^-$) and 1,3,5-C$_6$H$_3$(OC$_6$H$_{12}$CN)$_3$ ligands selectively yields a colorless viscous ionic liquid or yellow amorphous CP.[173] The ionic liquid and the amorphous CP exhibit T_g of −53 and 0 °C, respectively. UV irradiation of the ionic liquid triggers a phase transition to the CP glass (Figure 28). Additionally, heating the solid at 90 °C for 30 min or 130 °C for 1 min recovers the
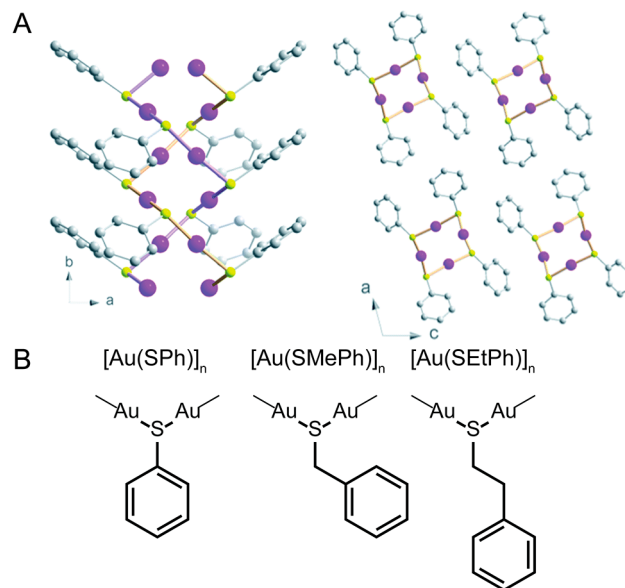
Figure 27. (A) Crystal structure of 1D Au(SPh). Pink, yellow and gray spheres represent gold, sulfur and carbon atoms, respectively. (B) Representation of Au(SPh) and two other related CPs. Reprinted with permission from ref 34. Copyright 2020 The Royal Society of Chemistry. https://creativecommons.org/licenses/by/3.0/.
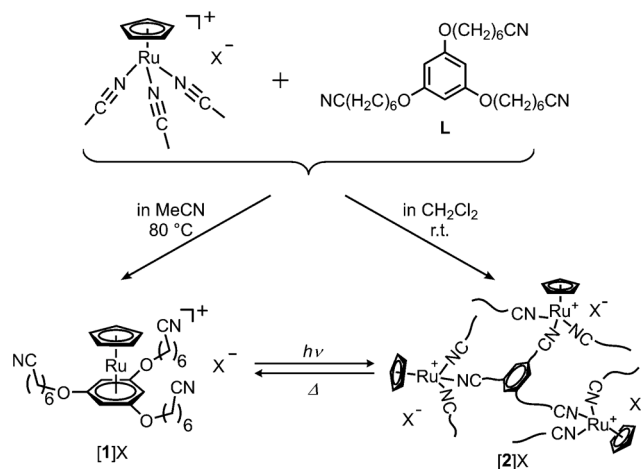
Figure 28. Reactions of [Ru(C$_5$H$_5$)(MeCN)$_3$]X (X = FSA$^-$, PF$_6^-$) and **L**. Conversion between [**1**]X and [**2**]X occurs for X = FSA$^-$. Reprinted with permission from ref 173. Copyright 2016 The Royal Society of Chemistry.

ionic liquid. Similar behavior was observed in [Ru(C$_5$H$_5$)-(C$_6$H$_5$R)][B(CN)$_4$] (R = butyl, ethyl, octyl) ionic liquids, which transform into amorphous CPs with the formula Ru(C$_5$H$_5$)[B(CN)$_4$].[174] The transition is triggered by UV irradiation together with the elimination of the arene ligand. Interestingly, the N$_2$ isotherm at 77 K indicates the presence of micro and macroporosity in the solid phase, with a Brunauer−Emmett−Teller (BET) surface area and total pore volume of 202 m^2 g^{-1} and 0.27 mL g^{-1}, respectively. Another Ru-containing poly(ionic liquid), [Ru(C$_5$H$_5$)-[C$_6$H$_3$(OC$_6$H$_{12}$CN)$_3$]]$^+$, and a polymeric anion, [CH$_2$−CH(SO$_2$N−SO$_2$CF$_3$)]$_n$, undergo a UV-induced phase transition.[175] UV irradiation initiates the photochemical reaction of the cation, resulting in a cationic coordination network and anionic covalent chains (T_g = −8 °C). In addition to the
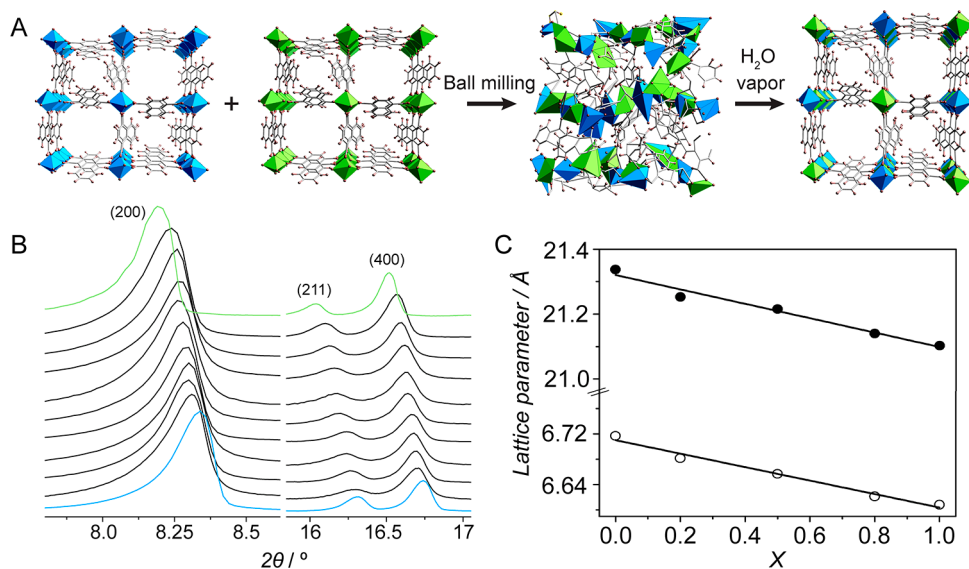
Figure 29. Mechanical alloying of MOFs through a reversible crystal-to-amorphous/glass transformation. (A) Schematic of Al-ndc and Ga-ndc MOF alloy formation through a mechanical amorphization and vapor-assisted crystallization process. (B) PXRD patterns showing peaks of the (200), (211), and (400) crystal planes of Al-ndc (blue), Ga-ndc (green), and their mixtures (9:1 to 1:9, black) under an Ar atmosphere. (C) Lattice parameters $a = b$ (filled circle) and c (white circle) from Pawley analysis with a variable Al-ndc content (X) in Ga-ndc crystals. Reprinted with permission from ref 177. Copyright 2017 John Wiley and Sons.

synthesis of ionic liquids, the formation of 2D and 3D crystalline anionic CPs containing organometallics and ionic liquids has been demonstrated.[117] Although they exhibit crystal melting (T_m = 102−239 °C), the melts consist of solid $M[C(CN)_3]$ and an ionic liquid. A reverse process is observed in 3D MOFs, which melt upon irradiation by a femtosecond laser pulse.[176] Although the process results in products equivalent to the decomposition of CPs/MOFs, this opens an additional pathway to initiate the phase transition in CPs/MOFs.

6. HYBRIDIZATION AND MORPHOLOGICAL CONTROL

Deviation from perfectly ordered crystals and phase transitions provides numerous possibilities for CP/MOF glass fabrication. Reversible crystal-to-glass/amorphous transformations allow uniform mixing of two distinct MOF parents in a "softer" state, whereas the recrystallization process of the solid solution permits the recovery of crystalline alloys.[177] The mechanical alloying of Al(ndc)(OH) (ndc = 1,4-naphthalenedicarboxylate, Al-ndc) and Ga(ndc)(OH) (Ga-ndc) was studied at various Al-ndc/Ga-ndc ratios, ranging from 1:9 to 9:1. The mixture was amorphized by ball milling at 400 rpm for 1 h under an Ar atmosphere. The compound was then recrystallized through 72 h of a vapor-assisted method with saturated water vapor at 25 °C (Figure 29A). The sub-Ångström pore channels can be controlled because the (200), (211), and (400) Bragg peaks gradually shift as the composition varies (Figure 29B). The linear relationship between the lattice spacing and the composition of Al-ndc/Ga-ndc verifies the formation of proportional solid solutions, which follow Vegard's law (Figure 29C). In addition to the Al-ndc/Ga-ndc system, EXAFS studies of amorphized Al-ndc/Ga-ndc, $Cu_3(1,3,5$-benzenetricarboxylate$)_2$ (Cu-HKUST-1), Zn(2-methylimidazolate)$_2$ (Zn-ZIF-8), and $Zn_2(2,5$-dihydroxy-1,4-benzenedicarboxylate) (Zn-MOF-74) confirmed the retention of their coordination number and bond distances around the metal centers after they

transitioned from the crystalline to the amorphous state. Although this work did not study the DSC data of the amorphous materials, the technique can be applied to other MIGs of CP/MOF systems.

The presence of a stable liquid state in some CPs/MOFs allows the development of more sophisticated hybrid glasses, in which solid solution constraints can be ignored. Consequently, the resulting products are not limited to a homogeneous mixture of both parents (Figure 30).[45] The first example in the class is melt-state blending of meltable ZIF-62 (T_m = 437 °C) and ZIF-4-Zn (T_m = 587 °C).[36] Melt-quenching the premixed ZIFs at 590 °C for 2 min results in a

Figure 30. Schematic representation of various approaches for hybrid glass formation. Reprinted with permission from ref 45. Copyright 2019 The Royal Society of Chemistry.
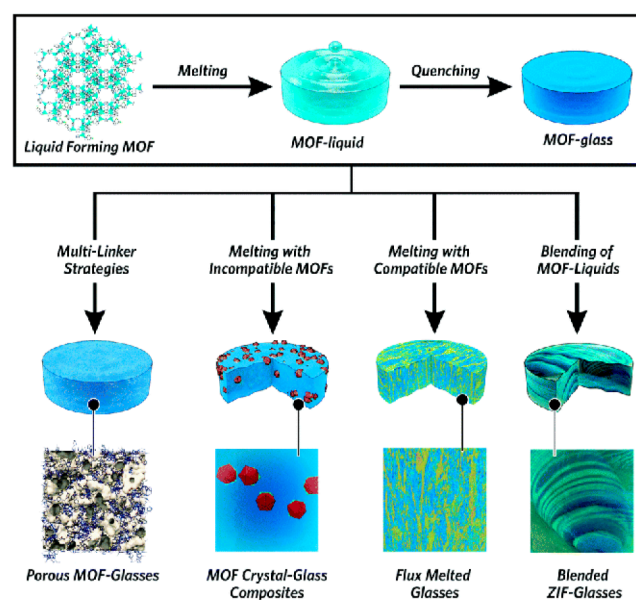
blended ZIF glass with a variable T_g controlled by the ZIF-4-Zn/ZIF-62 composition (Figure 31A). Complete mixing of
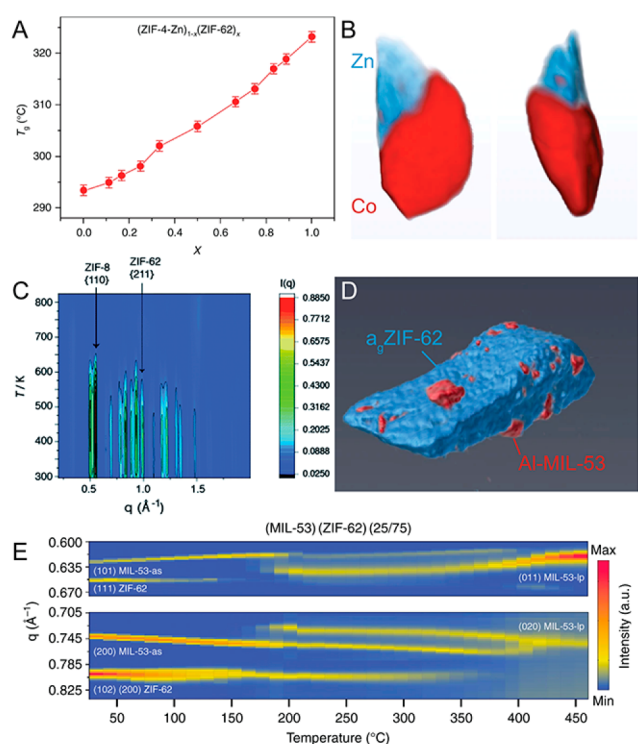

Figure 31. (A) Evolution of the T_g of $(ZIF-4-Zn)_{1-x}(ZIF-62)_x$ glasses. (B) Volume rendering of the tomographic reconstructions from EDS chemical mapping of $(ZIF-4-Zn)_{0.5}(ZIF-62)_{0.5}$. Reprinted with permission from ref 36. Copyright 2018 Springer Nature Limited under Creative Commons license CC BY 4.0. https://creativecommons.org/licenses/by/4.0/. (C) Temperature resolved WAXS diffraction of $(ZIF-8)_{0.2}(ZIF-62)_{0.8}$. Reprinted with permission from ref 178. Copyright 2019 The Royal Society of Chemistry. https://creativecommons.org/licenses/by/3.0/. (D) 3D tomography of the $(Al-MIL-53)_{0.25}(ZIF-62)_{0.75}$ CGC. (E) Contour plots of in situ synchrotron PXRD measurements during the thermal treatment (10 °C min^{-1}) of $(Al-MIL-53)_{0.25}(ZIF-62)_{0.75}$. Reprinted with permission from ref 38. Copyright 2019 Springer Nature Limited under Creative Commons license CC BY 4.0. https://creativecommons.org/licenses/by/4.0/.

both phases provides a single T_g, whereas insufficient grinding affords two distinguishable T_g values. Interfacial binding at the boundary of each domain in the ZIF-4-Co/ZIF-62 glass blend was confirmed via annular dark-field STEM electron tomography.[109] The highly viscous nature of ZIFs prevents complete homogeneous mixing on a microscopic scale (Figure 31B).

Because most CPs/MOFs decompose upon thermal activation prior to reaching T_m, flux melting might be an alternative route to force melting.[178] In contrast to ZIF-4 and ZIF-62, the T_m of ZIF-8 is inaccessible in its pure form ($T_d < T_m$). The lowering of T_m via flux melting is well-known for inorganic molten salts. Similarly, the liquid state of ZIF-62 was utilized as a solvent for ZIF-8. By mixing 20 wt % ZIF-8 with 80 wt % ZIF-62, DSC revealed a higher T_m than that of pristine ZIF-62. Moreover, the quenched glass did not contain any Bragg peaks and exhibited a single T_g, suggesting the successful crystal-to-glass transformation of ZIF-8 through thermal stimulus. In situ wide-angle X-ray scattering (WAXS)

elucidated the flux-melting mechanism. Amorphization of ZIF-62 occurred first at ~327 °C, followed by the disappearance of the Bragg diffraction of ZIF-8 above 377 °C (Figure 31C). The incorporation of an ionic liquid 1-ethyl-3-methylimidazolium bis(trifluoromethanesulfonyl)-imide, [EMIM][TFSI], into ZIF-8 pores results in an accessible T_m at 322 °C as well.[179] Ionic liquid helps compensate for the barrier to melting by stabilizing the rapidly dissociated ZIF-8 upon heating. It reduces T_m of ZIF-8.

This class of hybrid glasses comprises composite pairs in which one component retains its glassy state after quenching. Similar to a mixed matrix membrane (MMM), a crystal−glass composite (CGC) employs MOF glasses instead of conventional polymers as a matrix.[38] To achieve a crystal−glass composite, a glass matrix with a wide stable liquid state, such as ZIF-62, is required (T_m = 430 °C, T_d = 550 °C). Additionally, two crucial requirements for the crystalline component are high thermal stability, at least above the T_m of the glass phase, and chemical incompatibility to prevent flux melting. Examples have been demonstrated with flexible Al(OH)(BDC) (Al-MIL-53) or rigid $Zr_6O_4(OH)_4(BDC)_6$ (UiO-66) crystals. BDC denotes 1,4-benzenedicarboxylate. Twenty-five wt % Al-MIL-53 or UiO-66 was mixed with 75 wt % ZIF-62 and melt-quenched at 450 °C to obtain CGCs. STEM-EDS revealed distinguishable domains of MOF crystals between 30−300 nm embedded throughout the ZIF glass matrix (Figure 31D). While ZIF-62 was vitrified into a glassy matrix, PXRD of the CGC revealed the retention of crystalline MIL-53 with a transition to an open-pore structure (MIL-53-lp) because of the thermal activation (Figure 31E). The open-pore structure in the CGC was stable for over a year under ambient conditions. Conventionally, exposure of MIL-53-lp (lp = large pore) to moisture causes pore contraction to MIL-53-np (np = narrow pore) within 1 h through the interaction of guest water molecules. A subsequent study revealed the relationship between the MIL-53 loading content and the stability of the open-pore phase.[37] Rietveld refinement indicated that metastable MIL-53-lp was stabilized at a maximum fraction of 60−70 wt %. Above this limit, some of the MIL-53-lp is transformed into the MIL-53-np phase upon cooling. In addition to MIL-53, the CGC techniques are applicable to a library of thermally stable MOFs, such as MIL-118 and UL-MOF-1.[180] Because extended heating above the T_m of the ZIF-62 glass matrix is necessary, not all MOFs can withstand the high processing temperature required by the standard CGC method. An alternative approach via thermal annealing above T_g at 400 °C for 5 h of pressed pellets is available for the formation of stable CGCs.[181]

Thus, far, we have only covered hybrid composites with two MOF parents. Combining ZIF glasses with inorganic glasses or organic polymers is also possible because of the versatile processability of glass.[108,182] With the aim of overcoming the interfacial contact between porous MOF and polymer for better separation, an in situ melting and vitrification technique was proposed.[182] Thermal treatment of nonstoichiometric ZIF-62, $Zn(Im)_{1.95}(bIm)_{0.05}$, and Polyimide 6FDA-DAM [6FDA = 2,2-bis(3,4-carboxyphenyl)-hexafluoropropanedianhydride, DAM = 2,4,6-trimethyl-m-phenylenediamine] composite reduced the volume fraction of voids by 79%, thus enhancing the CO_2/N_2 selectivity as compared to crystal-polymer composite by void filling of ZIF-62. The selectivity decreases as ZIF-62 content reaches 30 wt % due to the formation of interfacial voids. Phosphate glasses,

$(1-x)([Na_2O]_z[P_2O_5])-x([AlO_{3/2}][AlF_3]_y)$, with a low T_g of 310−450 °C were chosen as representative materials.[108] Although the heat treatment did not exceed T_m, the "softer" character of phosphate glasses above T_g is expected to aid mixing between the two phases. Equivalent masses of ZIF-62 and phosphate glass were physically mixed and heated at 450 °C to obtain the composite material. The absence of substantial overlap between the Zn and Al EDS signals, as well as the presence of two distinct T_g values from the ZIF-62 and phosphate glasses in DSC, indicated that the composite had two distinct domains. This work supports the possibility of bond formation at the interface of both domains. This was confirmed by the appearance of a Na−N peak at ∼145 cm^{-1} in the Raman spectra, as well as the formation of terminal oxygen of the phosphate and PO_3N/PO_2N_2 species, which was detected by ^{31}P MAS NMR.

7. PROPERTIES AND FUNCTIONS

7.1. Ionic Conductivity

7.1.1. H$^+$ Conductivity. CPs/MOFs can achieve a higher ionic conductivity in the amorphous or glassy state than that of their crystalline counterparts owing to enhanced ion dynamics and isotropic conducting paths.[183] Furthermore, shaping versatility enables the fabrication of thin films as well as grain-boundary-free conductors. Although the melting and glass transformation of H$^+$-conductive CPs were thoroughly established in $[Zn(HPO_4)(H_2PO_4)](H_2Im)_2$,[26,51,184] Zn-$(H_2PO_4)_2(HTr)_2$,[26,52] and $[Zn_3(H_2PO_4)_6(H_2O)_3](HbIm$, Figure 4).[26,53] The first demonstration of enhanced conductivity in a CP glass was studied in a $Cd(HTr)_2(H_2PO_4)_2$ MIG (Figure 24).[81] The H$^+$ conductivity was enhanced by 2 orders of magnitude from 8×10^{-7} S cm^{-1} at 150 °C in the pristine crystalline state to 1.0×10^{-4} S cm^{-1} at 125 °C for the MIG (Figure 32A). The faster H$^+$ dynamics promoted by the higher acidity and isotropy of $H_2PO_4^-$ were confirmed through the downfield chemical shift in the ^{31}P MAS NMR spectrum. A similar behavior was observed for isostructural $M^{2+}(HTr)_2(H_2PO_4)_2$.[91]

The melting and vitrification processes enable the encapsulation of functional molecules into CP glasses.[185] Doping a photofunctional molecule, trisodium 8-hydroxy-1,3,6-pyrenetrisulfonate (pyranine), into a transparent H$^+$ conductive glass, $[Zn(HPO_4)(H_2PO_4)](H_2Im)_2$ (Figure 4), allows the overall conductivity to be controlled by light irradiation (Figure 32B). In response to light irradiation, ROH generates mobile H$^+$ and RO^{-*} species, increasing the overall number of charge carriers in the system. Once irradiation ends, the excited RO^{-*} returns to its original RO$^-$ state and ROH form via thermodynamically driven H$^+$ recombination. As a result, the number of charge carriers and, consequently, the conductivity decrease. The reversible pK_a changes upon 365 nm light exposure between the ground and excited states of the photoacid provide reversible control of the overall H$^+$ concentration and conductivity (Figure 32C).

Acid-doped crystalline compounds can be fabricated through a reversible crystal-to-glass transformation.[185] Trifluoromethanesulfonic acid (CF_3SO_3H) was incorporated into a $[Zn(HPO_4)(H_2PO_4)](H_2Im)_2$ melt, which then underwent mechanically induced recrystallization. This resulted in enhanced conductivity in the crystalline phase without changes in the coordination geometry. The conductivity of 15 mol % CF_3SO_3H-doped crystalline $[Zn(HPO_4)(H_2PO_4)](H_2Im)_2$
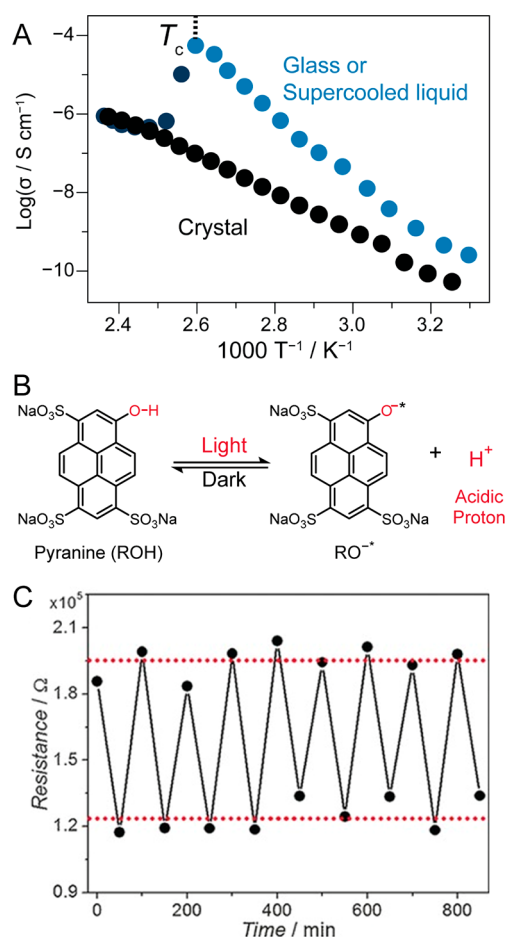
Figure 32. (A) Temperature-dependent H$^+$ conductivity of the crystalline and glassy states of $Cd(HTr)_2(H_2PO_4)_2$. (B) Schematic of H$^+$ conductivity switching by UV irradiation in a $[Zn(HPO_4)-(H_2PO_4)](H_2Im)_2$ MQG doped with a photoacid, 8-hydroxy-1,3,6-pyrenetrisulfonate (pyranine). (C) Reversible optically controlled (365 nm irradiation) H$^+$ conductivity in $[Zn(HPO_4)(H_2PO_4)]-(H_2Im)_2$ doped with 5 mol % pyranine. Reprinted with permission from ref 185. Copyright 2017 John Wiley and Sons.

was enhanced to 2.0×10^{-7} and 2.7×10^{-4} S cm^{-1} from 3.2×10^{-9} and 2.1×10^{-5} S cm^{-1} for the pristine sample at 30 and 110 °C, respectively.

The coexistence of H$^+$ conductivity and guest-accessible porosity in a CP glass was demonstrated in $[Zn_2(HPO_4)_2(H_2PO_4)](ClbImH^+)_2(H_2PO_4)(MeOH)$ (Figure 4).[125] Although the activated crystalline state did not conduct H$^+$ under humid conditions, the guest-accessible space in the CP glass and distorted components enabled an efficient transport pathway for H$^+$ conductivity, resulting in conductivity of 1.2×10^{-4} S cm^{-1} at 25 °C and under 98% relative humidity.

Direct synthesis of a CP glass from a protic ionic liquid was demonstrated to provide a promising moldable solid-state H$^+$ conductor.[31] Although most ionic liquids have an applicable H$^+$ conductivity, their low viscosity and low transport number range (0.5−0.6) prevent them from being efficient and versatile conductors.[186] Synthesis of $(dema)_{0.35}[Zn-(H_2PO_4)_{2.35}(H_3PO_4)_{0.65}]$ glass (Figure 26) from protic ionic liquid $[dema][H_2PO_4]$ yields a H$^+$ conductivity of 13.3 mS cm^{-1} at 120 °C (Figure 33A),[31] which is twice that of the parent ionic liquid $[dema][H_2PO_4]$ (6.5 mS cm^{-1} at 120 °C).
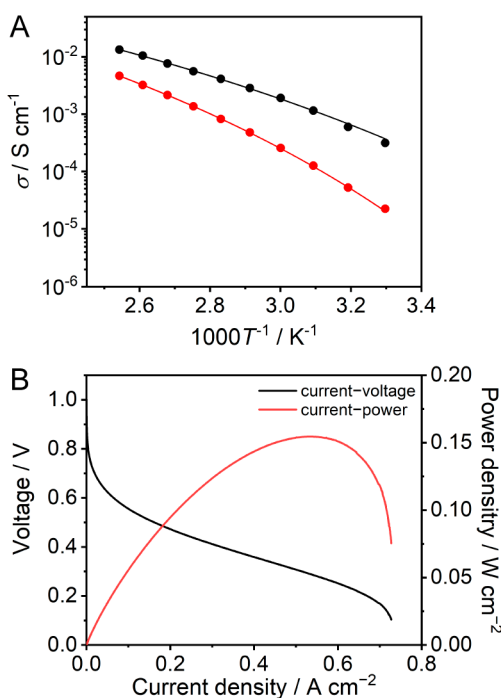
Figure 33. (A) H^+ conductivity as a function of temperature under anhydrous conditions of $(dema)_{0.35}[Zn(H_2PO_4)_{2.35}(H_3PO_4)_{0.65}]$ glass (black) and protic ionic liquid $[dema][H_2PO_4]$ (red). (B) $I–V$ (black) and $I–W$ (red) curves of a H_2/O_2 fuel cell employing $(dema)_{0.35}[Zn(H_2PO_4)_{2.35}(H_3PO_4)_{0.65}]$ glass as an electrolyte at 120 °C without humidification. Reprinted with permission from ref 31. Copyright 2020 The Royal Society of Chemistry. https://creativecommons.org/licenses/by/3.0/.

The transition of the dominant conductivity mechanism from the vehicle mechanism in the ionic liquid to the Grotthuss mechanism in the CP glass promotes a more efficient H^+ transport pathway. The formation of a coordination bonding network in the CP glass restricts the mobility of anionic species. Consequently, H^+ dominates the overall conductivity, resulting in a high H^+ transport number of 0.94. Without any restriction in anion movement, $[dema][H_2PO_4]$ exhibits an H^+ transport number of 0.49. Furthermore, an anhydrous H_2/O_2 fuel cell fabricated from a polytetrafluoroethylene (PTFE) membrane impregnated with $(dema)_{0.35}[Zn-(H_2PO_4)_{2.35}(H_3PO_4)_{0.65}]$ exhibited a maximum power density of 0.15 W cm^{-1} at 0.96 V and 120 °C (Figure 33B).

The operating temperatures of an emerging class of H^+ batteries have been increased through the application of MQGs.[32] Optimization of the hydrogen-bonding network in $[Zn_3(H_2PO_4)_6(H_2O)_3](BTA)$ (Figure 4) by substituting 1,3-benzimidazole with a lower pK_a 1,2,3-benzotriazole improves the crystalline conductivity by approximately six times at 60 °C. After melt-quenching, $[Zn_3(H_2PO_4)_6(H_2O)_3](BTA)$ exhibits a H^+ conductivity of 8.0×10^{-3} S cm^{-1} (Figure 34A) with a transport number of 1.0 at 120 °C. A low T_m and mechanical softness above T_m (42.8 Pa s at 120 °C), which is comparable to the viscosity of soda–lime–silica glass above 1100 °C, allow the fabrication of grain-boundary-free solid electrolytes with flawless electrode–electrolyte interfaces without decomposition of the electrode material (Figure 34B and 34C). A rechargeable anhydrous solid-state H^+ battery with a wide operating temperature range (25−110 °C) was

first demonstrated with a full-cell discharge capacity of 55.4 mA h g^{-1} at 25 °C (Figure 34D).

7.1.2. Li^+ Conductivity. Until now, research on conductive CP glasses has been dominated by H^+ conductivity, but interest in other metal ions is emerging.[30] 3D tetrahedrally coordinated $Li[N(SO_2F)_2](NCCH_2CH_2CN)_2$ (Figure 20A) exhibits a reversible solid−melt transition with a T_m of 59.5 °C. By minimizing the interaction between Li^+ (hard acid) and the conduction paths (SN, soft base), the compound exhibits high Li^+ conductivities of 1×10^{-4} S cm^{-1} at 30 °C and 1×10^{-5} S cm^{-1} at −20 °C with a Li^+ transport number of 0.95. An all-solid-state lithium battery was fabricated by melting and solidifying the CP between a thin-film $LiCoO_2$ cathode and a Li metal anode (Figure 35). The battery demonstrated a capacity retention of 90% of the initial discharge capacity after 100 cycles. Additionally, the reversible phase-transition behavior of the CP at moderate temperatures allowed self-healing of cracks that formed during operation.

Vitrification enables the exploration of unique features in ZIFs. Encapsulating lithium bis(trifluoromethanesulfonyl)-imide (LiTFSI) in propylene carbonate (equivalent to 2.9 M) to glassy ZIF-4 yields quasi-solid-state electrolytes (QSSEs).[187] Owing to the grain boundary-free and isotropic properties, the glassy host exhibits high Li^+ conductivities of 1.6×10^{-4} S cm^{-1} at 30 °C and 6.0×10^{-5} S cm^{-1} at −56.6 °C with a Li^+ transport number of 0.89, which are higher than the conductivity values observed in crystalline counterparts (8.2×10^{-5} S cm^{-1} at 30 °C, 4.5×10^{-7} S cm^{-1} at −56.6 °C, and a transport number of 0.51). When paired with a $LiFePO_4$ cathode, the glassy QSSE cell retains a discharge capacity of 101 mAh g^{-1} for 500 cycles at 1 C. In addition to Li^+ conductivity, vitrification of the redox-active Co ZIF-4 anode results in an enhanced specific capacity of 306 mAh g^{-1} compared to 157 mAh g^{-1} for its crystalline counterpart after 1000 cycles at 2 A g^{-1}.[188]

7.2. Optical Properties

7.2.1. Transparent and Luminescent. The intrinsic transparency, processability, and isotropic homogeneity of CP/MOF glasses enable the design of functional glasses for optical applications.[26] Luminescence of a CP glass was first demonstrated in lanthanide-based $Eu(hfa)_3(p\text{-}dpeb)$ (Figure 36).[33,189,190] The design combines the benefits of the lanthanide metal center with 4f−4f emissions of the parity-forbidden transition with the prevention of $\pi-\pi$ and $CH-\pi$ interactions via the ethynyl group in the ligand. The compound exhibits strong luminescence with a 4f−4f emission quantum yield (ΦLn) of 86% and an emission lifetime of 0.93 ms at room temperature. (1-butyl-4-methyl-pyridinium)$[Cu(SCN)_2]$ exhibits melting at 91 °C.[148] The luminophore bridging ligand (SCN^-) alone can trigger a small but detectable luminescence with a quantum efficiency of 0.90% and a lifetime of 131 ns at room temperature.

Considering the possibility of both thermally and mechanically induced decomposition, it is challenging to process intrinsically "soft" CP/MOF glasses without deleterious effects.[112] The highly viscous liquid state of ZIF-62 melts prevents the formation of transparent, bubble-free glass monoliths using the conventional melt-quenching technique. This issue is overcome by using the vacuum hot-press method (Figure 37A). Hot-pressed ZIF-62 glass has a high transmittance of up to 90% for visible and near-infrared wavelengths, which is comparable to that of oxide glasses (Figure
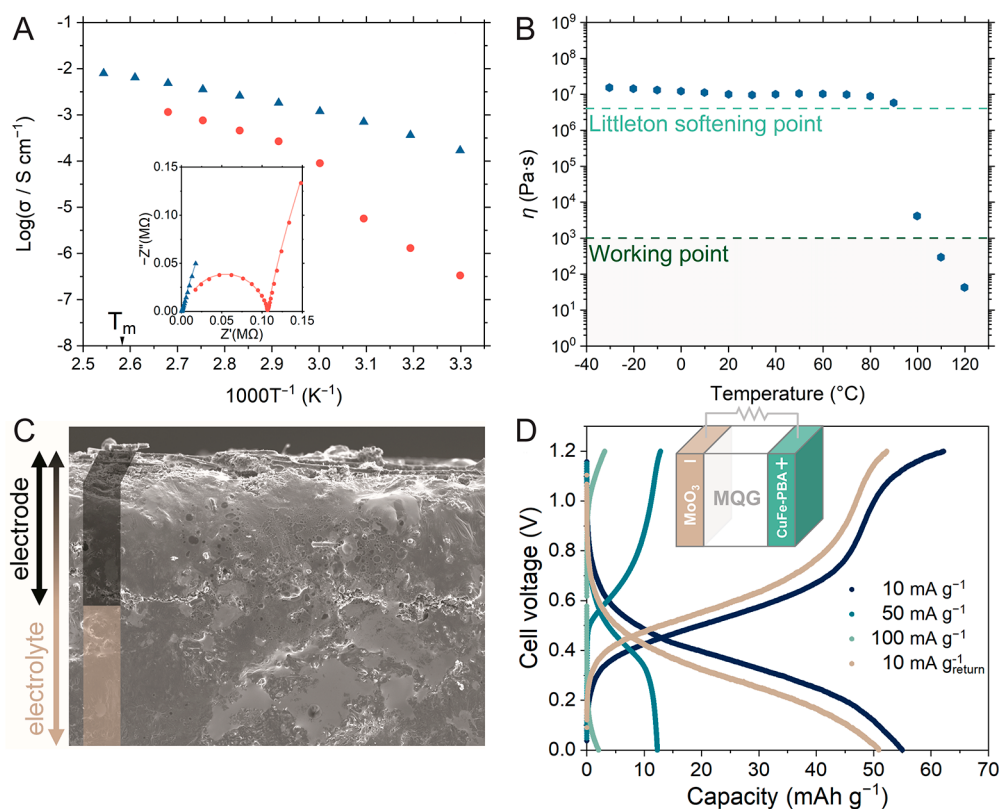
Figure 34. (A) Arrhenius plots of the anhydrous H⁺ conductivity of a $[Zn_3(H_2PO_4)_6(H_2O)_3](BTA)$ degas crystal (●) and MQG (▲) under an Ar atmosphere. (B) Temperature-dependent viscosity (η). (C) Cross-sectional SEM images (150× magnification) of the electrode−solid-state electrolyte interface. (D) Charge−discharge profiles of a fuel cell utilizing the MQG as a solid-state electrolyte at 10 mA h g^{-1} and 25 °C. Prussian blue analogs cathode is denoted as PBA. Adapted with permission from ref 32. Copyright 2021 The Royal Society of Chemistry. https://creativecommons.org/licenses/by/3.0/.
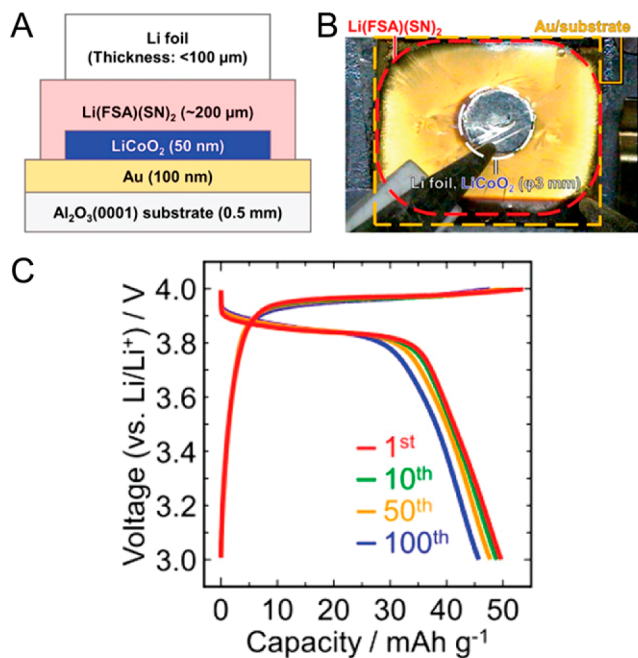
Figure 35. (A) Cell configuration and (B) top-view photograph of Li-battery $(Li|Li[N(SO_2F)_2](NCCH_2CH_2CN)_2|LiCoO_2|Au)$. (C) Charge−discharge profiles at a current density of 1 μA cm^{-2}. Reprinted with permission from ref 30. Copyright 2021 American Chemical Society.
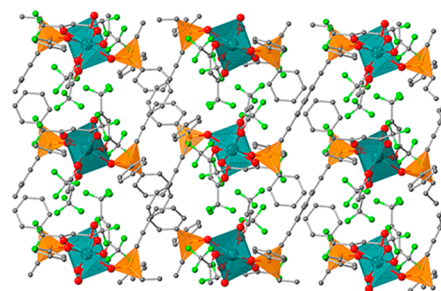
Figure 36. Crystal structure of $Eu(hfa)_3(p\text{-dpeb})$. Eu, C, P, O, and F atoms are represented by teal, gray, orange, red, and green spheres, respectively.

37B). Although the refractive index was measured to be ∼1.56 via the Becke line method, its Abbe number of 31 locates it in the upper range of polymers in the refractive index−Abbe number diagram. Additionally, the refractive index of ZIF-62 glass can be tuned by varying the linker (bIm:Im) ratio during synthesis.

Co^{2+} substitution in ZIF-62 glass introduces a photonic functionality in the range of broadband mid-infrared (mid-IR, 1.5−4.8 μm) luminescence.[140] A series of $Zn_{1-x}Co_x(Im)_{1.7}(bIm)_{0.3}$ glasses, where x = 0, 0.1, and 0.5, were produced by hydrothermal synthesis followed by melt-quenching. While pure Zn ZIF-62 did not exhibit any luminescence, the emission intensity strengthened with an increasing Co^{2+} fraction owing to the d−d transition.

A

B
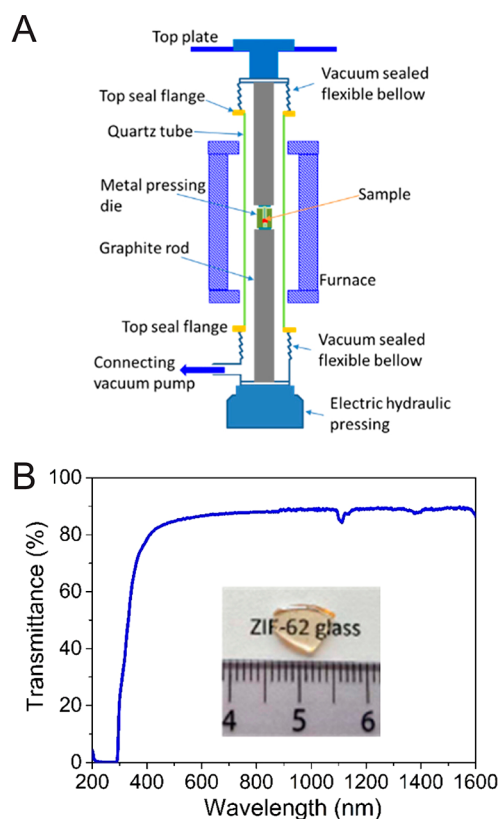
Figure 37. (A) Schematic of the hot-pressing facility. (B) Transmittance curve of polished ZIF-62 MQG. Adapted with permission from ref 112. Copyright 2019 The Optical Society.

Additionally, the mid-IR luminescence of Co^{2+}-containing ZIF-62 was stronger than that of its crystalline counterpart.

Transparent and luminescent glasses are not limited to CPs/MOFs with stable liquid states. Transparent and red-emissive gold thiolate CP glasses have been fabricated through uniaxial compression of amorphous powder samples at 0.67 GPa under ambient atmospheric conditions.[34] Three examples of double-helix interpenetrated spiral chain gold-based glasses are Au(SPh), Au(SMePh), and Au(SEtPh) (Figure 27). The yellow glass pellets of Au(SPh) and Au(SMePh) begin to transmit light at 430 nm and reach a maximum transmittance of 19% at 850 nm, whereas the transparent nature of colorless Au(SMePh) begins at 400 nm and reaches a maximum value of 26% at 850 nm. The luminescent properties of d^{10} gold thiolates arise from aurophilic interactions that induce the ligand-to-metal charge transfer process. Au(SPh) and Au(SEtPh) are emissive below −23 °C, while Au(SMePh) exhibits a weak red emission at room temperature because of the minor electronic transition induced by the ligand (Figure 38). The emission increases with decreasing temperature owing to the enhanced structural rigidity and faster intersystem crossing process. At −180 °C, Au(SPh) glass exhibits red phosphorescence (microsecond lifetime) with a maximum emission peak at 690 nm and Stokes shift of −9780 cm^{-1}, which deviates from the 675 nm emission peak with Stokes shift of 16435 cm^{-1} of the crystalline state. In contrast, Au(SMePh) and phenylethanethiolate Au(SEtPh) glasses exhibit an emission peak at 675 nm with a Stokes shift of >12000 cm^{-1}.

7.2.2. Nonlinear Optics. The near-infrared nonlinear optical (NIR-NLO) responses to a femtosecond laser was

A

B
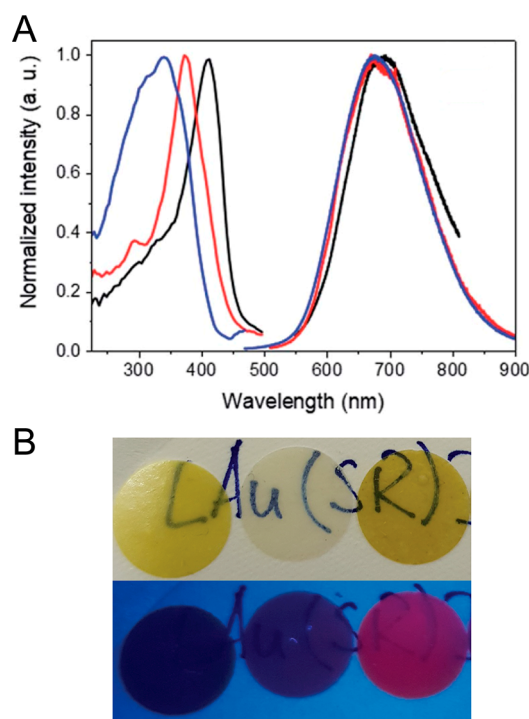
Figure 38. (A) Emission−excitation spectra of Au(SPh) (black), Au(SEtPh) (blue), and Au(SMePh) (red) obtained in the solid state at −180 °C with, respectively, ($λ_{ex}$, $λ_{em}$) in nm as follows: (412, 690), (372, 675), and (340, 675). (B) Photos of Au(SPh), Au(SEtPh), and Au(SMePh) glass pellets (from left to right). Photos are shown under normal (top) and UV (bottom) lighting. Reprinted with permission from ref 34. Copyright 2020 The Royal Society of Chemistry. https://creativecommons.org/licenses/by/3.0/.

observed in an identical series of $Zn_{1−x}Co_x(Im)_{1.7}(bIm)_{0.3}$ MQGs (Figure 39).[35] An NLO response is one that deviates from a linear response; it typically occurs at high powers. Unlike the $Zn(Im)_{1.7}(bIm)_{0.3}$ MQG, where no NLO response is observed because of its high transparency in the NIR range, the $Zn_{0.5}Co_{0.5}(Im)_{1.7}(bIm)_{0.3}$ MQG exhibits two strong absorption bands at 570 and 1100 nm. These prerequisite absorption peaks are assigned to the d−d transitions of
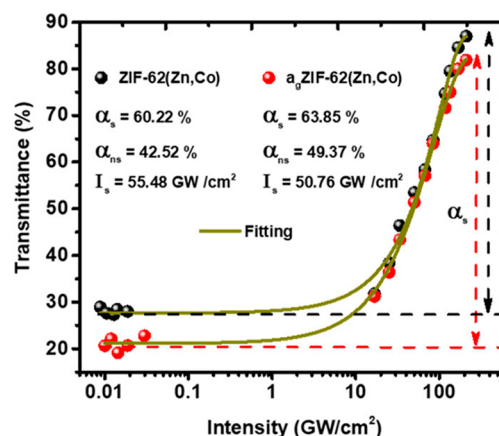
Figure 39. Dependence of transmittance on the laser power density for ZIF-62-Zn/Co and ZIF-62-Zn/Co MQGs. $α_s$, $α_{ns}$, and I_s are saturable loss, nonsaturable loss, and saturation intensity, respectively. Reprinted with permission from ref 35. Copyright 2020 American Chemical Society.

tetrahedrally coordinated Co^{2+} via $^4A_2(^4F) \rightarrow {}^4T_1(^4F)$ and $^4A_2(^4F) \rightarrow {}^4T_1(^4P)$. A saturable broad positive peak at the beam focus was observed in both crystalline and glassy $Zn_{0.5}Co_{0.5}(Im)_{1.7}(bIm)_{0.3}$ under an open-aperture Z-scan measurement with a 1030 nm femtosecond laser (260 fs, 1 kHz), indicating the presence of an NLO response. The crystal−glass transformation induces changes in NLO parameters, such as the saturable loss (α_s), imaginary part of $\chi^{(3)}$, absorption coefficient (β), and figure of merit (FOM), from 60.22%, -5.93×10^{-11} esu, -3.37 cm GW^{-1}, and 26.94×10^{-11} esu cm for the crystalline state to 63.85%, -3.55×10^{-11} esu, -2.02 cm GW^{-1}, and 10.75×10^{-11} esu cm for the glassy state, respectively. The modulation depths in $Zn_{0.5}Co_{0.5}(Im)_{1.7}(bIm)_{0.3}$ glass at 1030 nm are higher than those observed in low-dimensional NLO materials, including plasmonic nanostructures, graphene, and molybdenum disulfide.[191]

7.3. Mechanical Properties

The intrinsic mechanical properties dictate the potential applications of these novel CP/MOF glasses. By understanding the nature of CP/MOF glasses, the mechanical reliability during operation can be predicted. We differentiate studies into stiffness and failure mode. The former term identifies the deformation resistance in response to applied force, while the latter discusses the conditions in which glass fails under the action of external loads.

7.3.1. Stiffness.
Nanoindentation studies of ZIF glasses revealed that their elastic modulus correlates well with the pycnometric density and chemical composition.[101] The indentation modulus of ZIF-62 glass was calculated to be ∼6 GPa with a Poisson's ratio of 0.45 via Brillouin scattering.[94] The scratch resistance and creep behavior of ZIF-4, ZIF-62, ZIF-76, and ZIF-76-mbIm glasses have been studied by nanoindentation.[105] The strain-rate sensitivities determined through both strain-rate jump (SRJ) and constant load and hold (CLH) indentation creep experiments were comparable to the reported values for glassy polymers and Se-rich GeSe chalcogenide glasses with similar hardness. The absence of a jump in the friction coefficient curve of ZIF-62 glass after remelting indicates the absence of ductile fracture.

In contrast to conventional materials with a high Poisson's ratio, ZIF glasses exhibit easy crack nucleation. Micro- and nanoindentation were conducted on a large ZIF-62 glass monolith to further understand the anomalous behaviors through the deformation and crack initiation patterns.[106,192] The Vickers microhardness dropped drastically from 0.65 to 0.53 GPa as the load increased from 0.1 to 0.2 N. The rate of decrease became more gradual from 0.53 to 0.50 GPa for higher indentation loads (Figure 40A). The uncommon drop in hardness from the initial state is due to the drastic free volume change because the Zn−N coordination bonds break more easily than metallic, covalent, and ionic bonds. The gradual change at higher loads is ascribed to the indentation size effect, where the ratio between the indentation surface and the deformation volume increases with decreasing load owing to the elastic contribution.

7.3.2. Failure Mode.
Crack initiation and deformation mechanisms were studied via the subsurface area cross-sectional view of the indentation (Figure 40B).[106] Microcracks originated from the deformation and densification in Zone 1 (process zone), while median (B) and radial (C) cracks initiated in Zone II. Zone III refers to the undeformed glass
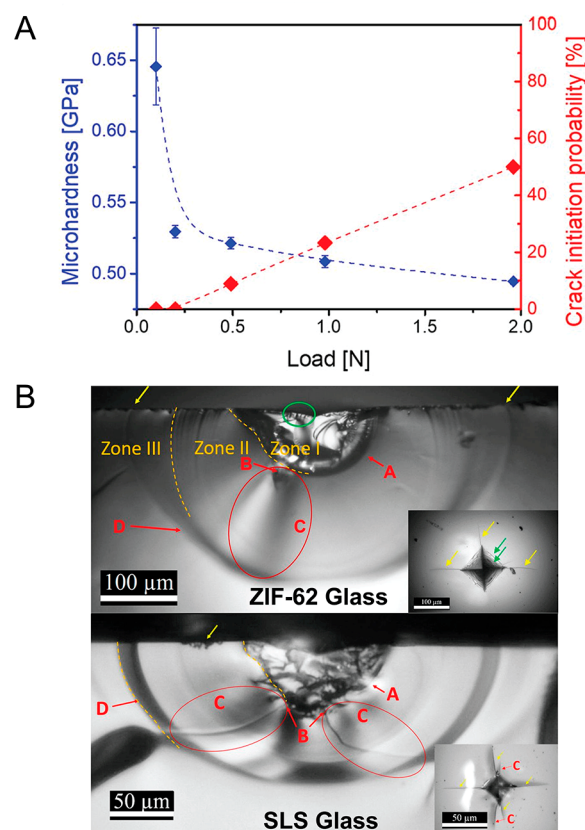
Figure 40. (A) Indentation behavior and Vickers microhardness of ZIF-62 glass in the load range 0.1−1.96 N. (B) Indentation deformation zone for ZIF-62 glass and soda−lime−silica (SLS) window glass. The inset displays radial cracks (yellow), median cracks (red) and shear bands (green). Reproduced with permission from ref 106. Copyright 2020 U.S. National Academy of Sciences.

matrix. These three zones are identical to those observed in most silica glass. The presence of a median crack in ZIF glasses is considered abnormal because of their considerably higher Poisson's ratio (0.45 and 0.35 via Brillouin scattering and sound wave velocity measurements, respectively). This could be attributed to sinking-in deformation from the weaker coordination bonds. Additionally, translational motion and bond reorientation enable the formation of anomalous shear bands, which have not been found in any fully polymerized 3D network glasses.

The fracture toughness (K_{Ic}), flexural strength, and origin of the fracture behavior of ZIF-62 glass, $Zn(Im)_{1.75}(bIm)_{0.25}$, were studied using the single-edge precracked beam (SEPB) method and ReaxFF-based MD simulations.[113] ZIF-62 exhibits a large degree of nanoductility under load, in contrast to the very brittle nature of a-SiO_2 glass. The brittleness index (B_{index}) of ZIF-62 glass is 0.70, where $B_{index} = 1$ corresponds to an ideal brittle material. It is worth noting that the value falls between that of disordered calcium silicate hydrate gel (0.62) and a-SiO_2 glass (0.9). The atomic-scale crack propagation mechanism was investigated to understand the origin of the fracture behavior. First, the introduced precrack induces the stretching of bonds with small strain values (Figure 41A). Increasing the strain then initiates actual bond breaking with crack propagation and the formation of nanocavities. Nano-ductility was found to originate from the formation of molecular bridges across the two fracture surfaces (Figure
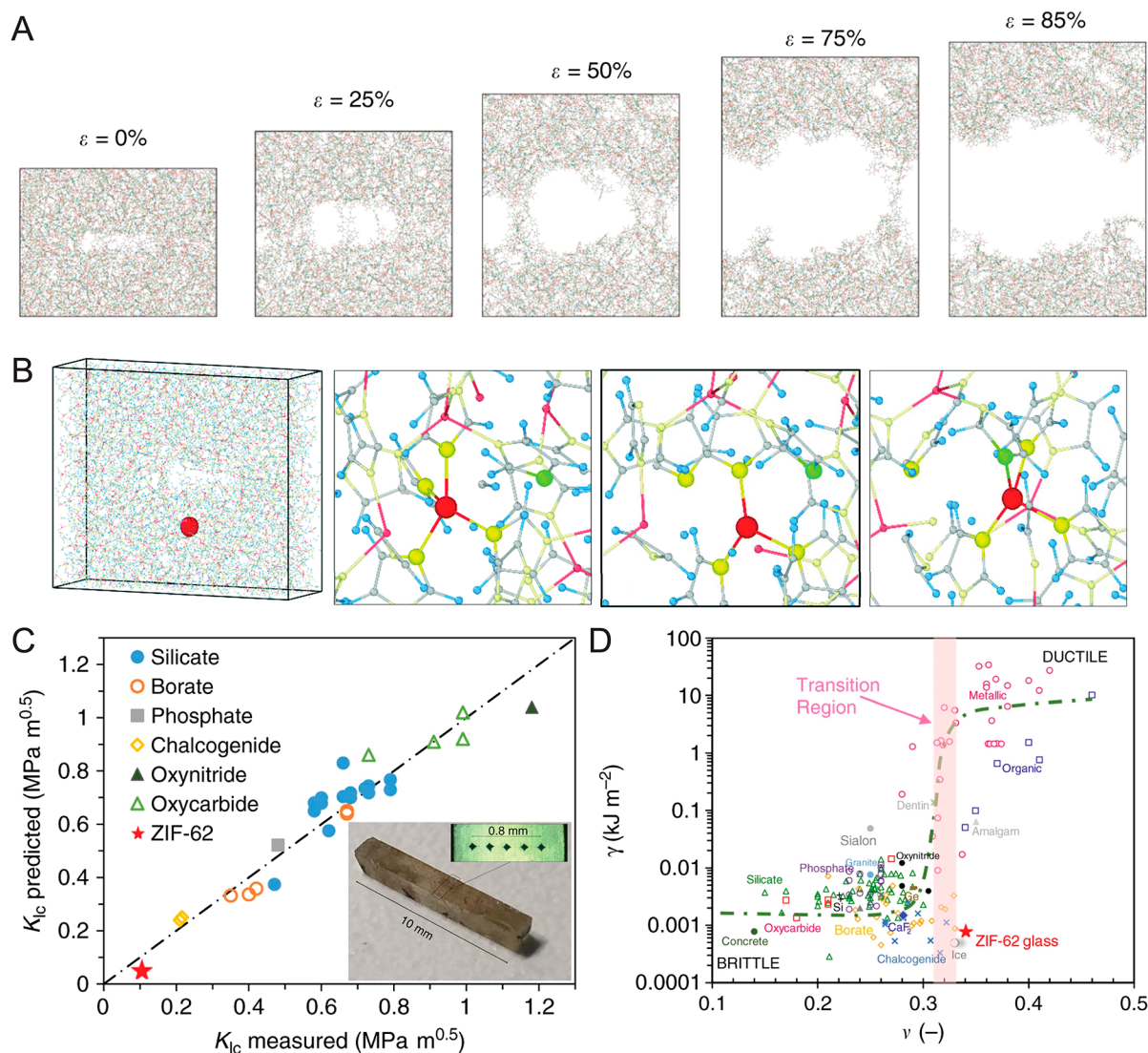
Figure 41. (A) Structural representation of crack propagation with increasing strain (ε) in a precracked ZIF-62 glass. The colored spheres represent carbon (red), hydrogen (gray), nitrogen (green), and zinc (blue). (B) Bond switching event during fracture. The color spheres depict carbon (gray), nitrogen (yellow and green), hydrogen (blue), and zinc (red). Position of the considered Zn atom (enlarged for visualization). Zn is 4-fold coordinated at $\varepsilon = 0$ and 3-fold coordinated at $\varepsilon = 0.09$. Zn returns to a 4-fold coordinated state at $\varepsilon = 0.42$, but with a new organic linker. (C) Predicted versus measured fracture toughness (K_{Ic}) for a range of different glass families. (D) Relationship between fracture surface energy (γ) and Poisson's ratio (ν) for a range of glass materials, showing an apparent brittle-to-ductile transition. Adapted with permission from ref 113. Copyright 2020 Springer Nature Limited under Creative Commons license CC BY 4.0. https://creativecommons.org/licenses/by/4.0/. Reprinted with permission from ref 88. Copyright 2021 The Royal Society of Chemistry.

41B), while the low fracture toughness was found to originate from the weak Zn−N coordination bonds. Interestingly, the applied stress induces rearrangement of the structure and ultimately increases the connectivity of the network. Thus, the total number of bonds after full fracture was observed to be higher than that before forced deformation. Nanoductility was later attributed to the Zn−N bond switching mechanism.[88] The behavior was found to be more pronounced for smaller organic linkers, resulting in slightly different fracture behaviors for various ZIF glasses, including ZIF-4, ZIF-62, and ZIF-76.

The fracture toughness of ZIF glasses was predicted using a model developed for oxide glasses that employs the bond strength and bond concentration along the fracture surface as well as the experimental values (Figure 41C).[113,193] Although the K_{Ic} of ZIF-62 glass is between that of elastomers and foams, its Young's modulus ($E = 4–6$ GPa) is considerably larger than

that of either material ($E < 1$ GPa). Additionally, the Poisson's ratio ($\nu = 0.34–0.35$) is as high as that of many metallic and organic glasses, allowing ZIF-62 to exhibit an anomalous position in the brittle-to-ductile transition curve (Figure 41D).

7.4. Porosity and Gas Permeability

7.4.1. Porosity. One characteristic functionality of crystalline CPs/MOFs is their permanent porosity. However, the retention of accessible porosity in CP/MOF glasses is challenging because the pore cavities generally collapse into a dense amorphous phase upon thermal or mechanical glass transformation. Thus, far, only partial retention of porosity in MOF glasses has been observed. Investigation of internal porosity in MQGs began with the PALS characterization of ZIF-4.[89] The results indicated that the MQG exhibits an intermediate porosity between that of crystalline ZIF-4 and dense ZIF-zni with a wider pore size distribution. It is worth

noting that neither the MQG nor ZIF-zni displayed significant N_2 uptake. Liquid ZIF-4 retains a substantial quantity of cavities according to computational modeling.[61] The statistical analyses of the instantaneous porosity evolution with increasing temperature were studied with a probe diameter of 2.4 Å (kinetic diameter of He). Pore distribution broadening was observed with increasing thermal motion (Figure 42). At
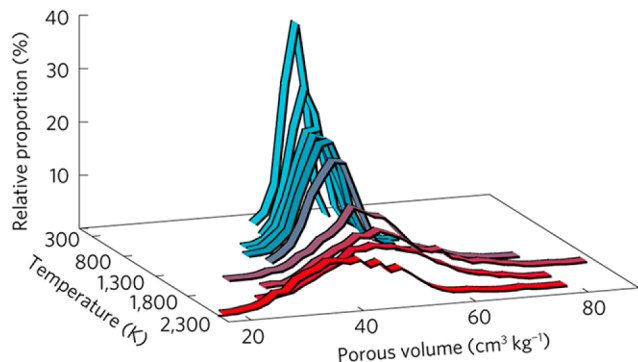
Figure 42. Distribution of total pore volume in ZIF-4 with increasing temperature calculated by FPMD. Reprinted with permission from ref 61. Copyright 2017 Springer Nature.

T_m, the partial preservation of porosity was observed with a slight deviation toward a lower pore volume with a larger accessible fraction from 74% in crystalline ZIF-4 at 27 °C to 95% in liquid ZIF-4 at 1227 °C.

Permanent porosity in CP/MOF glasses has been studied experimentally in ZIF-76 and ZIF-76-mbIm MQGs.[102] PALS revealed the contraction of pore cavities, where the cavities in ZIF-76 glass were reduced to a single cavity with a diameter of ~5 Å. In contrast, ZIF-76-mbIm retained two distinct pore characteristics, featuring contracted pores with diameters of 5.8 and 15.6 Å. Gas adsorption measurements of the ZIF-76 glass revealed a low uptake of N_2 and H_2 at 77 K with a significant hysteresis due to the restricted diffusion of guest molecules. In contrast, the ZIF-76-mbIm glass exhibited reversible CO_2 and CH_4 adsorption at 0 and 20 °C. However, pore contraction upon vitrification reduced the CO_2 uptake, with an estimated pore volume of 0.12 mL g^{-1} (7 wt % uptake) compared to 0.17 mL g^{-1} (10 wt % uptake) for its crystalline precursor (Figure 43). Kinetic analysis suggested that CO_2 diffusion was more constricted in the glass, and the pore network was more tortuous. Partial retention of porosity was observed in a glass prepared from the Co^{2+} analog of ZIF-62.[114] The MQG exhibited 50% of the CO_2 uptake (0.75 mmol g^{-1}) of its crystalline state at −178 °C. Moreover, the preserved cavities in ZIF glasses can host electrolytes and could be beneficial for electrochemical energy systems.[187,194]

In addition to ZIF glasses, permanent porosity for gas and vapor sorption has been demonstrated in [Ag(mL1)-(CF$_3$SO$_3$)]·2C$_6$H$_6$ and [Ag(pL2)(CF$_3$SO$_3$)]·2C$_6$H$_6$ (Figure 19).[92,93] The glasses prepared by mechanical vitrification exhibited microporosity characterized by CO_2 adsorption uptakes of 18 and 9.2 mL g^{-1}, respectively. A gate-opening type of adsorption behavior was observed in both MIGs. The vapor uptake was exclusive to glass phases; no uptake was observed for crystalline phases in the pressure range of 0−12.3 kPa. Unlike during gas uptake, in which the glassy state remained stable, both MIGs underwent a glass-to-crystal
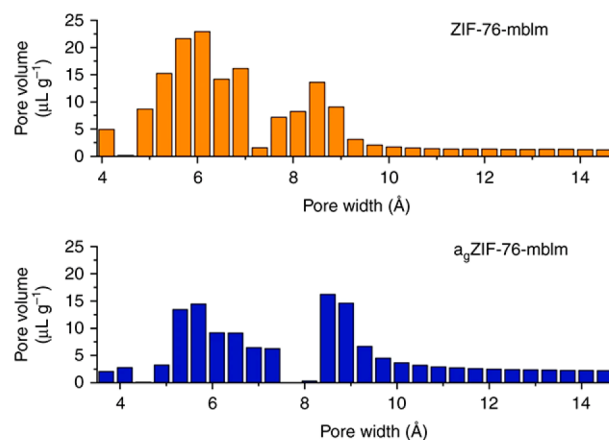
Figure 43. Pore size distributions of crystalline and MQG ZIF-76-mbIm determined by the NLDFT method from CO_2 adsorption isotherms at 0 °C. Reprinted with permission from ref 102. Copyright 2018 Springer Nature Limited under Creative Commons license CC BY 4.0. https://creativecommons.org/licenses/by/4.0/.

transformation during vapor uptake, suggesting a vapor-induced crystallization behavior in these glasses.

The coexistence of guest-accessible porosity and H$^+$ conductivity has been observed in meltable [Zn$_2$(HPO$_4$)$_2$(H$_2$PO$_4$)] (ClbImH$^+$)$_2$(H$_2$PO$_4$$^-$)(MeOH) (Figure 4).[125] The as-synthesized 2D framework contains three types of uncoordinated guest molecules: protonated ClbIm, methanol, and H$_2$PO$_4$$^-$. Activation at 120 °C under vacuum resulted in accessible porosity through the release of encapsulated methanol, equivalent to 3.6 wt %. As demonstrated by the water and methanol isotherms, the guest-accessible porosity was maintained in the MQG. Gradual uptakes at 25 °C with a continuous structural change suggest a gate-opening effect. Interestingly, the maximum water and methanol uptakes of the MQG of 118.0 and 61.5 mL g^{-1} are slightly higher than the 111.9 and 35.0 mL g^{-1} of the crystalline counterpart. It is worth mentioning that both the crystalline and glassy states selectively adsorbed water and methanol but were not observed to uptake gases such as N_2 and CO_2. Moreover, the presence of guest water enhanced the H$^+$ conductivity of the MQG, where the conductivity increased to 1.2×10^{-4} S cm^{-1} at 25 °C and 98% RH compared to $<10^{-7}$ S cm^{-1} under anhydrous conditions.

Selective hydrocarbon sorption was demonstrated with the ZIF-62-bIm$_x$ glass variant containing a Zn^{2+} metal node (x = 0.05, 0.17, 0.35). Identical to the Co^{2+} analog, ZIF-62-bIm$_x$ exhibited a permanent porosity with 50% of the CO_2 uptake of its crystalline state at 0 °C. The pore size distribution indicates the loss of small cavities (diameter $\approx$ 3.5 Å), the retention of medium-sized cavities (diameter $\approx$5−6 Å), and the emergence of large cavities (diameter $\approx$ 8 Å).[116] In contrast to CO_2, a large hysteresis was observed in the sorption isotherms of n-butane (kinetic diameter of 4.3 Å), with uptake of 0.7 to 0.8 mmol g^{-1} at 0 °C. Additionally, the hysteresis became more pronounced with the increasing Im/bIm ratio because the bulkier bIm restricted the diffusion kinetics of the larger hydrocarbon gas. Kinetic sorption measurements revealed a preference for the adsorption of propylene over propane, where the diffusion rate could be controlled via the Im/bIm ratio (Figure 44). The propylene/propane selectivity based on the ideal adsorption solution theory (S_{IAST}) is between 1.8 and 2.5 for a 1:1 mixture. Although the current benchmark MOFs
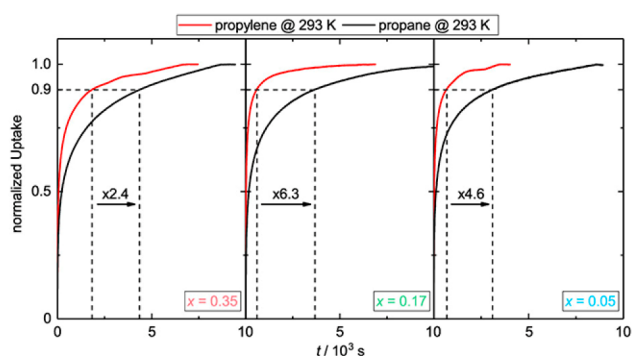
Figure 44. Kinetic sorption profiles of ZIF-62-bIm$_x$ glass (x = 0.05, 0.17, 0.35) recorded with an equilibrium pressure of ~54 kPa. Reprinted with permission from ref 116. Copyright 2019 American Chemical Society.

exhibit a considerably larger propylene/propane selectivity (S_{IAST} of up to ~60), the ability to form a grain-boundary-free monolith opens opportunities for the fabrication of homogeneous membranes[28,29] and mixed-matrix monoliths.[38,180]

7.4.2. Gas Permeability. Membrane-based separation plays a critical role in purification and separation technologies. The polycrystalline nature of the zeolitic and MOF membranes suffers from unavoidable grain boundaries or cracks. CP/MOF glasses possess the ability to be processed through the solid–liquid transition while maintaining their porous nature, resulting in a promising system for grain-boundary-free membrane. The preparation of glass membranes for gas separation has been demonstrated with both ZIFs and phosphate–azole frameworks.[28,29] A ZIF-62-based glass membrane was prepared by melt-quenching treatment of an in situ solvothermally synthesized polycrystalline ZIF-62 on a porous ceramic alumina support (Figure 45A).[28] The vitrified membrane demonstrated a highly isotropic and grain-boundary-free nature, which is in contrast to the polycrystalline precursor. Additionally, parts of the melts penetrated the top layer of Al$_2$O$_3$, improving the stability of the membrane interface. The elimination of interparticle gas diffusion enhanced the molecular sieving ability of the membrane for H$_2$/CH$_4$, CO$_2$/N$_2$, and CO$_2$/CH$_4$, with separation factors of 50.7, 34.5, and 36.6, respectively (Figure 45B). Moldability through the reversible solid-to-melt transformation in [M-(H$_2$PO$_4$)$_2$(HPO$_4$)]·(H$_2$dmbIm)$_2$ (M = Zn^{2+}, Cd^{2+}, Cu^{2+}, and Mn^{2+}) (Figure 4) enables the preparation of a healable membrane.[29] The low viscosity of [M(H$_2$PO$_4$)$_2$(HPO$_4$)]·(H$_2$dmbIm)$_2$ permits the application of hot-casting or hot-pressing techniques to prepare a variety of membranes, either free-standing or porous matrix composites (Figure 45C and D). The derived glass membrane exhibited H$_2$/CO$_2$, H$_2$/N$_2$, and H$_2$/CH$_4$ separation capabilities (Figure 45E). The membrane showed healing ability via melt-quenching, with complete separation performance recovery.

7.5. Thermal Conductivity

The relationship between the densification of ZIFs upon glass formation and their thermal conductivity (κ) has been studied.[111] Conventionally, the thermal conductivity of glasses is always lower than that of the corresponding crystal because they possess weaker phonon–phonon scattering. The weaker scattering is due to the increase in the free volume upon vitrification. However, both ZIF-4 and ZIF-62 display anomalous behavior: the glassy states of both compounds
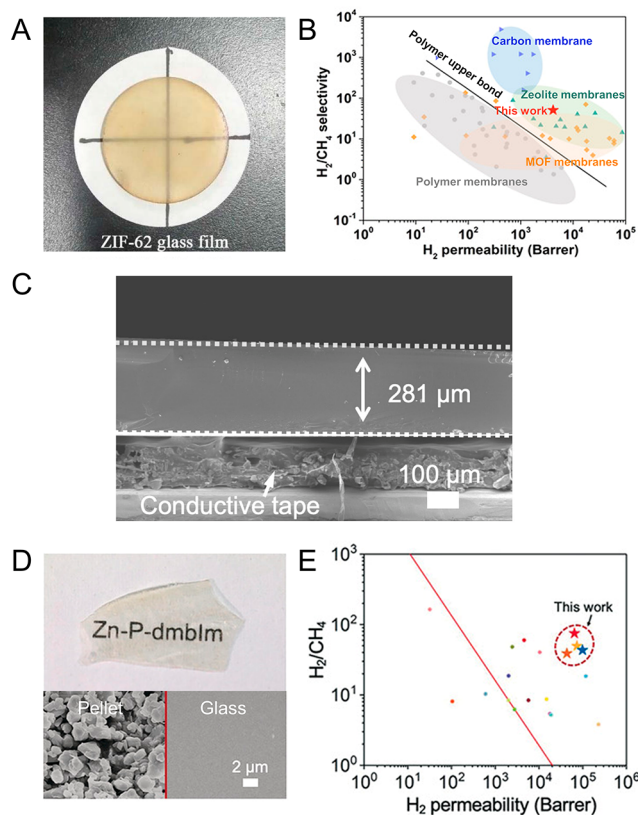
Figure 45. (A) Photograph of a ZIF-62 glass film on a nonporous SiO$_2$ support with a diameter of 5 cm. (B) Comparison of the separation performances of the glass membrane for H$_2$/CH$_4$. Adapted with permission from ref 28. Copyright 2020 John Wiley and Sons. (C) Cross-sectional SEM, as well as (D) a photograph of a free-standing [Zn(H$_2$PO$_4$)$_2$(HPO$_4$)]·(H$_2$dmbIm)$_2$ glass membrane and SEM images of the pellet and glass membrane. (E) Comparison of the separation performances of the glass membrane for H$_2$/CH$_4$. Circles represent the separation performances of reported MOF membranes. Reprinted with permission from ref 29. Copyright 2021 John Wiley and Sons.

have a higher thermal conductivity with negative $\Delta\kappa$ values (Figure 46). Because the crystal and glass share an identical heat transfer mechanism, as revealed by ReaxFF-based MD simulations, the difference in κ is ascribed to the higher density and rigidity of the ligand. Both are caused by the collapse and distortion of internal cavities upon melting.

8. OUTLOOK AND CONCLUSION

For decades, research on CPs/MOFs has mainly focused on crystalline systems. With the increasing realization that intrinsic disorder can enable unique features in materials, recent years have witnessed the emergence of diverse interests in noncrystalline CP/MOF glasses, which possess a fully disordered system. Moldability through a mechanically "soft" nature or the presence of a reversible solid–melt transition in CP/MOF glasses enables the fabrication of grain-boundary-free monoliths. Enhanced ion (H$^+$/Li$^+$) conductivities in CP glasses have been implemented in all-solid-state fuel cells and secondary batteries.[30−32,187] Distinct mechanical and thermal behaviors have been observed.[88,106,111,113] The gas separation ability of melt-quenched membranes has benefited from the elimination of interparticle space, pore-size restriction, and ease of processing.[28,29,116] Transparent, luminescent, and
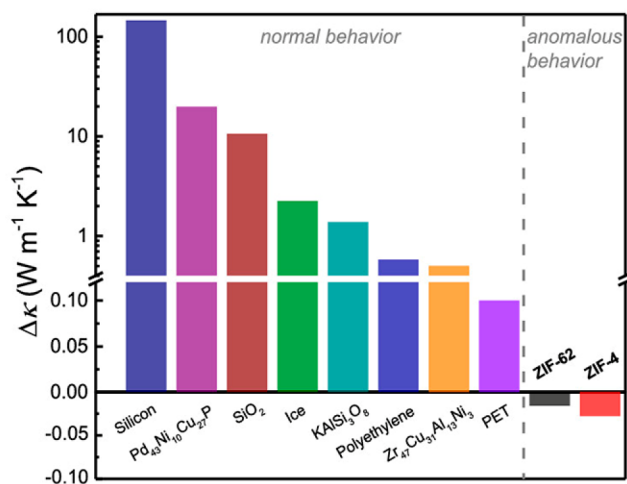
Figure 46. Difference in thermal conductivity (κ) between the amorphous and crystalline states ($\Delta\kappa = \kappa_{crystal} - \kappa_{amorphous}$) for ten different materials, including ZIF-4 and ZIF-62, obtained from room temperature powder pellet measurements. Reprinted with permission from ref 111. Copyright 2020 American Chemical Society.

nonlinear optics have been demonstrated.[34,35,112] The absence of stoichiometric constraints, controllable phase transitions, and microstructuring highlights the opportunity for tailored functionalities in CP/MOF liquids and glasses. In their infancy, the aforementioned features have undoubtedly attracted interest in the discovery of novel structures and functionalities. However, substantial challenges remain, including the fundamental aspects of controlling, characterizing, and exploiting the liquid and glassy states.

8.1. Crystal Melting and Glass Formation

The variation of specific framework components within crystalline CPs/MOFs can be exploited to render distinct thermal behaviors. To achieve a stable liquid state, the intrinsic T_m must be lower than the T_d. Reducing T_m or increasing T_d while retaining the counterpart is essential. Thus, far, the manipulation of T_m is plausible by balancing the entropy and enthalpy changes upon melting ($T_m = \Delta H_{fus}/\Delta S_{fus}$). To some extent, this relationship has already been utilized empirically to correlate the change at the molecular level to the melting behavior.[41,115,116] ΔH_{fus} can be minimized by regulating the cohesive interactions between the solid and melt states. A certain degree of decoordination must be allowed during melting.[54,61] A lower crystal field stabilization energy, particularly for the d^{10} configuration, requires a lower energy for bond dissociation.[54,91] The hard−soft acid−base theory is another practical guideline for estimating the strength of metal−ligand interactions. Melts are stabilized through the minimization of electrostatic attractions via charge delocalization and spatial separation of anions and cations, mimicking the anticrystal engineering of ionic liquids. In contrast, ΔS_{fus} must be maximized, which is achievable by restricting the residual motion in solids through intermolecular interactions and promoting a higher degree of freedom in the liquid state through flexible ligands and labile coordination nodes. In addition, the presence of porosity hinders the observation of T_m because the free space allows the ligands to possess a higher degree of residual motion and thus increases the overall entropy in the solid state. However, the manipulation of thermal behavior and the kinetics of the quenching process still

require further understanding. For example, can T_g be manipulated without disturbing T_m? How can the glass-forming ability of melts be modulated in cases where cooling the melt yields a crystallized product instead of vitrified glass?[30,41,195−198] The absence of stoichiometric constraints in the glass opens the possibility of modulating thermal behavior through doping, which has proven effective in conventional glasses.

Preparation of stable melts and large-scale production of monoliths have always been challenging. Although ZIF-62 glass can be obtained by melt-quenching in the Ar atmosphere, it suffers from oxidation at high temperatures. It has difficulty preparing a bubble-free glass sample due to its high viscosity.[112] A vacuum hot press with polishing is required to obtain a transparent, bubble-free monolith. In comparison to viscous ZIF-62 melts ($10^{5.1}$ Pa s at T_m), [Zn(HPO$_4$)-(H$_2$PO$_4$)$_2$](ImH$_2$)$_2$ ($10^{0.6}$ Pa s at T_m)[26] and [Zn$_3$(H$_2$PO$_4$)$_6$(H$_2$O)$_3$](BTA) ($10^{2.3}$ Pa s at T_m)[32] are more easily formed into glass monoliths/films of the appropriate size. The behavior is primarily correlated with two parameters: viscosity above T_m and temperature windows between T_m and T_d. The viscosity of melts is the most important parameter during the glass-forming process.[199] A suitable range of viscosity depends on the glass-forming technology used. The main characteristic temperatures are assigned based on the viscosity: (1) Melting point (10^1 Pa s). this temperature does not correspond to the physical melting point, but it is the temperature at which the viscosity is suitable for the melt to provide good homogeneity within the melting container. (2) Working point (10^3 Pa s) is the temperature at which most forming processes occur. However, the viscosity varies based on the forming technology. (3) Softening point ($10^{6.65}$ Pa s) or Littleton softening point is the temperature at which glass deforms under its own weight at the rate of 1 mm/min. After the forming process, the glass must be released at a temperature below this point to avoid unwanted deformation. (4) Strain point ($10^{13.5}$ Pa s) is the temperature at which the stresses generated during the forming process can be released within 15 h. (5) At the annealing point ($10^{11.4}$ Pa s), glass can release the stresses generated during forming by viscous relaxation within 15 min. The annealing process includes heating above the annealing point, followed by slow cooling. In addition, a wider stable liquid state temperature window allows a higher possibility of achieving a suitable viscosity for glass fabrication.

Thus, far, the discovery of melting quenching and mechanically induced vitrification has been primarily achieved based on scientific intuition and trial-and-error experimentation. This results in a lengthy time to discover new CPs/MOFs that can undergo vitrification, delaying the exploration of new functionality. An important question here is how can we discover/design a potential glass-forming CP/MOF with the desired properties? Screening through computational means potentially provides some hints prior to the actual experiment. High-throughput theoretical calculations offer the opportunity to efficiently search for new systems with accessible melting behaviors through the evaluation of thermodynamic parameters.[200]

8.2. Alternative Routes to Obtain a Glassy State

CP/MOF glasses can be fabricated through alternative routes, such as mechanical vitrification and direct synthesis. Because most CPs/MOFs undergo thermal decomposition upon

heating prior to melting, these approaches are positioned as alternative pathways to access the glassy state. Furthermore, only minor differences are present between glasses obtained from different routes. Mechanical methods are considered a greener process compared to the energy-intensive melting process.[80] However, these glasses are underexplored because only five MIG compounds and three families of direct synthesis glasses have been explored.[31,34,81,91–93,117,173–175]

At the present stage, the intrinsic elastic, bulk, Young's, and shear moduli of the framework are found to rely on the strength of coordination bonds and can be optimized through the variation of the framework components.[91] Higher mechanical stability requires a substantial amount of energy for complete vitrification. Generally, MIGs exhibit thermally induced crystallization. The process, which relies on the growth of residual nuclei, is an exclusive feature of MIGs and inaccessible in most MQGs because none of the starting nuclei survive the melting process.[150] The underlying challenges are the limited number of examples and characterization difficulties. Computational studies and in situ monitoring are more complex because each degree of freedom in the milling or direct synthesis process must be considered, while for MQGs, only the thermal stimuli need to be considered. At the most basic level, systematic correlations between the mechanical properties of the crystalline parent and their behaviors under mechanical stress can provide a mechanistic understanding and general strategies to achieve MIGs.

Vitrification through alternative approaches such as light irradiation potentially offers an opportunity to precisely control the vitrification in a confined space. Moreover, reversible crystal–glass transformation is potentially controlled by incorporating two or more light-responsive components into the CPs/MOFs and responding to different wavelengths of light. Although the method has not yet been demonstrated to provide glassy behaviors in CPs/MOFs, examples can be found in amorphous CPs/MOFs. They undergo amorphization under prolonged light irradiation or even exposure to electron beams, X-rays, and γ rays.[176,201–203] Care must be taken to distinguish the contributions of irradiation and heat to the vitrification process as well as identify the amorphous products, whether they are glasses or decomposed residuals. Although glass vitrified through conventional melt-quenching and irradiation are expected to share some degree of similarity, unique features are expected in irradiation-induced glasses due to the potential difference in short and medium-range structure. An example is silica glass, where irradiated quartz comprises coordination defects, edge-sharing units, and large silicate rings, which are absent from the structure of melt-quenched silica.[204]

8.3. Structural Identification

Understanding the nature of liquids and glasses is unarguably one of the most complex problems in science.[205] To begin with, distinctions in topology and chemical composition already lead to different melting mechanisms, where the melts exhibit either complete dissociation into 0D fragments or only partial decoordination with rearrangement of ligands.[54,61] As previously mentioned, the nucleation process of melts is an exclusive feature observed in very few CPs/MOFs.[26,30,41,195–198] Understanding the nucleation processes is a huge challenge, even in conventional crystal growth.[206,207] Recrystallization from supercooled liquids or melts would provide a facile fabrication method for thin films, the alignment

of crystal orientation, and the growth of single-crystal monoliths. Another challenge is the difficulty in structural identification. The amorphous nature of liquids and glasses limits structural characterization to local distribution and computational modeling.[31,55,61,208] The development of accurate modeling for representative liquid and glass structures is crucial to correlate the macroscopic properties with local topology, kinetic factors governing ligand reorientation in the liquid state, and the degree of structural periodicity of the network under various vitrification conditions.[83,209–211]

8.4. Application

As described previously, the unique network topologies of CPs/MOFs in the liquid and glassy states provide exceptional ion, phonon, and mass transport. To perceive and exploit the advantages of the phase transition in CPs/MOFs, established examples in conventional systems should be considered, including organic polymers, ceramics, metals, and molecular glasses. Aspects that differentiate CP/MOF glasses from traditional glasses include the labile nature of coordination bonds, compositional variation through reticular design, manipulation of network connectivity through coordination chemistry, and functionality controlled at the molecular level. Exploiting the extensive library of metal ions, secondary building units, and organic linkers available for the construction of crystalline CPs/MOFs and reinterpreting this from the anti-crystal engineering perspective would enable the precise control of properties in glasses and liquids as well as extend the functionality to a wider range of applications. Moldability through a softer nature or reversible phase transitions enables the fabrication of various conformations. Microstructuring and the formation of complex hierarchical domains can give rise to unique chemical and physical properties, such as interfacial conductivity or unidirectional ion transport. Hybridization with other materials is also feasible. The reversible crystal–liquid–glass transformation is promising for the fabrication of immersive interfaces and beneficial for electrochemical applications, where the electrode/electrolyte interface contributes significantly to performance. Grain-boundary-free monoliths lead to the fabrication of homogeneous films or membranes, which are ideal for applications such as charge transport, photonics, and gas separation. Thermal/light-induced phase transitions are promising for thermal/solar energy storage and conversion or even phase-transition memory units. The inclusion of stimuli-responsive dopants in a glass matrix could result in an advanced functional glass with switching capabilities or luminescence. Finally, it remains challenging to establish a connection between the physical properties, local topology, and the underlying chemistry of glasses. The collective understanding of and the ability to exploit the liquid and glassy states of CPs/MOFs at an early stage of the transition toward disorder can enable more applications in the future.

ASSOCIATED CONTENT

Special Issue Paper

This paper is an additional review for *Chem. Rev.* 2020, volume *120*, issue 16, "Porous Framework Chemistry".

AUTHOR INFORMATION

Corresponding Author

Satoshi Horike − *Department of Synthetic Chemistry and Biological Chemistry, Graduate School of Engineering, Kyoto*

University, Kyoto 615-8510, Japan; AIST-Kyoto University Chemical Energy Materials Open Innovation Laboratory (ChEM-OIL), National Institute of Advanced Industrial Science and Technology (AIST), Kyoto 606-8501, Japan; Institute for Integrated Cell-Material Sciences, Institute for Advanced Study, Kyoto University, Kyoto 606-8501, Japan; Department of Materials Science and Engineering, School of Molecular Science and Engineering, Vidyasirimedhi Institute of Science and Technology, Rayong 21210, Thailand; orcid.org/0000-0001-8530-6364; Email: horike@icems.kyoto-u.ac.jp

Author

Nattapol Ma − Department of Synthetic Chemistry and Biological Chemistry, Graduate School of Engineering, Kyoto University, Kyoto 615-8510, Japan; orcid.org/0000-0002-6162-1834

Complete contact information is available at:
https://pubs.acs.org/10.1021/acs.chemrev.1c00826

Notes

The authors declare no competing financial interest.

Biographies

Nattapol Ma is a Ph.D. student and a Japanese Government (MEXT) scholarship fellow in Horike's group at Kyoto University. His current research focuses on charge transport in coordination polymer and metal−organic framework glasses. He received his M.Eng. and B.Eng. in chemical engineering from Vidyasirimedhi Institute of Science and Technology (VISTEC) and King Mongkut's Institute of Technology Ladkrabang (KMITL).

Satoshi Horike received his Ph.D. in 2007 at the Graduate School of Engineering, Kyoto University. He carried out postdoctoral research at the University of California, Berkeley, for two years. In 2009, he began work at Kyoto University, Graduate School of Engineering, as an Assistant Professor. Since 2017, he has been working as an Associate Professor at the Institute for Advanced Study, Kyoto University. His research is based on coordination chemistry and solid-state chemistry, particularly the synthesis of ion conductors and molecular framework-based glass materials showing phase transition.

ABBREVIATIONS

0D	discrete molecule
1D	one-dimension
1-mIm	1-methylimidazole
2D	two-dimension
2-Mebim	2-methylbenzimidazole
3D	three-dimension
3-Pybpy	[3,1′:4′,4″-terpyridin]-1′-ium
5-Cl-2-mbIm	5-chloro-2-methylbenzimi-dazolate
5-ClbIm	5-chloro-benzimidazolate
5-FbIm	5-fluoro-benzimidazolate
6-Cl-5-FbIm	6-chloro-5-fluoro-benzimidazolate
AFM	atomic force microscopy
bba	N,N'-1,4-butylenebis(acetamide)
BDC	1,4-benzenedicarboxylate
BET	Brunauer−Emmett−Teller
bIm	1,3-benzimidazolate
B_{index}	brittleness index
BTA	1,2,3-benzotriazole
C_2bpy	1-ethyl-[4,4′-bipyridin]-1-ium
C_4bpy	1-butyl-[4,4′-bipyridin]-1-ium
CGC	crystal-glass composite
ClbIm	5-chloro-1H-benzimidazole
CLH	constant load and hold
CP	coordination polymer
C_p	heat capacity
d	bond distance (Lindemann's rule)
DABCO	diazabicyclo[2,2,2]octane
DAC	diamond anvil cell
dema	diethylmethylammonium
dca	dicyanamide
DFT	density-functional theory
DMA	dynamic mechanical analysis
DSC	differential scanning calorimetry
E	Young's modulus
EDS	energy dispersive X-ray spectroscopy
EELS	electron energy loss spectroscopy
EIS	electrochemical impedance spectroscopy
EXAFS	extended X-ray absorption fine structure
FPMD	first-principles molecular dynamic
FSA^-	bis(fluorosulfonyl) imide anion
FSDP	first sharp diffraction peak
G	Gibbs free energy
GFA	glass forming ability
H_2dmbIm	protonated 5,6-dimethylbenzimidazole
H_2Im	imidazolium
HbIm	1,3-benzimidazole
HDA	high-density amorphous
HDL	high-density liquid
hfa^-	hexafluoroacetylacetonato anion
H_{fus}	enthalpy of fusion
hmba	N,N'-1,6-hexamethylenebis(acetamide)
HmbIm	2-methylbenzimidazole
HOIP	hybrid organic−inorganic perovskites
HTr	1,2,4-triazole
Im	imidazolate
IR	infrared
K_{Ic}	fracture toughness
LDA	low-density amorphous
LDL	low-density liquid
LLT	liquid−liquid phase transtion
m	liquid fragility
MAF	metal azolate frameworks (MAFs)
MAS	magic-angle spinning
mbIm	5-methybenzimidazolate
MeIm	2-methylimidazole
MD	molecular dynamic
m-dpeb	1,3-bis(diphenylphosphorylethynyl)benzene)
MIG	mechanical-induced glass
mL1	1,3,5-tris(3-cyanophenylethynyl)benzene
MOF	metal−organic framework
MQG	melt-quenched glass
ndc	1,4-naphthalenedicarboxylate
NIR	near-infrared
NLO	nonlinear optic

NMR	nuclear magnetic resonance
o-dpeb	1,2-bis(diphenylphosphorylethynyl)benzene)
O_h	octahedral
P	pressure
PALS	positron lifetime annihilation spectroscopy
p-dpeb	1,4-bis(diphenylphosphorylethynyl)benzene)
PDF	pair distribution function
Phbpy	1-phenyl-[4,4′-bipyridin]-1-ium
pL2	1,3,5-tris(4-cyanophenylethynyl)benzene
PMF	potential mean force
PXRD	powder X-ray diffraction
RDF	radial distribution function
RMC	Reverse Monte Carlo
SBU	secondary building unit
SCN	thiocyanate
SEM	scanning electron microscopy
SEPB	single-edge precracked beam
SEtPh	phenylethanethiolate
S_{fus}	entropy of fusion
S_{IAST}	selectivity based on ideal adsorption solution theory
SMePh	phenylmethanethiolate
SN	succinonitrile
SPh	thiophenolate
SRJ	strain-rate jump
STEM	scanning-transmission electron microscopy
T	temperature
TCT	topological constraint theory
T_d	decomposition temperature
T_d	tetrahedral
T_g	glass transition temperature
TGA	thermal gravimetric analysis
T_m	melting temperature
TMA	thermal mechanical analysis
TPrA	tetrapropylammonium
u	mean thermal atomic displacement (Lindemann's rule)
UV–vis	ultraviolet–visible spectroscopy
V	volume
VT	variable temperature
WAXS	wide-angle X-ray scattering
XAFS	X-ray absorption fine structure
XANES	X-ray absorption near edge structure
XAS	X-ray absorption spectroscopy
ZIF	zeolitic imidazolate framework
η	viscosity
κ	thermal conductivity
ν	Poisson's ratio

REFERENCES

(1) Eddaoudi, M.; Moler, D. B.; Li, H.; Chen, B.; Reineke, T. M.; O'Keeffe, M.; Yaghi, O. M. Modular Chemistry: Secondary Building Units as a Basis for the Design of Highly Porous and Robust Metal-Organic Carboxylate Frameworks. *Acc. Chem. Res.* **2001**, *34*, 319–330.

(2) Kitagawa, S.; Kitaura, R.; Noro, S.-i. Functional Porous Coordination Polymers. *Angew. Chem., Int. Ed.* **2004**, *43*, 2334–2375.

(3) Kitagawa, S.; Matsuda, R. Chemistry of Coordination Space of Porous Coordination Polymers. *Coord. Chem. Rev.* **2007**, *251*, 2490–2509.

(4) Furukawa, H.; Cordova, K. E.; O'Keeffe, M.; Yaghi, O. M. The Chemistry and Applications of Metal-Organic Frameworks. *Science* **2013**, *341*, 1230444.

(5) Horike, S.; Nagarkar, S. S.; Ogawa, T.; Kitagawa, S. New Dimension of Coordination Polymers and Metal-Organic Frame-

works toward Functional Glasses and Liquids. *Angew. Chem., Int. Ed.* **2020**, *59*, 6652.

(6) Kondo, M.; Yoshitomi, T.; Matsuzaka, H.; Kitagawa, S.; Seki, K. Three-Dimensional Framework with Channeling Cavities for Small Molecules: $\{[M_2(4, 4′-bpy)_3(NO_3)_4]\cdot xH_2O\}_n$ (M = Co, Ni, Zn). *Angew. Chem., Int. Ed. Engl.* **1997**, *36*, 1725–1727.

(7) Li, H.; Eddaoudi, M.; Groy, T. L.; Yaghi, O. M. Establishing Microporosity in Open Metal-Organic Frameworks: Gas Sorption Isotherms for Zn(BDC) (BDC = 1,4-Benzenedicarboxylate). *J. Am. Chem. Soc.* **1998**, *120*, 8571–8572.

(8) Yaghi, O. M.; O'Keeffe, M.; Ockwig, N. W.; Chae, H. K.; Eddaoudi, M.; Kim, J. Reticular Synthesis and the Design of New Materials. *Nature* **2003**, *423*, 705–714.

(9) Bétard, A.; Fischer, R. A. Metal-Organic Framework Thin Films: From Fundamentals to Applications. *Chem. Rev.* **2012**, *112*, 1055–1083.

(10) Sumida, K.; Rogow, D. L.; Mason, J. A.; McDonald, T. M.; Bloch, E. D.; Herm, Z. R.; Bae, T.-H.; Long, J. R. Carbon Dioxide Capture in Metal-Organic Frameworks. *Chem. Rev.* **2012**, *112*, 724–781.

(11) Stassen, I.; Burtch, N.; Talin, A.; Falcaro, P.; Allendorf, M.; Ameloot, R. An Updated Roadmap for the Integration of Metal-Organic Frameworks with Electronic Devices and Chemical Sensors. *Chem. Soc. Rev.* **2017**, *46*, 3185–3241.

(12) Bavykina, A.; Kolobov, N.; Khan, I. S.; Bau, J. A.; Ramirez, A.; Gascon, J. Metal-Organic Frameworks in Heterogeneous Catalysis: Recent Progress, New Trends, and Future Perspectives. *Chem. Rev.* **2020**, *120*, 8468–8535.

(13) Mancuso, J. L.; Mroz, A. M.; Le, K. N.; Hendon, C. H. Electronic Structure Modeling of Metal-Organic Frameworks. *Chem. Rev.* **2020**, *120*, 8641–8715.

(14) Lim, D.-W.; Kitagawa, H. Proton Transport in Metal-Organic Frameworks. *Chem. Rev.* **2020**, *120*, 8416–8467.

(15) Geng, K.; He, T.; Liu, R.; Dalapati, S.; Tan, K. T.; Li, Z.; Tao, S.; Gong, Y.; Jiang, Q.; Jiang, D. Covalent Organic Frameworks: Design, Synthesis, and Functions. *Chem. Rev.* **2020**, *120*, 8814–8933.

(16) Islamoglu, T.; Chen, Z.; Wasson, M. C.; Buru, C. T.; Kirlikovali, K. O.; Afrin, U.; Mian, M. R.; Farha, O. K. Metal-Organic Frameworks against Toxic Chemicals. *Chem. Rev.* **2020**, *120*, 8130–8160.

(17) Qian, Q.; Asinger, P. A.; Lee, M. J.; Han, G.; Mizrahi Rodriguez, K.; Lin, S.; Benedetti, F. M.; Wu, A. X.; Chi, W. S.; Smith, Z. P. MOF-Based Membranes for Gas Separations. *Chem. Rev.* **2020**, *120*, 8161–8266.

(18) Rice, A. M.; Martin, C. R.; Galitskiy, V. A.; Berseneva, A. A.; Leith, G. A.; Shustova, N. B. Photophysics Modulation in Photoswitchable Metal-Organic Frameworks. *Chem. Rev.* **2020**, *120*, 8790–8813.

(19) Rojas, S.; Horcajada, P. Metal-Organic Frameworks for the Removal of Emerging Organic Contaminants in Water. *Chem. Rev.* **2020**, *120*, 8378–8415.

(20) Thorarinsdottir, A. E.; Harris, T. D. Metal-Organic Framework Magnets. *Chem. Rev.* **2020**, *120*, 8716–8789.

(21) Bennett, T. D.; Horike, S. Liquid, Glass and Amorphous Solid States of Coordination Polymers and Metal-Organic Frameworks. *Nat. Rev. Mater.* **2018**, *3*, 431–440.

(22) Kitagawa, S. Future Porous Materials. *Acc. Chem. Res.* **2017**, *50*, 514–516.

(23) Angell, C. A. Formation of Glasses from Liquids and Biopolymers. *Science* **1995**, *267*, 1924–1935.

(24) Debenedetti, P. G.; Stillinger, F. H. Supercooled Liquids and the Glass Transition. *Nature* **2001**, *410*, 259–267.

(25) Greaves, G. N.; Sen, S. Inorganic Glasses, Glass-Forming Liquids and Amorphizing Solids. *Adv. Phys.* **2007**, *56*, 1–166.

(26) Umeyama, D.; Horike, S.; Inukai, M.; Itakura, T.; Kitagawa, S. Reversible Solid-to-Liquid Phase Transition of Coordination Polymer Crystals. *J. Am. Chem. Soc.* **2015**, *137*, 864–870.

(27) Bennett, T. D.; Tan, J.-C.; Yue, Y.; Baxter, E.; Ducati, C.; Terrill, N. J.; Yeung, H. H. M.; Zhou, Z.; Chen, W.; Henke, S.; et al.

A Self-archived copy in
Kyoto University Research Information Repository
https://repository.kulib.kyoto-u.ac.jp

京都大学
KYOTO UNIVERSITY

京都大学学術情報リポジトリ
KURENAI 紅
Kyoto University Research Information Repository

Hybrid Glasses from Strong and Fragile Metal-Organic Framework Liquids. *Nat. Commun.* **2015**, *6*, 8079.

(28) Wang, Y.; Jin, H.; Ma, Q.; Mo, K.; Mao, H.; Feldhoff, A.; Cao, X.; Li, Y.; Pan, F.; Jiang, Z. A MOF Glass Membrane for Gas Separation. *Angew. Chem., Int. Ed.* **2020**, *59*, 4365−4369.

(29) Li, J.; Wang, J.; Li, Q.; Zhang, M.; Li, J.; Sun, C.; Yuan, S.; Feng, X.; Wang, B. Coordination Polymer Glasses with Lava and Healing Ability for High-Performance Gas Sieving. *Angew. Chem. Int. Ed.* **2021**, *60*, 21304−21309.

(30) Tanaka, K.; Tago, Y.; Kondo, M.; Watanabe, Y.; Nishio, K.; Hitosugi, T.; Moriya, M. High Li-Ion Conductivity in Li{N(SO$_2$F)$_2$}-(NCCH$_2$CH$_2$CN)$_2$ Molecular Crystal. *Nano Lett.* **2020**, *20*, 8200−8204.

(31) Ogawa, T.; Takahashi, K.; Nagarkar, S. S.; Ohara, K.; Hong, Y.-l.; Nishiyama, Y.; Horike, S. Coordination Polymer Glass from Protic Ionic Liquid: Proton Conductivity and Mechanical Property as Electrolyte. *Chem. Sci.* **2020**, *11*, 5175−5181.

(32) Ma, N.; Kosasang, S.; Yoshida, A.; Horike, S. Proton-Conductive Coordination Polymer Glass for Solid-State Anhydrous Proton Batteries. *Chem. Sci.* **2021**, *12*, 5818−5824.

(33) Hirai, Y.; Nakanishi, T.; Kitagawa, Y.; Fushimi, K.; Seki, T.; Ito, H.; Fueno, H.; Tanaka, K.; Satoh, T.; Hasegawa, Y. Luminescent Coordination Glass: Remarkable Morphological Strategy for Assembled Eu(III) Complexes. *Inorg. Chem.* **2015**, *54*, 4364−4370.

(34) Vaidya, S.; Veselska, O.; Zhadan, A.; Diaz-Lopez, M.; Joly, Y.; Bordet, P.; Guillou, N.; Dujardin, C.; Ledoux, G.; Toche, F.; et al. Transparent and Luminescent Glasses of Gold Thiolate Coordination Polymers. *Chem. Sci.* **2020**, *11*, 6815−6823.

(35) Ali, M. A.; Liu, X.; Li, Y.; Ren, J.; Qiu, J. Nonlinear-Optical Response in Zeolitic Imidazolate Framework Glass. *Inorg. Chem.* **2020**, *59*, 8380−8386.

(36) Longley, L.; Collins, S. M.; Zhou, C.; Smales, G. J.; Norman, S. E.; Brownbill, N. J.; Ashling, C. W.; Chater, P. A.; Tovey, R.; Schönlieb, C.-B.; et al. Liquid Phase Blending of Metal-Organic Frameworks. *Nat. Commun.* **2018**, *9*, 2135.

(37) Ashling, C. W.; Johnstone, D. N.; Widmer, R. N.; Hou, J.; Collins, S. M.; Sapnik, A. F.; Bumstead, A. M.; Midgley, P. A.; Chater, P. A.; Keen, D. A.; et al. Synthesis and Properties of a Compositional Series of MIL-53(Al) Metal-Organic Framework Crystal-Glass Composites. *J. Am. Chem. Soc.* **2019**, *141*, 15641−15648.

(38) Hou, J.; Ashling, C. W.; Collins, S. M.; Krajnc, A.; Zhou, C.; Longley, L.; Johnstone, D. N.; Chater, P. A.; Li, S.; Coulet, M.-V.; et al. Metal-Organic Framework Crystal-Glass Composites. *Nat. Commun.* **2019**, *10*, 2580.

(39) Roberts, C. J.; Debenedetti, P. G. Polyamorphism and Density Anomalies in Network-Forming Fluids: Zeroth- and First-Order Approximations. *J. Chem. Phys.* **1996**, *105*, 658−672.

(40) Salmon, P. S.; Martin, R. A.; Mason, P. E.; Cuello, G. J. Topological Versus Chemical Ordering in Network Glasses at Intermediate and Extended Length Scales. *Nature* **2005**, *435*, 75−78.

(41) Liu, M.; McGillicuddy, R. D.; Vuong, H.; Tao, S.; Slavney, A. H.; Gonzalez, M. I.; Billinge, S. J. L.; Mason, J. A. Network-Forming Liquids from Metal-Bis(acetamide) Frameworks with Low Melting Temperatures. *J. Am. Chem. Soc.* **2021**, *143*, 2801−2811.

(42) Cairns, A. B.; Goodwin, A. L. Structural Disorder in Molecular Framework Materials. *Chem. Soc. Rev.* **2013**, *42*, 4881−4893.

(43) Cheetham, A. K.; Bennett, T. D.; Coudert, F. X.; Goodwin, A. L. Defects and Disorder in Metal Organic Frameworks. *Dalton Trans.* **2016**, *45*, 4113−4126.

(44) Tao, H.; Bennett, T. D.; Yue, Y. Melt-Quenched Hybrid Glasses from Metal-Organic Frameworks. *Adv. Mater.* **2017**, *29*, 1601705.

(45) Tuffnell, J. M.; Ashling, C. W.; Hou, J.; Li, S.; Longley, L.; Ríos Gómez, M. L.; Bennett, T. D. Novel Metal-Organic Framework Materials: Blends, Liquids, Glasses and Crystal-Glass Composites. *Chem. Commun.* **2019**, *55*, 8705−8715.

(46) Yin, Z.; Zhang, Y.-B.; Yu, H.-B.; Zeng, M.-H. How to Create MOF Glasses and Take Advantage of Emerging Opportunities. *Sci. Bull.* **2020**, *65*, 1432−1435.

(47) Fonseca, J.; Gong, T.; Jiao, L.; Jiang, H.-L. Metal-Organic Frameworks (MOFs) Beyond Crystallinity: Amorphous MOFs, MOF Liquids and MOF Glasses. *J. Mater. Chem. A* **2021**, *9*, 10562−10611.

(48) Horike, S.; Ma, N.; Fan, Z.; Kosasang, S.; Smedskjaer, M. M. Mechanics, Ionics, and Optics of Metal-Organic Framework and Coordination Polymer Glasses. *Nano Lett.* **2021**, *21*, 6382−6390.

(49) Shen, K.; Chen, X.; Chen, J.; Li, Y. Development of MOF-Derived Carbon-Based Nanomaterials for Efficient Catalysis. *ACS Catal.* **2016**, *6*, 5887−5903.

(50) Feng, L.; Wang, K.-Y.; Day, G. S.; Ryder, M. R.; Zhou, H.-C. Destruction of Metal-Organic Frameworks: Positive and Negative Aspects of Stability and Lability. *Chem. Rev.* **2020**, *120*, 13087−13133.

(51) Horike, S.; Umeyama, D.; Inukai, M.; Itakura, T.; Kitagawa, S. Coordination-Network-Based Ionic Plastic Crystal for Anhydrous Proton Conductivity. *J. Am. Chem. Soc.* **2012**, *134*, 7612−7615.

(52) Umeyama, D.; Horike, S.; Inukai, M.; Itakura, T.; Kitagawa, S. Inherent Proton Conduction in a 2D Coordination Framework. *J. Am. Chem. Soc.* **2012**, *134*, 12780−12785.

(53) Umeyama, D.; Horike, S.; Inukai, M.; Kitagawa, S. Integration of Intrinsic Proton Conduction and Guest-Accessible Nanospace into a Coordination Polymer. *J. Am. Chem. Soc.* **2013**, *135*, 11345−11350.

(54) Umeyama, D.; Funnell, N. P.; Cliffe, M. J.; Hill, J. A.; Goodwin, A. L.; Hijikata, Y.; Itakura, T.; Okubo, T.; Horike, S.; Kitagawa, S. Glass Formation via Structural Fragmentation of a 2D Coordination Network. *Chem. Commun.* **2015**, *51*, 12728−12731.

(55) Bennett, T. D.; Goodwin, A. L.; Dove, M. T.; Keen, D. A.; Tucker, M. G.; Barney, E. R.; Soper, A. K.; Bithell, E. G.; Tan, J.-C.; Cheetham, A. K. Structure and Properties of an Amorphous Metal-Organic Framework. *Phys. Rev. Lett.* **2010**, *104*, 115503.

(56) Bennett, T. D.; Cao, S.; Tan, J. C.; Keen, D. A.; Bithell, E. G.; Beldon, P. J.; Friscic, T.; Cheetham, A. K. Facile Mechanosynthesis of Amorphous Zeolitic Imidazolate Frameworks. *J. Am. Chem. Soc.* **2011**, *133*, 14546−14549.

(57) Bennett, T. D.; Simoncic, P.; Moggach, S. A.; Gozzo, F.; Macchi, P.; Keen, D. A.; Tan, J.-C.; Cheetham, A. K. Reversible Pressure-Induced Amorphization of a Zeolitic Imidazolate Framework (ZIF-4). *Chem. Commun.* **2011**, *47*, 7983−7985.

(58) Bennett, T. D.; Keen, D. A.; Tan, J.-C.; Barney, E. R.; Goodwin, A. L.; Cheetham, A. K. Thermal Amorphization of Zeolitic Imidazolate Frameworks. *Angew. Chem., Int. Ed.* **2011**, *50*, 3067−3071.

(59) Park, K. S.; Ni, Z.; Côté, A. P.; Choi, J. Y.; Huang, R.; Uribe-Romo, F. J.; Chae, H. K.; O'Keeffe, M.; Yaghi, O. M. Exceptional Chemical and Thermal Stability of Zeolitic Imidazolate Frameworks. *Proc. Natl. Acad. Sci. U. S. A.* **2006**, *103*, 10186−10191.

(60) Lehnert, R.; Seel, F. Darstellung und Kristallstruktur des Mangan(II)- und Zink(II)-Derivates des Imidazols. *Z. Anorg. Allg. Chem.* **1980**, *464*, 187−194.

(61) Gaillac, R.; Pullumbi, P.; Beyer, K. A.; Chapman, K. W.; Keen, D. A.; Bennett, T. D.; Coudert, F.-X. Liquid Metal-Organic Frameworks. *Nat. Mater.* **2017**, *16*, 1149−1154.

(62) Batten, S. R.; Champness, N. R.; Chen, X.-M.; Garcia-Martinez, J.; Kitagawa, S.; Öhrström, L.; O'Keeffe, M.; Paik Suh, M.; Reedijk, J. Terminology of Metal-Organic Frameworks and Coordination Polymers (IUPAC Recommendations 2013). *Pure Appl. Chem.* **2013**, *85*, 1715−1724.

(63) Öhrström, L. Let's Talk about MOFs—Topology and Terminology of Metal-Organic Frameworks and Why We Need Them. *Crystals* **2015**, *5*, 154.

(64) Scholze, H., Nature and Structure of Glass. *Glass: Nature, Structure, and Properties*; Springer: New York, 1991; pp 3−155.

(65) Conradt, R. Thermodynamics and Kinetics of Glass. *Springer Handbook of Glass*; Springer: Cham, 2019; pp 51−77.

(66) Zheng, Q.; Zhang, Y.; Montazerian, M.; Gulbiten, O.; Mauro, J. C.; Zanotto, E. D.; Yue, Y. Understanding Glass through Differential Scanning Calorimetry. *Chem. Rev.* **2019**, *119*, 7848−7939.

(67) Bennett, T. D.; Cheetham, A. K. Amorphous Metal-Organic Frameworks. *Acc. Chem. Res.* **2014**, *47*, 1555−1562.

(68) Lin, I. J. B.; Vasam, C. S. Metal-Containing Ionic Liquids and Ionic Liquid Crystals Based on Imidazolium Moiety. *J. Organomet. Chem.* **2005**, *690*, 3498−3512.

(69) Goossens, K.; Lava, K.; Bielawski, C. W.; Binnemans, K. Ionic Liquid Crystals: Versatile Materials. *Chem. Rev.* **2016**, *116*, 4643−4807.

(70) Prodius, D.; Mudring, A.-V. Rare Earth Metal-Containing Ionic Liquids. *Coord. Chem. Rev.* **2018**, *363*, 1−16.

(71) Yanagisawa, J.; Hiraoka, T.; Kobayashi, F.; Saito, D.; Yoshida, M.; Kato, M.; Takeiri, F.; Kobayashi, G.; Ohba, M.; Lindoy, L. F.; et al. Luminescent Ionic Liquid Formed from a Melted Rhenium(V) Cluster. *Chem. Commun.* **2020**, *56*, 7957−7960.

(72) Zhukhovitskiy, A. V.; Zhong, M.; Keeler, E. G.; Michaelis, V. K.; Sun, J. E. P.; Hore, M. J. A.; Pochan, D. J.; Griffin, R. G.; Willard, A. P.; Johnson, J. A. Highly Branched and Loop-Rich Gels via Formation of Metal-Organic Cages Linked by Polymers. *Nat. Chem.* **2016**, *8*, 33−41.

(73) Nagarkar, S. S.; Tsujimoto, M.; Kitagawa, S.; Hosono, N.; Horike, S. Modular Self-Assembly and Dynamics in Coordination Star Polymer Glasses: New Media for Ion Transport. *Chem. Mater.* **2018**, *30*, 8555−8561.

(74) Legrand, A.; Craig, G. A.; Bonneau, M.; Minami, S.; Urayama, K.; Furukawa, S. Understanding the Multiscale Self-Assembly of Metal-Organic Polyhedra Towards Functionally Graded Porous Gels. *Chem. Sci.* **2019**, *10*, 10833−10842.

(75) Craig, G. A.; Larpent, P.; Urabe, H.; Legrand, A.; Bonneau, M.; Kusaka, S.; Furukawa, S. Hysteresis in the Gas Sorption Isotherms of Metal-Organic Cages Accompanied by Subtle Changes in Molecular Packing. *Chem. Commun.* **2020**, *56*, 3689−3692.

(76) Legrand, A.; Liu, L.-H.; Royla, P.; Aoyama, T.; Craig, G. A.; Carné-Sánchez, A.; Urayama, K.; Weigand, J. J.; Lin, C.-H.; Furukawa, S. Spatiotemporal Control of Supramolecular Polymerization and Gelation of Metal-Organic Polyhedra. *J. Am. Chem. Soc.* **2021**, *143*, 3562−3570.

(77) Wang, Z.; Craig, G. A.; Legrand, A.; Haase, F.; Minami, S.; Urayama, K.; Furukawa, S. Porous Colloidal Hydrogels Formed by Coordination-Driven Self-Assembly of Charged Metal-Organic Polyhedra. *Chem. - Asian J.* **2021**, *16*, 1092−1100.

(78) Pachfule, P.; Shinde, D.; Majumder, M.; Xu, Q. Fabrication of Carbon Nanorods and Graphene Nanoribbons from a Metal-Organic Framework. *Nat. Chem.* **2016**, *8*, 718−724.

(79) Wang, H.-F.; Chen, L.; Pang, H.; Kaskel, S.; Xu, Q. MOF-Derived Electrocatalysts for Oxygen Reduction, Oxygen Evolution and Hydrogen Evolution Reactions. *Chem. Soc. Rev.* **2020**, *49*, 1414−1448.

(80) Keen, D. A.; Bennett, T. D. Structural Investigations of Amorphous Metal-Organic Frameworks Formed via Different Routes. *Phys. Chem. Chem. Phys.* **2018**, *20*, 7857−7861.

(81) Chen, W.; Horike, S.; Umeyama, D.; Ogiwara, N.; Itakura, T.; Tassel, C.; Goto, Y.; Kageyama, H.; Kitagawa, S. Glass Formation of a Coordination Polymer Crystal for Enhanced Proton Conductivity and Material Flexibility. *Angew. Chem., Int. Ed.* **2016**, *55*, 5195−5200.

(82) Ciriminna, R.; Fidalgo, A.; Pandarus, V.; Béland, F.; Ilharco, L. M.; Pagliaro, M. The Sol-Gel Route to Advanced Silica-Based Materials and Recent Applications. *Chem. Rev.* **2013**, *113*, 6592−6620.

(83) Keen, D. A.; Goodwin, A. L. The Crystallography of Correlated Disorder. *Nature* **2015**, *521*, 303−309.

(84) Widmer, R. N.; Lampronti, G. I.; Anzellini, S.; Gaillac, R.; Farsang, S.; Zhou, C.; Belenguer, A. M.; Wilson, C. W.; Palmer, H.; Kleppe, A. K.; et al. Pressure Promoted Low-Temperature Melting of Metal-Organic Frameworks. *Nat. Mater.* **2019**, *18*, 370−376.

(85) Lindemann, F. A. *Phys. Z.* **1910**, *11* (14), 609−612.

(86) Bordiga, S.; Bonino, F.; Lillerud, K. P.; Lamberti, C. X-Ray Absorption Spectroscopies: Useful Tools to Understand Metal-lorganic Frameworks Structure and Reactivity. *Chem. Soc. Rev.* **2010**, *39*, 4885−4927.

(87) Yang, Y.; Shin, Y. K.; Li, S.; Bennett, T. D.; van Duin, A. C. T.; Mauro, J. C. Enabling Computational Design of ZIFs Using ReaxFF. *J. Phys. Chem. B* **2018**, *122*, 9616−9624.

(88) To, T.; Sørensen, S. S.; Yue, Y.; Smedskjaer, M. M. Bond Switching Is Responsible for Nanoductility in Zeolitic Imidazolate Framework Glasses. *Dalton Trans.* **2021**, *50*, 6126−6132.

(89) Thornton, A. W.; Jelfs, K. E.; Konstas, K.; Doherty, C. M.; Hill, A. J.; Cheetham, A. K.; Bennett, T. D. Porosity in Metal-Organic Framework Glasses. *Chem. Commun.* **2016**, *52*, 3750−3753.

(90) Koontz, E. Thermal Analysis of Glass. *Springer Handbook of Glass*; Springer: Cham, 2019; pp 853−878.

(91) Ohara, Y.; Hinokimoto, A.; Chen, W.; Kitao, T.; Nishiyama, Y.; Hong, Y.-l.; Kitagawa, S.; Horike, S. Formation of Coordination Polymer Glass by Mechanical Milling: Dependence on Metal Ions and Molecular Doping for H$^+$ Conductivity. *Chem. Commun.* **2018**, *54*, 6859−6862.

(92) Das, C.; Ogawa, T.; Horike, S. Stable Melt Formation of 2D Nitrile-Based Coordination Polymer and Hierarchical Crystal-Glass Structuring. *Chem. Commun.* **2020**, *56*, 8980−8983.

(93) Das, C.; Horike, S. Crystal Melting and Vitrification Behaviors of a Three-Dimensional Nitrile-Based Metal-Organic Framework. *Faraday Discuss.* **2021**, *225*, 403−413.

(94) Qiao, A.; Bennett, T. D.; Tao, H.; Krajnc, A.; Mali, G.; Doherty, C. M.; Thornton, A. W.; Mauro, J. C.; Greaves, G. N.; Yue, Y. A Metal-Organic Framework with Ultrahigh Glass-Forming Ability. *Sci. Adv.* **2018**, *4*, No. eaao6827.

(95) Ito, K.; Moynihan, C. T.; Angell, C. A. Thermodynamic Determination of Fragility in Liquids and a Fragile-to-Strong Liquid Transition in Water. *Nature* **1999**, *398*, 492−495.

(96) Mauro, J. C.; Yue, Y.; Ellison, A. J.; Gupta, P. K.; Allan, D. C. Viscosity of Glass-Forming Liquids. *Proc. Natl. Acad. Sci. U. S. A.* **2009**, *106*, 19780−19784.

(97) Shaw, B. K.; Hughes, A. R.; Ducamp, M.; Moss, S.; Debnath, A.; Sapnik, A. F.; Thorne, M. F.; McHugh, L. N.; Pugliese, A.; Keeble, D. S.; et al. Melting of Hybrid Organic-Inorganic Perovskites. *Nat. Chem.* **2021**, *13*, 778−785.

(98) Hadjiivanov, K. I.; Panayotov, D. A.; Mihaylov, M. Y.; Ivanova, E. Z.; Chakarova, K. K.; Andonova, S. M.; Drenchev, N. L. Power of Infrared and Raman Spectroscopies to Characterize Metal-Organic Frameworks and Investigate Their Interaction with Guest Molecules. *Chem. Rev.* **2021**, *121*, 1286−1424.

(99) Itakura, T.; Matsui, H.; Tada, T.; Kitagawa, S.; Demessence, A.; Horike, S. The Role of Lattice Vibration in the Terahertz Region for Proton Conduction in 2D Metal-Organic Frameworks. *Chem. Sci.* **2020**, *11*, 1538−1541.

(100) Hou, J.; Ríos Gómez, M. L.; Krajnc, A.; McCaul, A.; Li, S.; Bumstead, A. M.; Sapnik, A. F.; Deng, Z.; Lin, R.; Chater, P. A.; et al. Halogenated Metal-Organic Framework Glasses and Liquids. *J. Am. Chem. Soc.* **2020**, *142*, 3880−3890.

(101) Bennett, T. D.; Yue, Y.; Li, P.; Qiao, A.; Tao, H.; Greaves, N. G.; Richards, T.; Lampronti, G. I.; Redfern, S. A. T.; Blanc, F.; et al. Melt-Quenched Glasses of Metal-Organic Frameworks. *J. Am. Chem. Soc.* **2016**, *138*, 3484−3492.

(102) Zhou, C.; Longley, L.; Krajnc, A.; Smales, G. J.; Qiao, A.; Erucar, I.; Doherty, C. M.; Thornton, A. W.; Hill, A. J.; Ashling, C. W.; et al. Metal-Organic Framework Glasses with Permanent Accessible Porosity. *Nat. Commun.* **2018**, *9*, 5042.

(103) Madsen, R. S. K.; Qiao, A.; Sen, J.; Hung, I.; Chen, K.; Gan, Z.; Sen, S.; Yue, Y. Ultrahigh-Field ^{67}Zn NMR Reveals Short-Range Disorder in Zeolitic Imidazolate Framework Glasses. *Science* **2020**, *367*, 1473.

(104) Lengke, M. F.; Ravel, B.; Fleet, M. E.; Wanger, G.; Gordon, R. A.; Southam, G. Mechanisms of Gold Bioaccumulation by Filamentous Cyanobacteria from Gold(III)-Chloride Complex. *Environ. Sci. Technol.* **2006**, *40*, 6304−6309.

(105) Li, S.; Limbach, R.; Longley, L.; Shirzadi, A. A.; Walmsley, J. C.; Johnstone, D. N.; Midgley, P. A.; Wondraczek, L.; Bennett, T. D. Mechanical Properties and Processing Techniques of Bulk Metal-

Organic Framework Glasses. *J. Am. Chem. Soc.* **2019**, *141*, 1027−1034.

(106) Stepniewska, M.; Januchta, K.; Zhou, C.; Qiao, A.; Smedskjaer, M. M.; Yue, Y. Observation of Indentation-Induced Shear Bands in a Metal-Organic Framework Glass. *Proc. Natl. Acad. Sci. U. S. A.* **2020**, *117*, 10149−10154.

(107) Collins, S. M.; Kepaptsoglou, D. M.; Butler, K. T.; Longley, L.; Bennett, T. D.; Ramasse, Q. M.; Midgley, P. A. Subwavelength Spatially Resolved Coordination Chemistry of Metal-Organic Framework Glass Blends. *J. Am. Chem. Soc.* **2018**, *140*, 17862−17866.

(108) Longley, L.; Calahoo, C.; Limbach, R.; Xia, Y.; Tuffnell, J. M.; Sapnik, A. F.; Thorne, M. F.; Keeble, D. S.; Keen, D. A.; Wondraczek, L.; et al. Metal-Organic Framework and Inorganic Glass Composites. *Nat. Commun.* **2020**, *11*, 5800.

(109) Collins, S. M.; MacArthur, K. E.; Longley, L.; Tovey, R.; Benning, M.; Schönlieb, C.-B.; Bennett, T. D.; Midgley, P. A. Phase Diagrams of Liquid-Phase Mixing in Multi-Component Metal-Organic Framework Glasses Constructed by Quantitative Elemental Nano-Tomography. *APL Mater.* **2019**, *7*, 091111.

(110) Xie, L. S.; Skorupskii, G.; Dincǎ, M. Electrically Conductive Metal-Organic Frameworks. *Chem. Rev.* **2020**, *120*, 8536−8580.

(111) Sørensen, S. S.; Østergaard, M. B.; Stepniewska, M.; Johra, H.; Yue, Y.; Smedskjaer, M. M. Metal-Organic Framework Glasses Possess Higher Thermal Conductivity than Their Crystalline Counterparts. *ACS Appl. Mater. Interfaces* **2020**, *12*, 18893−18903.

(112) Qiao, A.; Tao, H.; Carson, M. P.; Aldrich, S. W.; Thirion, L. M.; Bennett, T. D.; Mauro, J. C.; Yue, Y. Optical Properties of a Melt-Quenched Metal-Organic Framework Glass. *Opt. Lett.* **2019**, *44*, 1623−1625.

(113) To, T.; Sørensen, S. S.; Stepniewska, M.; Qiao, A.; Jensen, L. R.; Bauchy, M.; Yue, Y.; Smedskjaer, M. M. Fracture Toughness of a Metal-Organic Framework Glass. *Nat. Commun.* **2020**, *11*, 2593.

(114) Frentzel-Beyme, L.; Kloß, M.; Pallach, R.; Salamon, S.; Moldenhauer, H.; Landers, J.; Wende, H.; Debus, J.; Henke, S. Porous Purple Glass - a Cobalt Imidazolate Glass with Accessible Porosity from a Meltable Cobalt Imidazolate Framework. *J. Mater. Chem. A* **2019**, *7*, 985−990.

(115) Nagarkar, S. S.; Kurasho, H.; Duong, N. T.; Nishiyama, Y.; Kitagawa, S.; Horike, S. Crystal Melting and Glass Formation in Copper Thiocyanate Based Coordination Polymers. *Chem. Commun.* **2019**, *55*, 5455−5458.

(116) Frentzel-Beyme, L.; Kloß, M.; Kolodzeiski, P.; Pallach, R.; Henke, S. Meltable Mixed-Linker Zeolitic Imidazolate Frameworks and Their Microporous Glasses: From Melting Point Engineering to Selective Hydrocarbon Sorption. *J. Am. Chem. Soc.* **2019**, *141*, 12362−12371.

(117) Kimata, H.; Mochida, T. Crystal Structures and Melting Behaviors of 2D and 3D Anionic Coordination Polymers Containing Organometallic Ionic Liquid Components. *Chem. - Eur. J.* **2019**, *25*, 10111−10117.

(118) Dupont, J. From Molten Salts to Ionic Liquids: A "Nano" Journey. *Acc. Chem. Res.* **2011**, *44*, 1223−1231.

(119) Izgorodina, E. I.; Seeger, Z. L.; Scarborough, D. L. A.; Tan, S. Y. S. Quantum Chemical Methods for the Prediction of Energetic, Physical, and Spectroscopic Properties of Ionic Liquids. *Chem. Rev.* **2017**, *117*, 6696−6754.

(120) Butler, K. T.; Walsh, A.; Cheetham, A. K.; Kieslich, G. Organised Chaos: Entropy in Hybrid Inorganic-Organic Systems and Other Materials. *Chem. Sci.* **2016**, *7*, 6316−6324.

(121) Smedskjaer, M. M.; Sørensen, S. S. A Glass Act. *Nat. Chem.* **2021**, *13*, 723−724.

(122) Suzuya, K.; Itoh, K.; Kajinami, A.; Loong, C. K. The Structure of Binary Zinc Phosphate Glasses. *J. Non-Cryst. Solids* **2004**, *345−346*, 80−87.

(123) Inukai, M.; Horike, S.; Chen, W.; Umeyama, D.; Itakura, T.; Kitagawa, S. Template-Directed Proton Conduction Pathways in a Coordination Framework. *J. Mater. Chem. A* **2014**, *2*, 10404−10409.

(124) Rose, J.; Moulin, I.; Masion, A.; Bertsch, P. M.; Wiesner, M. R.; Bottero, J.-Y.; Mosnier, F.; Haehnel, C. X-Ray Absorption Spectroscopy Study of Immobilization Processes for Heavy Metals in Calcium Silicate Hydrates. 2. Zinc. *Langmuir* **2001**, *17*, 3658−3665.

(125) Inukai, M.; Nishiyama, Y.; Honjo, K.; Das, C.; Kitagawa, S.; Horike, S. Glass-Phase Coordination Polymer Displaying Proton Conductivity and Guest-Accessible Porosity. *Chem. Commun.* **2019**, *55*, 8528−8531.

(126) Zhang, J.-P.; Zhang, Y.-B.; Lin, J.-B.; Chen, X.-M. Metal Azolate Frameworks: From Crystal Engineering to Functional Materials. *Chem. Rev.* **2012**, *112*, 1001−1033.

(127) Greaves, G. N.; Meneau, F.; Sapelkin, A.; Colyer, L. M.; ap Gwynn, I.; Wade, S.; Sankar, G. The Rheology of Collapsing Zeolites Amorphized by Temperature and Pressure. *Nat. Mater.* **2003**, *2*, 622−629.

(128) Greaves, G. N.; Meneau, F.; Majérus, O.; Jones, D. G.; Taylor, J. Identifying Vibrations That Destabilize Crystals and Characterize the Glassy State. *Science* **2005**, *308*, 1299−1302.

(129) Angell, C. A.; Moynihan, C. T.; Hemmati, M. ʽStrong' and ʽSuperstrong' Liquids, and an Approach to the Perfect Glass State via Phase Transition. *J. Non-Cryst. Solids* **2000**, *274*, 319−331.

(130) Angell, C. A. Liquid Fragility and the Glass Transition in Water and Aqueous Solutions. *Chem. Rev.* **2002**, *102*, 2627−2650.

(131) Zhang, J.; Longley, L.; Liu, H.; Ashling, C. W.; Chater, P. A.; Beyer, K. A.; Chapman, K. W.; Tao, H.; Keen, D. A.; Bennett, T. D.; et al. Structural Evolution in a Melt-Quenched Zeolitic Imidazolate Framework Glass During Heat-Treatment. *Chem. Commun.* **2019**, *55*, 2521−2524.

(132) Tian, Y.-Q.; Zhao, Y.-M.; Chen, Z.-X.; Zhang, G.-N.; Weng, L.-H.; Zhao, D.-Y. Design and Generation of Extended Zeolitic Metal-Organic Frameworks (ZMOFs): Synthesis and Crystal Structures of Zinc(II) Imidazolate Polymers with Zeolitic Topologies. *Chem. - Eur. J.* **2007**, *13*, 4146−4154.

(133) Gaillac, R.; Pullumbi, P.; Coudert, F.-X. Melting of Zeolitic Imidazolate Frameworks with Different Topologies: Insight from First-Principles Molecular Dynamics. *J. Phys. Chem. C* **2018**, *122*, 6730−6736.

(134) Gaillac, R.; Pullumbi, P.; Bennett, T. D.; Coudert, F.-X. Structure of Metal-Organic Framework Glasses by *Ab Initio* Molecular Dynamics. *Chem. Mater.* **2020**, *32*, 8004−8011.

(135) Kauzmann, W. The Nature of the Glassy State and the Behavior of Liquids at Low Temperatures. *Chem. Rev.* **1948**, *43*, 219−256.

(136) Zhou, C.; Stepniewska, M.; Longley, L.; Ashling, C. W.; Chater, P. A.; Keen, D. A.; Bennett, T. D.; Yue, Y. Thermodynamic Features and Enthalpy Relaxation in a Metal-Organic Framework Glass. *Phys. Chem. Chem. Phys.* **2018**, *20*, 18291−18296.

(137) Widmer, R. N.; Lampronti, G. I.; Chibani, S.; Wilson, C. W.; Anzellini, S.; Farsang, S.; Kleppe, A. K.; Casati, N. P. M.; MacLeod, S. G.; Redfern, S. A. T.; et al. Rich Polymorphism of a Metal-Organic Framework in Pressure-Temperature Space. *J. Am. Chem. Soc.* **2019**, *141*, 9330−9337.

(138) Yang, Y.; Wilkinson, C. J.; Lee, K.-H.; Doss, K.; Bennett, T. D.; Shin, Y. K.; van Duin, A. C. T.; Mauro, J. C. Prediction of the Glass Transition Temperatures of Zeolitic Imidazolate Glasses through Topological Constraint Theory. *J. Phys. Chem. Lett.* **2018**, *9*, 6985−6990.

(139) Ríos Gómez, M. L.; Lampronti, G. I.; Yang, Y.; Mauro, J. C.; Bennett, T. D. Relating Structural Disorder and Melting in Complex Mixed Ligand Zeolitic Imidazolate Framework Glasses. *Dalton Trans.* **2020**, *49*, 850−857.

(140) Ali, M. A.; Ren, J.; Zhao, T.; Liu, X.; Hua, Y.; Yue, Y.; Qiu, J. Broad Mid-Infrared Luminescence in a Metal-Organic Framework Glass. *ACS Omega* **2019**, *4*, 12081−12087.

(141) Thorne, M. F.; Gómez, M. L. R.; Bumstead, A. M.; Li, S.; Bennett, T. D. Mechanochemical Synthesis of Mixed Metal, Mixed Linker, Glass-Forming Metal-Organic Frameworks. *Green Chem.* **2020**, *22*, 2505−2512.

(142) Nozari, V.; Calahoo, C.; Longley, L.; Bennett, T. D.; Wondraczek, L. Structural Integrity, Meltability, and Variability of

Thermal Properties in the Mixed-Linker Zeolitic Imidazolate Framework ZIF-62. *J. Chem. Phys.* **2020**, *153*, 204501.

(143) Bumstead, A. M.; Ríos Gómez, M. L.; Thorne, M. F.; Sapnik, A. F.; Longley, L.; Tuffnell, J. M.; Keeble, D. S.; Keen, D. A.; Bennett, T. D. Investigating the Melting Behaviour of Polymorphic Zeolitic Imidazolate Frameworks. *CrystEngComm* **2020**, *22*, 3627−3637.

(144) Bumstead, A. M.; Thorne, M. F.; Bennett, T. D. Identifying the Liquid and Glassy States of Coordination Polymers and Metal-Organic Frameworks. *Faraday Discuss.* **2021**, *225*, 210−225.

(145) Zhang, J.; Qiao, A.; Tao, H.; Yue, Y. Synthesis, Phase Transitions and Vitrification of the Zeolitic Imidazolate Framework: ZIF-4. *J. Non-Cryst. Solids* **2019**, *525*, 119665.

(146) Yu, Y.; Qiao, A.; Bumstead, A. M.; Bennett, T. D.; Yue, Y.; Tao, H. Impact of 1-Methylimidazole on Crystal Formation, Phase Transitions, and Glass Formation in a Zeolitic Imidazolate Framework. *Cryst. Growth Des.* **2020**, *20*, 6528−6534.

(147) Prananto, Y. P. Coordination Polymer of M(II)-Pyrazinamide (M = Co, Cd) with Double End-to-End Thiocyanate Bridge. *IOP Conf. Ser.: Mater. Sci. Eng.* **2018**, *299*, 012032.

(148) Spielberg, E. T.; Edengeiser, E.; Mallick, B.; Havenith, M.; Mudring, A.-V. (1-Butyl-4-Methyl-Pyridinium)[Cu(SCN)₂]: A Coordination Polymer and Ionic Liquid. *Chem.—Eur. J.* **2014**, *20*, 5338−5345.

(149) Su, Y.-J.; Cui, Y.-L.; Wang, Y.; Lin, R.-B.; Zhang, W.-X.; Zhang, J.-P.; Chen, X.-M. Copper(I) 2-Isopropylimidazolate: Supramolecular Isomerism, Isomerization, and Luminescent Properties. *Cryst. Growth Des.* **2015**, *15*, 1735−1739.

(150) Willart, J.; De Gusseme, A.; Hemon, S.; Odou, G.; Danede, F.; Descamps, M. Direct Crystal to Glass Transformation of Trehalose Induced by Ball Milling. *Solid State Commun.* **2001**, *119*, 501−505.

(151) Fukunaga, T.; Utsumi, M.; Akatsuka, H.; Misawa, M.; Mizutani, U. Structure of Amorphous Se Prepared by Milling. *J. Non-Cryst. Solids* **1996**, *205−207*, 531−535.

(152) Jóvári, P.; Delaplane, R. G.; Pusztai, L. Structural Models of Amorphous Selenium. *Phys. Rev. B: Condens. Matter Mater. Phys.* **2003**, *67*, 172201.

(153) Zhao, Y. H.; Lu, K.; Liu, T. Exafs Study of Mechanical-Milling-Induced Solid-State Amorphization of Se. *J. Non-Cryst. Solids* **2004**, *333*, 246−251.

(154) Joraid, A. A.; Alamri, S. N.; Abu-Sehly, A. A.; Benghanem, M. Nonisothermal Crystallisation Kinetics of Amorphous Selenium Prepared by High-Energy Ball Milling: A Comparison with the Melt-Quenching and Thin-Film Techniques. *J. Non-Cryst. Solids* **2012**, *358*, 1268−1273.

(155) Suzuki, K. A Structural Study of the Solid State Vitrification of Metals and Oxides by Ball Milling. *J. Non-Cryst. Solids* **1989**, *112*, 23−32.

(156) Fecht, H. J.; Han, G.; Fu, Z.; Johnson, W. L. Metastable Phase Formation in the Zr-Al Binary System Induced by Mechanical Alloying. *J. Appl. Phys.* **1990**, *67*, 1744−1748.

(157) Font, J.; Muntasell, J.; Cesari, E. Amorphization of Organic Compounds by Ball Milling. *Mater. Res. Bull.* **1997**, *32*, 1691−1696.

(158) Nagahama, M.; Suga, H.; Andersson, O. Formation of Molecular Alloys by Solid-State Vitrification. *Thermochim. Acta* **2000**, *363*, 165−174.

(159) Willart, J.; Descamps, N.; Caron, V.; Capet, F.; Danede, F.; Descamps, M. Formation of Lactose-Mannitol Molecular Alloys by Solid State Vitrification. *Solid State Commun.* **2006**, *138*, 194−199.

(160) Willart, J.; Dudognon, E.; Descamps, N.; Larsson, T.; Descamps, M. Lactose-Based Molecular Alloys Obtained by Solid State Vitrification. *J. Non-Cryst. Solids* **2006**, *352*, 4475−4479.

(161) Descamps, M.; Willart, J.; Dudognon, E.; Caron, V. Transformation of Pharmaceutical Compounds Upon Milling and Comilling: The Role of Tg. *J. Pharm. Sci.* **2007**, *96*, 1398−1407.

(162) Willart, J.; Descamps, M. Solid State Amorphization of Pharmaceuticals. *Mol. Pharmaceutics* **2008**, *5*, 905−920.

(163) Willart, J.-F.; Carpentier, L.; Danède, F.; Descamps, M. Solid-State Vitrification of Crystalline Griseofulvin by Mechanical Milling. *J. Pharm. Sci.* **2012**, *101*, 1570−1577.

(164) Morris, J. W.; Krenn, C. R. The Internal Stability of an Elastic Solid. *Philos. Mag. A* **2000**, *80*, 2827−2840.

(165) Ortiz, A. U.; Boutin, A.; Fuchs, A. H.; Coudert, F.-X. Investigating the Pressure-Induced Amorphization of Zeolitic Imidazolate Framework ZIF-8: Mechanical Instability Due to Shear Mode Softening. *J. Phys. Chem. Lett.* **2013**, *4*, 1861−1865.

(166) Hoang, H. T.; Nguyen, H. L.; Phan, T. B.; Bureekaew, S.; Kawazoe, Y.; Nguyen-Manh, D.; Le, H. M. From Reticular Chemistry Design to Density Functional Theory Modeling for New Zeolitic Imidazolate Framework Topologies: Mechanical Stability, Electronic Structure, and Co2 Selectivity. *J. Phys. Chem. C* **2018**, *122*, 23543−23553.

(167) Stillinger, F. H. A Topographic View of Supercooled Liquids and Glass Formation. *Science* **1995**, *267*, 1935−1939.

(168) Baxter, E. F.; Bennett, T. D.; Cairns, A. B.; Brownbill, N. J.; Goodwin, A. L.; Keen, D. A.; Chater, P. A.; Blanc, F.; Cheetham, A. K. A Comparison of the Amorphization of Zeolitic Imidazolate Frameworks (ZIFs) and Aluminosilicate Zeolites by Ball-Milling. *Dalton Trans.* **2016**, *45*, 4258−4268.

(169) Burmeister, C.; Titscher, L.; Breitung-Faes, S.; Kwade, A. Dry Grinding in Planetary Ball Mills: Evaluation of a Stressing Model. *Adv. Powder Technol.* **2018**, *29*, 191−201.

(170) Boström, H. L. B.; Collings, I. E.; Daisenberger, D.; Ridley, C. J.; Funnell, N. P.; Cairns, A. B. Probing the Influence of Defects, Hydration, and Composition on Prussian Blue Analogues with Pressure. *J. Am. Chem. Soc.* **2021**, *143*, 3544−3554.

(171) Thorne, M. F.; Sapnik, A. F.; McHugh, L. N.; Bumstead, A. M.; Castillo-Blas, C.; Keeble, D. S.; Diaz Lopez, M.; Chater, P. A.; Keen, D. A.; Bennett, T. D. Glassy Behaviour of Mechanically Amorphised ZIF-62 Isomorphs. *Chem. Commun.* **2021**, *57*, 9272−9275.

(172) Vaidya, S.; Veselska, O.; Zhadan, A.; Daniel, M.; Ledoux, G.; Fateeva, A.; Tsuruoka, T.; Demessence, A. Flexible and Luminescent Fibers of a 1D Au(I)-Thiophenolate Coordination Polymer and Formation of Gold Nanoparticle-Based Composite Materials for Sers. *J. Mater. Chem. C* **2020**, *8*, 8018−8027.

(173) Funasako, Y.; Mori, S.; Mochida, T. Reversible Transformation between Ionic Liquids and Coordination Polymers by Application of Light and Heat. *Chem. Commun.* **2016**, *52*, 6277−6279.

(174) Ueda, T.; Tominaga, T.; Mochida, T.; Takahashi, K.; Kimura, S. Photogeneration of Microporous Amorphous Coordination Polymers from Organometallic Ionic Liquids. *Chem. - Eur. J.* **2018**, *24*, 9490−9493.

(175) Sumitani, R.; Mochida, T. Metal-Containing Poly(Ionic Liquid) Exhibiting Photogeneration of Coordination Network: Reversible Control of Viscoelasticity and Ionic Conductivity. *Macromolecules* **2020**, *53*, 6968−6974.

(176) Kulachenkov, N. K.; Bruyere, S.; Sapchenko, S. A.; Mezenov, Y. A.; Sun, D.; Krasilin, A. A.; Nominé, A.; Ghanbaja, J.; Belmonte, T.; Fedin, V. P.; et al. Ultrafast Melting of Metal-Organic Frameworks for Advanced Nanophotonics. *Adv. Funct. Mater.* **2020**, *30*, 1908292.

(177) Panda, T.; Horike, S.; Hagi, K.; Ogiwara, N.; Kadota, K.; Itakura, T.; Tsujimoto, M.; Kitagawa, S. Mechanical Alloying of Metal-Organic Frameworks. *Angew. Chem., Int. Ed.* **2017**, *56*, 2413−2417.

(178) Longley, L.; Collins, S. M.; Li, S.; Smales, G. J.; Erucar, I.; Qiao, A.; Hou, J.; Doherty, C. M.; Thornton, A. W.; Hill, A. J.; et al. Flux Melting of Metal-Organic Frameworks. *Chem. Sci.* **2019**, *10*, 3592−3601.

(179) Nozari, V.; Calahoo, C.; Tuffnell, J. M.; Keen, D. A.; Bennett, T. D.; Wondraczek, L. Ionic Liquid Facilitated Melting of the Metal-Organic Framework ZIF-8. *Nat. Commun.* **2021**, *12*, 5703.

(180) Ashling, C. W.; Macreadie, L.; Southern, T.; Zhang, Y.; McHugh, L. N.; Evans, R. C.; Kaskel, S.; Telfer, S.; Bennett, T. D. Guest Size Limitation in Metal-Organic Framework Crystal-Glass Composites. *J. Mater. Chem. A* **2021**, *9*, 8386−8393.

(181) Li, S.; Yu, S.; Collins, S. M.; Johnstone, D. N.; Ashling, C. W.; Sapnik, A. F.; Chater, P. A.; Keeble, D. S.; McHugh, L. N.; Midgley, P.

京都大学
KYOTO UNIVERSITY

京都大学学術情報リポジトリ
KURENAI 紅
Kyoto University Research Information Repository

A.; et al. A New Route to Porous Metal-Organic Framework Crystal-Glass Composites. *Chem. Sci.* **2020**, *11*, 9910−9918.

(182) Lin, R.; Hou, J.; Li, M.; Wang, Z.; Ge, L.; Li, S.; Smart, S.; Zhu, Z.; Bennett, T. D.; Chen, V. Interfacial Engineering of a Polymer-MOF Composite by in Situ Vitrification. *Chem. Commun.* **2020**, *56*, 3609−3612.

(183) Minami, T. Fast Ion Conducting Glasses. *J. Non-Cryst. Solids* **1985**, *73*, 273−284.

(184) Umeyama, D.; Horike, S.; Tassel, C.; Kageyama, H.; Higo, Y.; Hagi, K.; Ogiwara, N.; Kitagawa, S. Pressure-Induced Amorphization of a Dense Coordination Polymer and Its Impact on Proton Conductivity. *APL Mater.* **2014**, *2*, 124401.

(185) Nagarkar, S. S.; Horike, S.; Itakura, T.; Le Ouay, B.; Demessence, A.; Tsujimoto, M.; Kitagawa, S. Enhanced and Optically Switchable Proton Conductivity in a Melting Coordination Polymer Crystal. *Angew. Chem., Int. Ed.* **2017**, *56*, 4976−4981.

(186) Nakamoto, H.; Noda, A.; Hayamizu, K.; Hayashi, S.; Hamaguchi, H. O.; Watanabe, M. Proton-Conducting Properties of a Bronsted Acid-Base Ionic Liquid and Ionic Melts Consisting of Bis(Trifluoromethanesulfonyl)Imide and Benzimidazole for Fuel Cell Electrolytes. *J. Phys. Chem. C* **2007**, *111*, 1541−1548.

(187) Jiang, G.; Qu, C.; Xu, F.; Zhang, E.; Lu, Q.; Cai, X.; Hausdorf, S.; Wang, H.; Kaskel, S. Glassy Metal-Organic-Framework-Based Quasi-Solid-State Electrolyte for High-Performance Lithium-Metal Batteries. *Adv. Funct. Mater.* **2021**, *31*, 2104300.

(188) Gao, C.; Jiang, Z.; Wang, P.; Jensen, L. R.; Zhang, Y.; Yue, Y. Metal-Organic Framework Glass Anode with an Exceptional Cycling-Induced Capacity Enhancement for Lithium Ion Batteries. *ChemRxiv*, 2021. DOI: 10.26434/chemrxiv.14745477.v1.

(189) Hirai, Y.; Ferreira da Rosa, P. P.; Nakanishi, T.; Kitagawa, Y.; Fushimi, K.; Hasegawa, Y. Amorphous Formability and Temperature-Sensitive Luminescence of Lanthanide Coordination Glasses Linked by Thienyl, Naphthyl, and Phenyl Bridges with Ethynyl Groups. *Bull. Chem. Soc. Jpn.* **2017**, *90*, 322−326.

(190) Kitagawa, Y.; Wada, S.; Islam, M. D. J.; Saita, K.; Gon, M.; Fushimi, K.; Tanaka, K.; Maeda, S.; Hasegawa, Y. Chiral Lanthanide Lumino-Glass for a Circularly Polarized Light Security Device. *Commun. Chem.* **2020**, *3*, 119.

(191) Dini, D.; Calvete, M. J. F.; Hanack, M. Nonlinear Optical Materials for the Smart Filtering of Optical Radiation. *Chem. Rev.* **2016**, *116*, 13043−13233.

(192) Stepniewska, M.; Østergaard, M. B.; Zhou, C.; Yue, Y. Towards Large-Size Bulk ZIF-62 Glasses via Optimizing the Melting Conditions. *J. Non-Cryst. Solids* **2020**, *530*, 119806.

(193) Rouxel, T. Fracture Surface Energy and Toughness of Inorganic Glasses. *Scr. Mater.* **2017**, *137*, 109−113.

(194) Tuffnell, J. M.; Morzy, J. K.; Kelly, N. D.; Tan, R.; Song, Q.; Ducati, C.; Bennett, T. D.; Dutton, S. E. Comparison of the Ionic Conductivity Properties of Microporous and Mesoporous MOFs Infiltrated with a Na-Ion Containing IL Mixture. *Dalton Trans.* **2020**, *49*, 15914−15924.

(195) Zhang, J.-P.; Qi, X.-L.; He, C.-T.; Wang, Y.; Chen, X.-M. Interweaving Isomerism and Isomerization of Molecular Chains. *Chem. Commun.* **2011**, *47*, 4156−4158.

(196) Zhang, J.-P.; Huang, X.-C.; Chen, X.-M. Supramolecular Isomerism in Coordination Polymers. *Chem. Soc. Rev.* **2009**, *38*, 2385−2396.

(197) Su, Y.-J.; Cui, Y.-L.; Wang, Y.; Lin, R.-B.; Zhang, W.-X.; Zhang, J.-P.; Chen, X.-M. Copper(I) 2-Isopropylimidazolate: Supramolecular Isomerism, Isomerization, and Luminescent Properties. *Cryst. Growth Des.* **2015**, *15*, 1735−1739.

(198) Huang, X.-C.; Zhang, J.-P.; Chen, X.-M. A New Route to Supramolecular Isomers via Molecular Templating: Nanosized Molecular Polygons of Copper(I) 2-Methylimidazolates. *J. Am. Chem. Soc.* **2004**, *126*, 13218−13219.

(199) Laniel, R.; Hubert, M.; Miroir, M.; Brient, A., Glass Shaping. *Springer Handbook of Glass*; Springer: Cham, 2019; pp 1259-1292.

(200) Colón, Y. J.; Snurr, R. Q. High-Throughput Computational Screening of Metal-Organic Frameworks. *Chem. Soc. Rev.* **2014**, *43*, 5735−5749.

(201) Volkringer, C.; Falaise, C.; Devaux, P.; Giovine, R.; Stevenson, V.; Pourpoint, F.; Lafon, O.; Osmond, M.; Jeanjacques, C.; Marcillaud, B.; et al. Stability of Metal-Organic Frameworks under Gamma Irradiation. *Chem. Commun.* **2016**, *52*, 12502−12505.

(202) Conrad, S.; Kumar, P.; Xue, F.; Ren, L.; Henning, S.; Xiao, C.; Mkhoyan, K. A.; Tsapatsis, M. Controlling Dissolution and Transformation of Zeolitic Imidazolate Frameworks by Using Electron-Beam-Induced Amorphization. *Angew. Chem., Int. Ed.* **2018**, *57*, 13592−13597.

(203) Widmer, R. N.; Lampronti, G. I.; Casati, N.; Farsang, S.; Bennett, T. D.; Redfern, S. A. T. X-Ray Radiation-Induced Amorphization of Metal-Organic Frameworks. *Phys. Chem. Chem. Phys.* **2019**, *21*, 12389−12395.

(204) Krishnan, N. M. A.; Wang, B.; Le Pape, Y.; Sant, G.; Bauchy, M. Irradiation- Vs. Vitrification-Induced Disordering: The Case of A-Quartz and Glassy Silica. *J. Chem. Phys.* **2017**, *146*, 204502.

(205) Seife, F. So Much More to Know.. *Science* **2005**, *309*, 78−102.

(206) Zhou, J.; Yang, Y.; Yang, Y.; Kim, D. S.; Yuan, A.; Tian, X.; Ophus, C.; Sun, F.; Schmid, A. K.; Nathanson, M.; et al. Observing Crystal Nucleation in Four Dimensions Using Atomic Electron Tomography. *Nature* **2019**, *570*, 500−503.

(207) Schottelius, A.; Mambretti, F.; Kalinin, A.; Beyersdorff, B.; Rothkirch, A.; Goy, C.; Müller, J.; Petridis, N.; Ritzer, M.; Trinter, F.; et al. Crystal Growth Rates in Supercooled Atomic Liquid Mixtures. *Nat. Mater.* **2020**, *19*, 512−516.

(208) Sapnik, A. F.; Bechis, I.; Collins, S. M.; Johnstone, D. N.; Divitini, G.; Smith, A. J.; Chater, P. A.; Addicoat, M. A.; Johnson, T.; Keen, D. A.; et al. Mixed Hierarchical Local Structure in a Disordered Metal-Organic Framework. *Nat. Commun.* **2021**, *12*, 2062.

(209) Simonov, A.; De Baerdemaeker, T.; Boström, H. L. B.; Ríos Gómez, M. L.; Gray, H. J.; Chernyshov, D.; Bosak, A.; Bürgi, H.-B.; Goodwin, A. L. Hidden Diversity of Vacancy Networks in Prussian Blue Analogues. *Nature* **2020**, *578*, 256−260.

(210) Simonov, A.; Goodwin, A. L. Designing Disorder into Crystalline Materials. *Nat. Rev. Chem.* **2020**, *4*, 657−673.

(211) Yang, Y.; Zhou, J.; Zhu, F.; Yuan, Y.; Chang, D. J.; Kim, D. S.; Pham, M.; Rana, A.; Tian, X.; Yao, Y.; et al. Determining the Three-Dimensional Atomic Structure of an Amorphous Solid. *Nature* **2021**, *592*, 60−64.